7 Accelerator

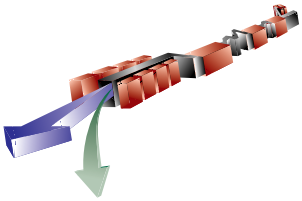

TECHNICAL SYNOPSIS

In order for the SASE FEL to operate in saturation, a high electron peak current with small transverse and longitudinal emittance is required. The LCLS nominally operates within a range of wavelengths from 15 to 1.5 Å. The most challenging parameters coincide with the 1.5-Å configuration with maximum peak current of 3.4 kA, transverse normalized 'slice' emittance of 1.2 μm, and top end energy of 14.35 GeV. Since the rf photocathode gun produces 1 nC in a bunch length of 3 psec rms, corresponding to a peak current of 100 A, the bunch has to be compressed by a factor of 35 before it enters the undulator. The acceleration and compression is done in the final kilometer of the slightly modified SLAC S-band linac.

The bunch compressors consist of a series of magnetic chicanes, arranged and located such that non-linearities in the compression and acceleration process (longitudinal wakefields, rf curvature, and second order momentum compaction) are approximately compensated. A short section of X-band rf is also used prior to the first compressor in order to linearize and stabilize the system. An optimal choice of linac design parameters both cancels the correlated energy spread after the final compression, and desensitizes the system to phase and charge variations. The electron energy at the first compressor is 250 MeV. This choice avoids space charge effects, while compressing the bunch early enough in the linac to ease the effects of transverse wakefields. In the first compressor, the bunch length is reduced from ~1 mm to 0.2 mm rms. The second compressor produces a 22-μm bunch. The energy of the second compressor, 4.54 GeV, is chosen as a balance between the conflicting requirements of longitudinal emittance dilution due to synchrotron radiation, and the need to cancel the final correlated energy spread. The design of the compressors is dominated by the need to reduce coherent synchrotron radiation (CSR) effects, which are most pronounced for short bunches. The most significant effect of CSR is to generate a correlated energy gradient along the bunch. By using a weak chicane and a large initial correlated energy spread, the effect of CSR on the transverse emittance can be reduced.

Simulations have been made which calculate emittance dilution in the linac due to transverse wakefields and anomalous momentum dispersion, each of which arises with component misalignments. These simulations include realistic correction techniques and successfully demonstrate the level of transverse emittance preservation required. Diagnostics, correction techniques, and feedback systems have also been incorporated into the design. Finally, the acceleration and compression systems are flexible enough to allow a high degree of operational variation in beam parameter choices, such as bunch charge, final beam energy, and an optional electron chirp, used for x-ray pulse compression.

7.1 Introduction and Overview

In order to reach SASE saturation in a reasonable length undulator, a high electron peak current is required. For a radiation wavelength of 1.5 Å, an undulator period of 3 cm, and an undulator parameter of $K \approx 3.7$, the desired electron beam should have a peak current of 3.4 kA, energy of 14.3 GeV, and transverse normalized rms 'slice' emittance of ≤1.2 μm. A longitudinal 'slice' of the electron beam is defined by the FEL slippage length (~0.5 μm in this case). These values correspond to an rms bunch length of 22 μm and charge of 1 nC, which is not possible in present rf photo-injectors due to space charge limitations. Therefore the bunch is accelerated and compressed in a series of linacs and magnetic chicanes. The accelerator must preserve the transverse emittance produced by the rf photo-injector. A slice emittance growth of <20% and projected emittance growth of 50-100% are allotted to the accelerator. Extensive tracking studies indicate this level is achievable (see **Section 7.6**).

Energy spread requirements in the undulator at 14.3 GeV are <0.1% and <0.02% for the rms coherent (correlated) and incoherent (uncorrelated) components, respectively. The nominal machine described here is designed to operate at a repetition rate of up to 120 Hz in a single-bunch mode with 1-nC of charge per bunch, and with the flexibility of running at significantly lower charge [1]. Future multi-bunch operations may also be possible [2], but are not described here. **Figure 7.1** shows a schematic of the LCLS accelerator. The nominal beam energy, rms bunch length (σ_z), and rms relative energy spread (σ_δ) are indicated at points along the accelerator, as are section parameters, such as length (L), rf phase (φ_{rf}), and momentum compaction (R_{56}).

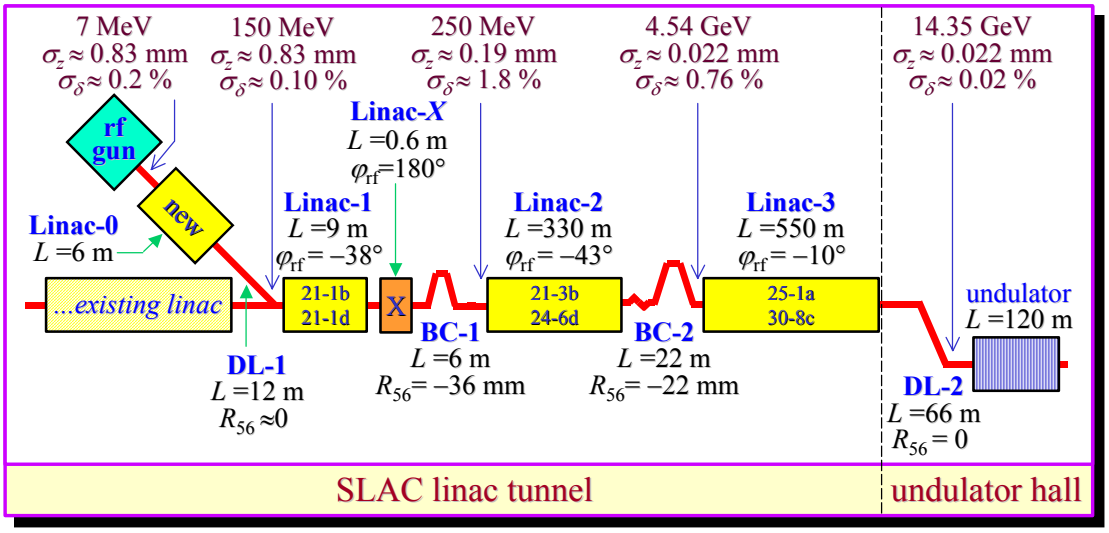

Figure 7.1 LCLS compression and acceleration schematic. The 'dog-legs' (DL-1 and DL-2) are simple transport lines and have no effect on bunch length, while the compressors are four-dipole chicanes. Acceleration crest is defined at $\varphi_{rf} = 0$.

The LCLS accelerator is composed of four S-band linac sections ($f_{rf} = 2.856$ GHz), one short X-band section ($f_{rf} = 11.424$ GHz), and four separate bending sections. The first linac (Linac-0 or

L0) is a new section installed in an existing off-axis enclosure adjacent to the beginning of sector-21. L0 is composed of two 3-m RF structures and accelerates the ~1-mm long bunch from the rf gun to 150 MeV. The space-charge emittance compensation is also finalized in L0 (see **Chapter 6).** The transport line following L0 (low energy 'dog-leg' or DL1) provides energy and emittance diagnostics and includes a bending section for injection into the SLAC linac at a 35˚ angle. Linac-1 (L1) accelerates the bunch "off-crest" to 272 MeV and generates a nearly linear energy correlation along the bunch to initiate the first stage of compression.

A short X-band rf section (LX), immediately following L1, is used to linearize the compression by removing the quadratic energy-time bunch correlation generated in L0 and L1. It operates at 180˚ and decelerates the beam by 22 MeV setting the BC1 compression energy at 250 MeV. The linearization allows strong compression in the first stage while maintaining a fairly uniform temporal distribution along the bunch. The first bunch compressor is a 4-dipole chicane (BC1, located at the start of linac sector-21), which shortens the bunch to 0.20 mm rms. Linac-2 (L2) then accelerates the bunch to 4.54 GeV, also at an off-crest phase, which maintains the desired linear energy correlation.

The second compressor is another 4-dipole chicane (BC2, at the end of linac sector-24) which compresses the bunch to its nominal final value of 22-μm rms. The very high peak current generated by the compression in BC2 can drive a micro-bunching instability [3], [4], which can damage both the slice emittance and the slice energy spread. In order to damp these effects, a very strong one-period superconducting wiggler is placed just upstream of the BC2 chicane in order to increase the incoherent energy spread of the beam. An increase to 3×10^{-5} rms (from 3×10^{-6} at 4.54 GeV without wiggler) is sufficient to suppress the instability without adding too much energy spread for the 1.5-Å SASE FEL. This is described in more detail in **Section 7.4.2**.

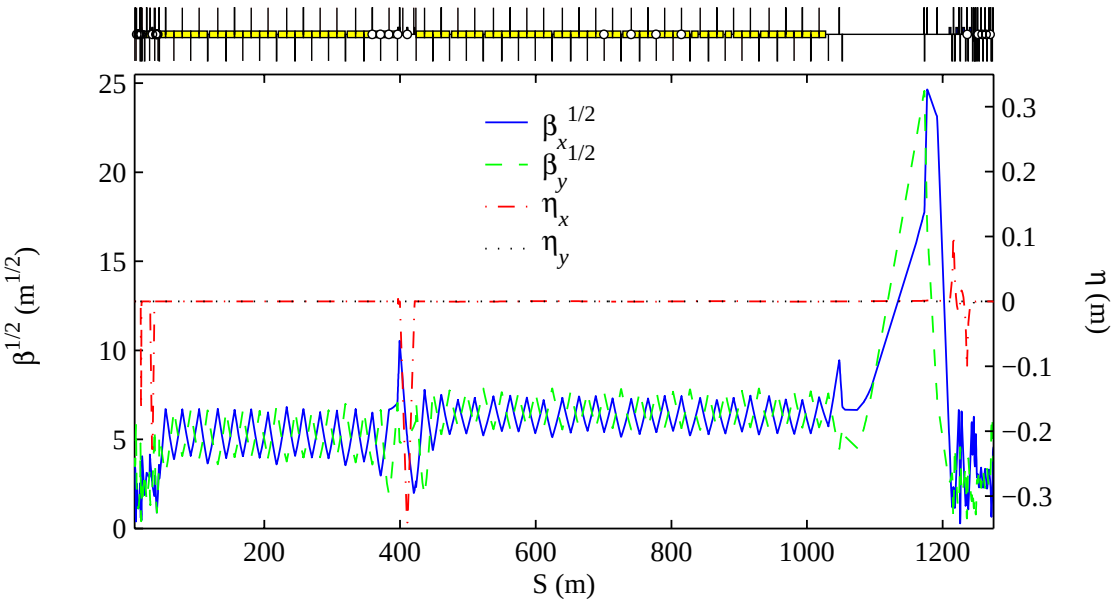

Figure 7.2 Twiss parameters for the LCLS accelerator from linac-0 exit to undulator entrance. The first compressor, BC1, is at $S \approx 30$ m and the second, BC2, is at $S \approx 400$ m.

Finally, Linac-3 (L3) accelerates the beam, nearly on-crest, to 14.35 GeV (a range of approximately 4.5-15 GeV is available) and also cancels the linear correlated energy spread with the strong geometric longitudinal wakefield of the S-band rf-structures. The high-energy dog-leg bend system (DL2) is designed for energy and energy spread analysis, transverse emittance measurement, final beam transport, and matching into the undulator. It is also useful for collimating dark-current and any off-energy beam halo prior to the undulator.

Each system, its parameters, and design criteria, as well as beam dynamics in the LCLS accelerator are discussed in the following sections. **Figure 7.2** shows the Twiss parameters for the 1266-meter LCLS accelerator from end of L0 injector to undulator entrance.

7.2 Longitudinal Beam Dynamics

To achieve the high peak current and small energy spread in the undulator, the bunch must be compressed in a series of magnetic chicanes. These are arranged and located such that non-linearities in the compression and acceleration process (longitudinal wakefields, rf curvature, and second order momentum compaction) are mostly canceled. With a careful arrangement of parameters, the bunch compression process can be made more linear, which reduces the minimum bunch length achievable and helps to avoid very high peak current spikes in the temporal distributions, which may drive collective effects. An optimum choice of parameters compensates the correlated energy spread after final compression and desensitizes the system to phase and charge jitter. In addition, the compressors must be designed to mitigate the effects of synchrotron radiation so the transverse emittance is not diluted. A semi-analytic fast computer program has been written to choose the acceleration and compression parameters in order to provide for these concerns [5]. An accelerator design for a 1-nC bunch charge is described here, but studies have also shown that a very wide variety of machine configurations are possible (including a 0.25-nC bunch charge scenario [6]) with simple, operational adjustments.

7.2.1 Bunch Compression Overview

The bunch is compressed by accelerating with an off-crest rf phase, thereby introducing a correlated energy spread along the bunch. This process is followed by a bending section, which has a linear path length dependence on particle energy. Temporarily ignoring wakefields, the final energy (E_f) of a particle, which is at axial position z_i with respect to bunch center, after nominal acceleration from E_{i0} to E_{f0} at an rf phase φ_0 (crest at $\varphi_0 = 0$ and $\varphi_0 \neq \pi/2$), is given by

$$E_f = E_i + \frac{E_{f0} - E_{i0}}{\cos\varphi_0}\cos\left(\varphi_0 + \Delta\varphi + 2\pi z_i/\lambda\right) , \qquad \textbf{(7.1)}$$

with $\Delta\varphi$ as a potential rf phase error, λ the rf wavelength, and E_i the initial (not perfectly nominal) beam energy. Here, the convention is used that the leading 'head' of the bunch is in the direction $z < 0$. The relative energy deviation after acceleration, $\delta_f \equiv (E_f - E_{f0})/E_{f0}$, is then

$$\delta_f \approx \delta_i + \left(1 - \frac{E_{i0}}{E_{f0}}\right)\left[\frac{\cos(\varphi_0 + \Delta\varphi) - [2\pi z_i/\lambda]\sin(\varphi_0 + \Delta\varphi)}{\cos\varphi_0} - 1\right], \qquad \textbf{(7.2)}$$

where $\delta_i \equiv (E_i - E_{i0})/E_{f0}$ represents small injection energy deviations scaled to the final energy. Wakefields are ignored here, and it is assumed that $|z_i| << \lambda/2\pi$. From **Eq. (7.2)** the linear correlation constant, k, is defined as

$$k(\varphi_0, \Delta\varphi) \equiv \frac{\partial\delta_f}{\partial z_i} = -\frac{2\pi}{\lambda}\left(1 - \frac{E_{i0}}{E_{f0}}\right)\frac{\sin(\varphi_0 + \Delta\varphi)}{\cos\varphi_0} \ . \qquad \textbf{(7.3)}$$

After a bending section with path length dependence, R_{56}, where $z_f = z_i + R_{56}\delta_f$, the final bunch length, σ_{zf}, and energy spread, $\sigma_{\delta f}$, are functions of the initial bunch length, σ_{z_i}, and energy spread, σ_{δ_i}, (assuming an uncorrelated initial bunch $\langle z_i\delta_i\rangle = 0$):

$$\sigma_{z_f} = \sqrt{(1 + kR_{56})^2\,\sigma_{z_i}^2 + R_{56}^2\sigma_{\delta_i}^2} \approx |1 + kR_{56}|\,\sigma_{z_i} \ ,$$
$$\sigma_{\delta_f} = \sqrt{k^2\sigma_{z_i}^2 + \sigma_{\delta_i}^2} \approx |k|\,\sigma_{z_i} \ . \qquad \textbf{(7.4)}$$

The injection energy spread, scaled to the final energy, $\sigma_{\delta i}$, is typically insignificant here. Minimum bunch compression is achieved for $R_{56} = -1/k$, with under-compression at $|R_{56}| < 1/|k|$ and over-compression for $|R_{56}| > 1/|k|$. For a magnetic chicane, the R_{56} value is negative (with bunch head at $z < 0$), and compression is achieved with $k > 0$ (or $-\pi/2 < \varphi_0 < 0$; i.e., bunch head at a lower energy than bunch tail).

Since k is a function of $\Delta\varphi$, the bunch length is sensitive to phase variations and injector timing jitter. For a single stage compressor, the final bunch length change, $\Delta\sigma_{z_f}$ for a phase change, $\Delta\varphi$, is given by [7]

$$\frac{\Delta\sigma_{z_f}}{\sigma_{z_{f0}}} \approx -\left(\frac{\sigma_{z_i}}{\sigma_{z_{f0}}} \mp 1\right)\Delta\varphi\cot\varphi_0 \ , \qquad \textbf{(7.5)}$$

with under-compression expressed by the minus sign and over-compression by the plus sign. For $\varphi_0 = 20°$ and a compression ratio of $\sigma_{z_i}/\sigma_{z_{f0}} = 33$, phase jitter of only 0.1° S-band (0.1 psec) results in final bunch length (or undulator peak current) jitter of ~16%. **Figure 7.3** shows the required R_{56}, and the bunch length sensitivity to phase jitter, versus nominal rf phase, for a single stage compressor with compression ratios of both 33 and 3.3.

Clearly, a single stage compressor is too sensitive. Furthermore, the final bunch length of a single stage compressor is limited by non-linearities, such as rf curvature, which make compression from ~1 mm to 22 μm very difficult. However, a two-stage compression system brings about cancellations that can reduce this phase jitter sensitivity by more than an order of magnitude. This arrangement allows the first compressor to be located at relatively low energy so that the next linac accelerates a shorter bunch. The reduced transverse wakefield of the shorter bunch provides looser rf-structure alignment tolerances. Conversely, a single compression stage

would need to be placed at a high enough beam energy so that space charge forces are not significant for a 22 μm bunch. Such a single stage system would prolong the acceleration of the long bunch through more linac, which tightens alignment tolerances. For these reasons, a two-stage compressor is used.

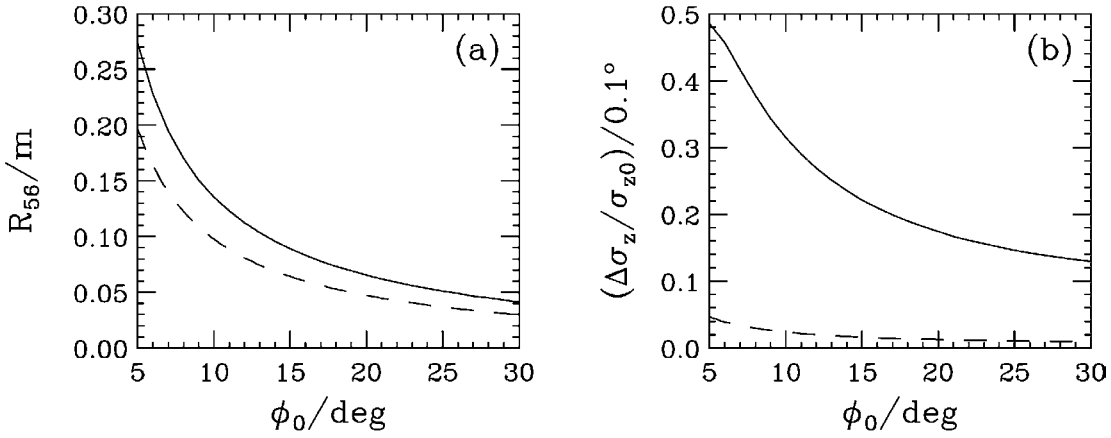

Figure 7.3 The required R_{56} (a) and the relative bunch length change per 0.1°(S-band) phase jitter (b) for a single stage compressor and linac which accelerates a 1-mm bunch from 80 MeV to 250 MeV at an rf phase of φ_0 for a final bunch length of both 30 μm (solid) and 300 μm (dashed).

The linear relations for a two-stage bunch compression system are similarly expressible. For a first linac which accelerates from E_0 to E_1 at rf phase φ_1 followed by a first compressor with $R_{56} \equiv \alpha_1$, then a second linac which accelerates from E_1 to E_2 at rf phase φ_2 followed by a second compressor with $R_{56} \equiv \alpha_2$, the final bunch length, σ_{z_2}, and energy spread, σ_{δ_2}, are approximately

$$\sigma_{z_2} \approx \sqrt{\left[\left(1+\alpha_1 k_1\right)\left(1+\alpha_2 k_2\right)+\alpha_2 k_1 E_1/E_2\right]^2\sigma_{z_0}^2+\left[\alpha_1\left(1+\alpha_2 k_2\right)E_0/E_1+\alpha_2 E_0/E_2\right]^2\sigma_{\delta_0}^2}\ ,$$

$$\sigma_{\delta_2} \approx \sqrt{\left[k_2\left(1+\alpha_1 k_1\right)^2+k_1 E_1/E_2\right]^2\sigma_{z_0}^2+\left[\alpha_1 k_2 E_0/E_1+E_0/E_2\right]^2\sigma_{\delta_0}^2}\ . \qquad \textbf{(7.6)}$$

In this case, σ_{δ_0} is the relative energy spread at injection to the first linac (at energy E_0) and σ_{z_0} is the initial bunch length there. Note, k_1 is a function of the rf phase and initial and final energies of Linac-1 as in **Eq. (7.3)**. The value for k_2, however, depends on the total phase error, which may have contributions from both Linac-1 and Linac-2:

$$k_2 = -\frac{2\pi}{\lambda}\left(1-\frac{E_1}{E_2}\right)\frac{\sin\left(\varphi_2+\left(1+\alpha_1 k_1\right)\Delta\varphi_1+\Delta\varphi_2\right)}{\cos\varphi_2}\ . \qquad \textbf{(7.7)}$$

It appears that the above relationships can be used to find a minimum final bunch length sensitivity to injection phase jitter, $\Delta\varphi_1$. In fact, longitudinal wakefields, rf curvature, and second order path length dependence, T_{566}, complicate these calculations sufficiently to invalidate this simple linear model. The above relationships can help one to understand sensitivities, but the

optimal stability is best found with a complete computer simulation that includes the important non-linearities and wakefield effects.

7.2.2 Design Optimization Technique

In order to determine the best parameter set which provides the correct acceleration, compression, machine stability, and final energy spread, a fast computer program is used which semi-analytically models the longitudinal beam dynamics and minimizes a penalty function while varying the key system parameters [5]. The varied parameters are:

- 1st and 2nd compressor strengths ($R_{56\text{-}1}$, $R_{56\text{-}2}$),
- RF phases of L1, L2, and L3 (φ_1, φ_2, φ_3),
- Energy (or location) of 1st and 2nd compression stages (E_{BC1}, E_{BC2}).

The penalty function, which is minimized, includes:

- The deviation of the final and intermediate bunch lengths from the desired ones, normalized to an allowable error (e.g., 22 μm ± 0.1 μm rms at undulator, and 200 μm ± 100 μm after BC1),
- The energy deviation at both compressors and at the undulator, with respect to the desired energy, each normalized to an allowable error (e.g., 14.35 GeV ± 0.02 GeV at undulator, or 250, +250, −50 MeV at 1st compressor),
- The deviation of the final correlated energy spread at the undulator with respect to the desired energy spread, normalized to an allowable error (e.g., 0.01% ± 0.002% — this is a signed quantity allowing for a positive or negatively correlated energy chirp as a desired outcome),
- The four sensitivities of: 1) final relative energy error vs. gun-timing error, and 2) vs. bunch-charge error; 3) the final peak current vs. gun-timing error, and 4) vs. bunch-charge error, all normalized to an allowable error (e.g., 0 ± 100 Amps/psec).

The parameters are varied over a reasonable range by constraining the minimization scan. The parameters constrained are:

- The two R_{56} values (e.g., −10 mm to −40 mm),
- The mean rf accelerating gradient per linac section (e.g., 18 MV/m upper limit),
- The three rf phases per linac section (e.g., −50° to +50°),
- The net active S-band linac length available to the LCLS beam (~900 m).

The semi-analytic model includes longitudinal wakefields, non-linearities (T_{566} and sinusoidal rf), and the effects of errors (timing, phase, charge and energy). The model also includes the X-band rf section, its wakefield, and its four-fold frequency increase. The details of the model and its range of validity are reviewed in reference [5]. The final chosen parameters, which provide for optimum machine stability, as well as the undulator peak current and energy spread requirements

are described below for the nominal case of a 1-nC bunch charge. Before final parameters are described, however, the motivations for the X-band rf section are described.

7.2.3 X-Band RF Compensation

A short X-band rf section (f_{rf} = 11.424 GHz) is included just prior to the BC1 chicane in order to better linearize the energy-time correlation along the bunch. A more linear correlation allows the bunch to be compressed to a much smaller length than would be possible without the X-band section. The 0.6-meter long X-band section is run at the decelerating crest phase (180˚) so that second order energy-time correlations in the beam, which are induced in the S-band linac-0 and linac-1, can be removed. The net beam energy is only reduced by 22 MeV (from 272 MeV to 250 MeV) by the X-band section, which is run at a relatively low gradient of ~37 MV/m. Without the X-band rf, the initial bunch length of 830 μm can only be compressed to ~400 μm rms without a large spike appearing at the head of the temporal distribution. A large peak-current spike can drive severe beam instabilities due to coherent synchrotron radiation (CSR) in the chicanes, which can quickly destroy the horizontal emittance and slice energy spread. Since the results of the fast design optimization code (described above) indicate a first compression level of 200 μm is desirable, the X-band section is needed to allow this possibility.

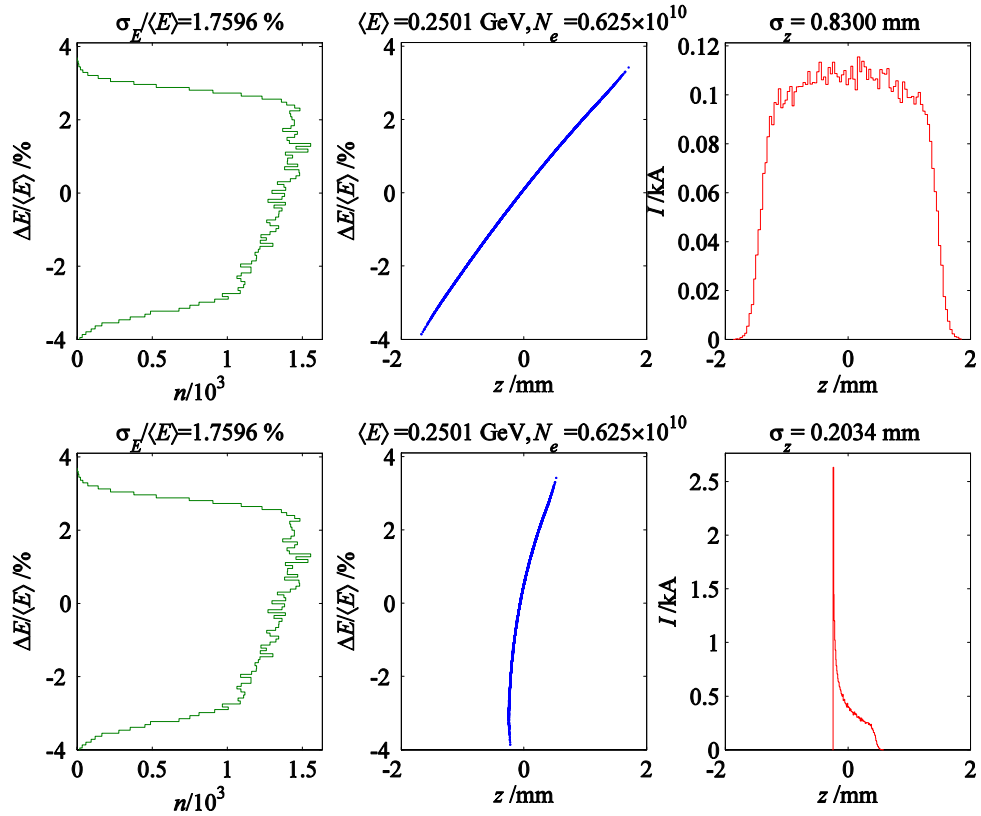

Figure 7.4 Simulated compression *without* X-band rf, where an 830-μm bunch is being compressed *towards* 200 μm (top-row: after S-band rf, bottom-row: after chicane). The bunch begins to fold over itself causing an large undesirable peak current spike.

Figure 7.4 shows a simulated compression *without* X-band rf, where an 830-μm bunch (top row of plots) is being compressed toward 200 μm (bottom row of plots). The bunch begins to fold over itself after the chicane resulting in a peak current spike at the head of the bunch in excess of 2 kA. The effect is exaggerated by the T_{566} of the chicane, which is always of a sign ($0 < T_{566} \approx -3R_{56}/2$) to amplify the S-band rf curvature (i.e., for an accelerating rf phase and a simple chicane without internal focusing optics).

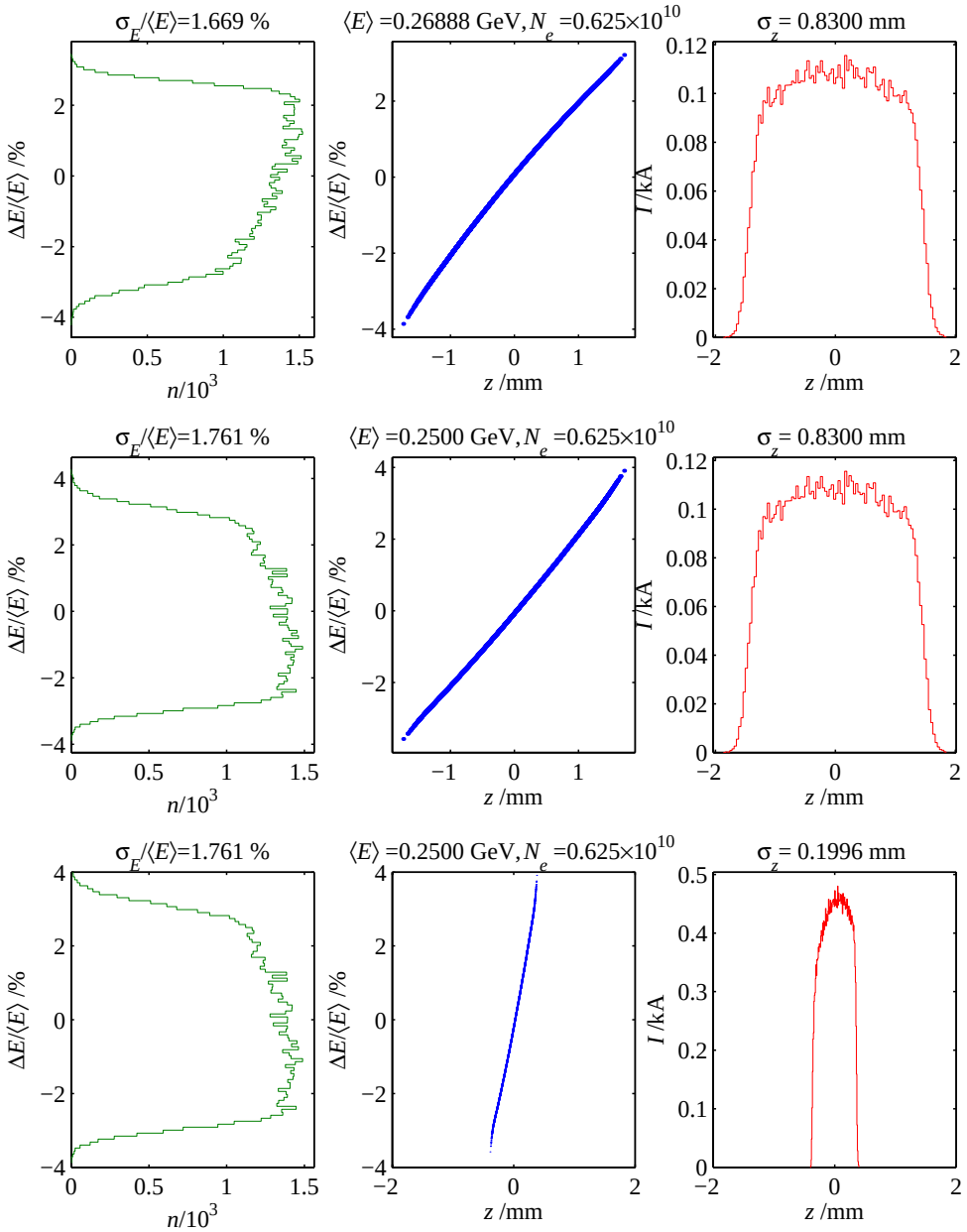

Figure 7.5 Simulated compression, now *including* X-band rf, where the *same* 830-μm bunch is easily compressed to 200 μm, and the final temporal distribution is unaltered (top-row: after S-band rf, middle-row: after X-band rf, bottom-row: after chicane). In addition, the bunch can easily be compressed much further if desired.

With the X-band rf included at a decelerating phase, and with the proper voltage (see below), the compression can be linearized such that a 200-μm rms bunch length is easily achievable with no significant alteration in the temporal distribution. **Figure 7.5** shows the simulation, starting from similar conditions as the top row of plots in **Figure 7.4**, but with some minor S-band phase and voltage adjustments (top row of **Figure 7.5**), and proceeding through the 20-MV X-band rf (middle row of **Figure 7.5**), and then through the chicane (bottom row of **Figure 7.5**). The final temporal distribution is nearly unaltered with the proper X-band rf compensation.

The X-band voltage, V_x, required to compensate the non-linear energy-time correlations induced in both the L0 and the L1 linacs, as well as that of the chicane, is given by [8]

$$eV_x = \frac{E_0\left[1-\frac{1}{2\pi^2}\frac{\lambda_s^2 T_{566}}{R_{56}^3}\left(1-\sigma_z/\sigma_{z0}\right)^2\right]-E_i}{\left(\lambda_s/\lambda_x\right)^2-1}\,, \qquad \textbf{(7.8)}$$

where λ_s and λ_x are the S-band and X-band, respectively, rf wavelengths (10.50 cm and 2.625 cm), σ_{z0} and σ_z are the initial and final bunch lengths, and E_i and E_0 are the initial and final beam energies at gun and BC1 chicane, respectively. The net deceleration is small due to the large denominator in **Eq. (7.8)**, which stems from the high harmonic number chosen ($\lambda_s/\lambda_x = 4$). For parameters $R_{56} \approx -35.9$ mm, $T_{566} \approx -3R_{56}/2 \approx +53.9$ mm, $\sigma_{z0} \approx 830\ \mu$m, $\sigma_z \approx 200\ \mu$m, $E_i \approx 7$ MeV, and $E_0 \approx 250$ MeV, the X-band voltage which removes the 2nd-order energy-time correlation along the bunch after BC1 is $V_x \approx 22$ MV. Tracking studies show that this voltage provides a more uniform temporal distribution after BC2 (see **Figure 7.6** and **Figure 7.7**).

With the availability at SLAC of high-gradient X-band accelerating structures developed for the NLC project [9], this 4th harmonic compensation strategy becomes a practical solution for the LCLS. A relatively low rf gradient of 37 MV/m allows a 0.6-meter long section to be used. The mean iris radius is 4.7 mm, which is very large for the typical beam size of 100 μm (see beta functions in **Figure 7.14**). The transverse wakefields of the X-band structure are strong, but the section is very short. The alignment tolerance of the short X-band structure is therefore ~200 μm, which is not particularly challenging.

A similar X-band section is not required at the entrance to BC2, since the quadratic correlation in the bunch after the L2-linac is much less pronounced than that after L1, due to the shortened bunch in L2 with respect to the S-band rf.

In addition to linearizing the compression process, the X-band rf also makes the net compression less sensitive to rf gun-timing jitter. Since the net accelerating voltage, as a function of beam arrival time, is more linear when the X-band rf is included, the induced energy-time correlation along the bunch then becomes nearly independent of beam arrival time [8]. This loosens the rf gun-timing jitter sensitivity by nearly a factor of four with respect to that published in the LCLS Design Study Report [16] (see also **Figure 7.8**). The section will need a dedicated X-band klystron, which is available at SLAC. The existing modulator at 21-2 will be used.

7.2.4 Nominal Parameters

The nominal design parameters for the LCLS two-stage bunch compression system at a bunch charge of 1 nC are summarized graphically in **Figure 7.1** and numerically in **Table 7.1** below.

A string of five linac sections and two chicane sections are used to compress an 830-μm rms bunch at 150 MeV to 22-μm rms at 14.35 GeV. The final bunch is still under-compressed, so it is actually possible to compress it even further (to <5 μm rms). However, many severe challenges arise with a shorter bunch at 1 nC, such as coherent synchrotron radiation in BC2 (see **Section 7.4.2**) and resistive wall and surface roughness wakefields in the undulator vacuum chamber (see **Chapter 8,** "Wakefield Effects in the Undulator"). These effects can become intolerable for much shorter bunches, depending on the charge. An rms bunch length of 22 μm at 1 nC achieves the 3.4-kA peak current required and should allow management of the various micro-bunch limitations. A longer bunch is also operationally possible if the transverse "slice" emittance achieved is less than 1.2 μm [e.g., $\sigma_z \approx 34$ μm at $\gamma\varepsilon \approx 1.0$ μm and $Q \approx 1$ nC, see **Eq. (7.11)**].

Table 7.1 LCLS nominal compression and acceleration parameters per beamline section, for a 1-nC bunch charge. The phase of −10° in L3 helps to stabilize the beam energy.

Beamline	E_{in}	E_{out}	$\sigma_{z\text{-in}}$	$\sigma_{z\text{-out}}$	$\sigma_{\delta\text{-in}}$	$\sigma_{\delta\text{-out}}$	φ_{rf}	R_{56}
	GeV	GeV	mm	mm	%	%	deg	mm
Linac-1	0.15	0.27	0.83	0.83	0.10	1.67	−38.1	—
Linac-*X*	0.27	0.25	0.83	0.83	1.67	1.78	180	—
BC1	0.25	0.25	0.83	0.19	1.78	1.78	—	−35.9
Linac-2	0.25	4.54	0.19	0.19	1.78	0.76	−42.8	—
BC2	4.54	4.54	0.19	0.022	0.76	0.76	—	−22.5
Linac-3	4.54	14.35	0.022	0.022	0.76	0.02	−10.0	—

For this ultra-relativistic beam, the bunch length cannot change through a linac (excluding L0), and the energy spread does not significantly change through the chicanes. Phase and current jitter tolerances are described in **Section 7.2.6**.

The first stage of compression is from 830 μm to 190 μm. This level of compression is only possible by including the short X-band rf section (Linac-*X* or LX) just prior to BC1. As described above, the X-band rf linearizes the compression. This is accomplished by running the X-band section at the decelerating rf crest (180°) at 22 MV. In this case, L1 accelerates to 272 MeV and LX decelerates to 250 MeV. This choice, for the parameters of **Table 7.1**, also best minimizes final bunch length sensitivity to injector timing and charge jitter. Finally, the chosen value of 190 μm also optimally scales the longitudinal wakefield in Linac-2 so that a cancellation is established between the Linac-2 wake and the small non-linearities (rf curvature and T_{566}) of the Linac-1/BC1 pair. The parameters are not a unique solution but represent a workable set at 1 nC. Many other possible solutions are available, including parameter sets which optimize a bunch

charge anywhere from 1 nC to 0.1 nC, or optimize with an intentional electron chirp at the undulator. A qualitative summary of the effects of changes to the critical compression parameters is listed in **Table 7.2**. The two R_{56} values are not considered free parameters here since their values depend on rf phases and other factors.

The lower limit on the choice for BC1 energy is set by space charge forces of the shorter bunch with 250 MeV considered a safe energy. The upper limit is set by the desire to initially compress the bunch early in the linac to ease transverse wakefields. The chosen energy of 250 MeV also desensitizes the system to injector timing jitter and is a practical solution for L1, which consists of one klystron powering three 3-meter S-band sections at an rf phase of −38° off crest at an average gradient of 17.5 MV/m. The location (energy) of BC2 is set by the need to produce a very small energy spread at 14.3 GeV. This involves a balance between the longitudinal geometric wakefield in L3 (which scales with Linac-3 length) and the remaining δ-z correlation just after BC2. Other factors, including synchrotron radiation, are discussed in more detail in **Section 7.4.1** (BC1) and **Section 7.4.2** (BC2).

Table 7.2 Bunch compression parameter trade-offs: A qualitative summary of the effects of changes to the bunch compression parameters. Only limitations are noted. An "increase" of rf phase, φ, refers to moving farther off rf crest and σ_{z1} is the intermediate bunch length (after BC1, but before BC2).

Parameter	Increase Parameter	Decrease Parameter
$\sigma_{z_1} \approx 190\ \mu$m	• Insufficient L2 wake compensation for L2/BC2 non-linearities. • Requires stronger BC2 and more CSR.	• CSR emittance growth increased in BC1. • Can increase jitter sensitivity.
$\lvert\varphi_1\rvert \approx 38°$	• Increased L1 energy spread. • Inefficient acceleration.	• Can increase jitter sensitivity. • Increased BC1 strength and $\Delta\varepsilon$ due to CSR.
$\lvert\varphi_2\rvert \approx 43°$	• Energy spread too large for cancellation with L3 wake. • Inefficient acceleration.	• Energy spread too small—over-compensated with L3 wake. • Increased BC2 strength and CSR $\Delta\varepsilon$.
$E_1 = 250$ MeV	• Longer L1—> stronger L1 transverse wakes and increased L1 $\Delta\varepsilon$. • Can increase jitter sensitivity.	• Increase BC1 chicane strength and CSR $\Delta\varepsilon$. • Increased space charge forces.
$E_2 = 4.54$ GeV	• Increase BC2 $\Delta\varepsilon$ due to incoherent synchrotron radiation, or lengthen BC2. • Shorter L3—> insufficient L3 wake for L2 energy spread compensation.	• Longer L3—> L3 wake too large— over-compensation of L2 energy spread. • Shorter L2—> insufficient L2 wake compensation for L2/BC2 non-linearities.

System optimization scans show that even higher BC2 energy (i.e., >4.5 GeV) can further desensitize the final bunch length and final energy to gun timing and charge jitter. In this case, however, the BC2 chicane needs to be even stronger and longer, so a compromise has been made at 4.54 GeV, which is also consistent with operation at a 15-Å FEL radiation wavelength, where the L3 linac RF is simply switched off.

7.2.5 Longitudinal Tracking Summary

In this section the longitudinal geometric wakefield and other beam dynamics effects are applied in a 6D tracking simulation to graphically summarize the compression process through the accelerator. (A full 6D tracking summary is presented in **Section 7.6**.) A more detailed description of the wakefields for the SLAC S-band accelerating structures, as well as a justification for the use of the asymptotic wake, is given in **Section 7.9**. The tracking code used here is *Elegant* [10], which includes non-linearities such as T_{566}, U_{5666} (the second and higher-order compression terms), longitudinal geometric wakefields of the rf-structures, resistive-wall longitudinal wakefields (where significant), the sinusoidal rf accelerating voltage, and the incoherent and coherent synchrotron radiation in the bends (CSR is a 1D line-charge model). The tracking proceeds from the output of the LCLS injector, at 150 MeV, to the undulator entrance at 14.3 GeV. The 6D input particle coordinates are from *Parmela* [11] after tracking through the LCLS injector to the end of L0 at 150 MeV [12]. The tracking uses $2{\cdot}10^5$ macro-particles.

A more complete summary of the tracking is presented in **Section 7.6**. The *Elegant* simulations ignore space charge effects, since the compression process takes place at energies well above 150 MeV. The input particle coordinates from *Parmela* do, however, include the effects of space charge forces at energies below 150 MeV.

Figure 7.6 and **Figure 7.7** show longitudinal phase space, energy distributions, and axial (z) distributions at various points in the compression process. The input gun-laser pulse has a uniform temporal distribution with a 1-psec rise/fall-time and the RF gradient in the gun is 120 MV/m. After acceleration to 150 MeV, the temporal distribution becomes slightly rounded, as shown in the figures, with a 0.83-mm rms bunch length (2.8-ps rms, or 10.2-ps FWHM) and 0.11-% rms projected relative energy spread at 150 MeV, with a bunch population of $6.25{\times}10^9$ ppb (1 nC). The rms incoherent energy spread is very small at just 3 keV ($2{\times}10^{-5}$ of 150 MeV).

As **Figure 7.6** and **Figure 7.7** show, the compression process has been arranged so that many of the non-linearities, such as rf-curvature and wakefield effects, will be compensated, leaving a narrow energy profile at 14.3 GeV. The final rms bunch length is 22 μm with >3.0 kA of peak beam current all along the bunch. Tails exist in the energy distribution (shown on 3rd row of **Figure 7.7**). The core of the beam, however, has an rms energy spread of ~0.01% with ~80% of the particles contained within a ±0.1% energy window. The energy tails ($|\Delta E/E_0| > 0.1\%$), which comprise 20% of the beam, have been cut out of the bottom row of **Figure 7.7** (14.3 GeV) to show the core beam more clearly, while all particles are shown in the 3rd row of **Figure 7.7**. Note, the incoherent component of the final energy spread at any particular slice of the bunch core (0.75 μm slice > FEL slippage length) is 0.008% rms, including the incoherent synchrotron radiation of the high-energy bends. The slight micro-bunching seen in the final temporal profile is a result of the CSR effects in the two compressor chicanes, and may be somewhat exaggerated here by possible overestimates of a 1D line-charge CSR model and also by the statistical noise levels of just $2{\times}10^5$ macro-particles. A superconducting one-period wiggler is added just before the BC2 chicane in order to add incoherent energy spread and damp this CSR-induced micro-bunching. This subject is covered in more detail in **Section 7.4.2**.

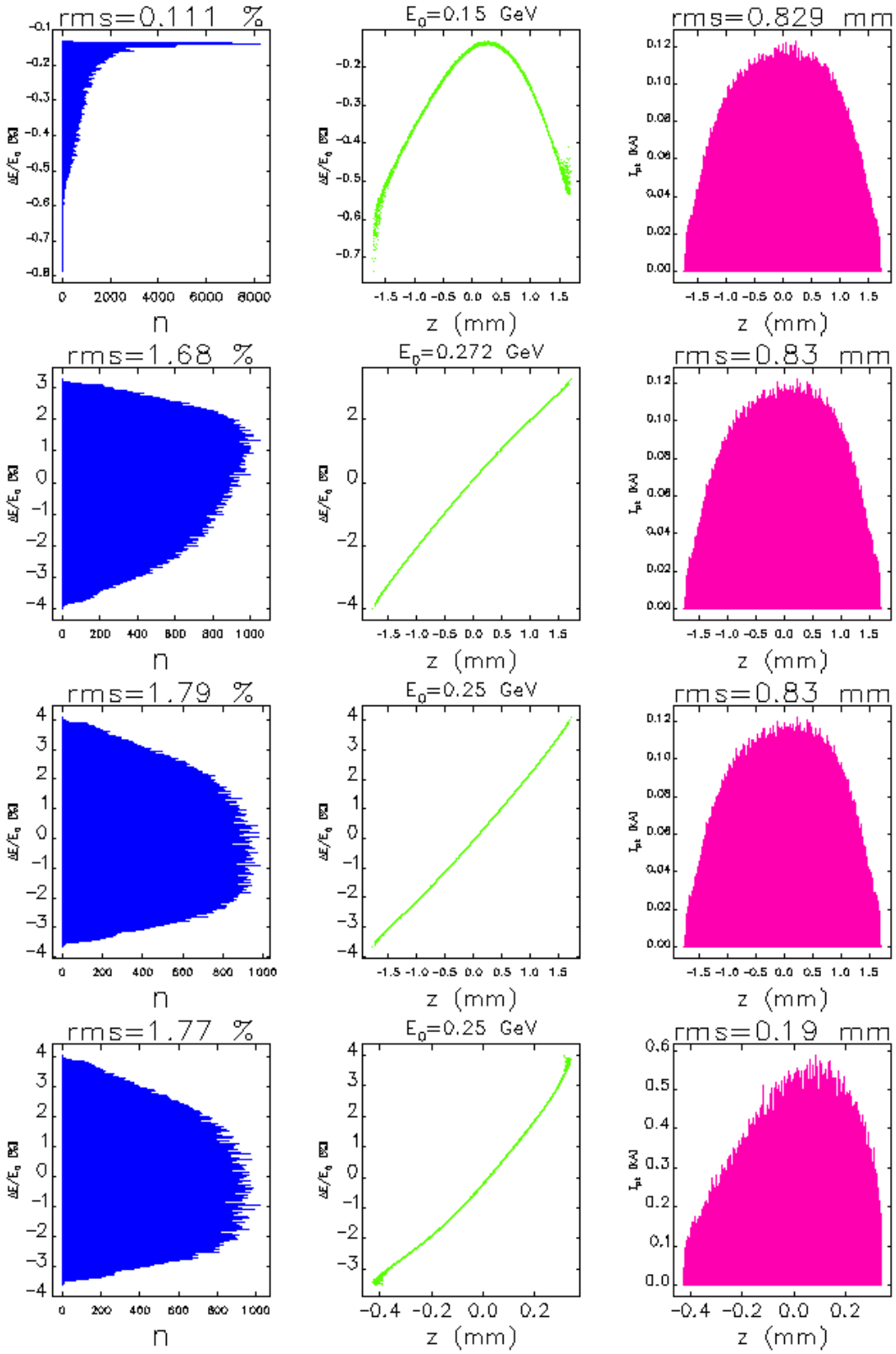

Figure 7.6 Energy (left column) and axial (right column) e^- distributions and longitudinal phase space (center column) after L0 at 150 MeV (top row), after L1 at 272 MeV (2nd row), after X-band at 250 MeV (3rd row), after BC1 at 250 MeV (4th row). Bunch head at left ($z < 0$).

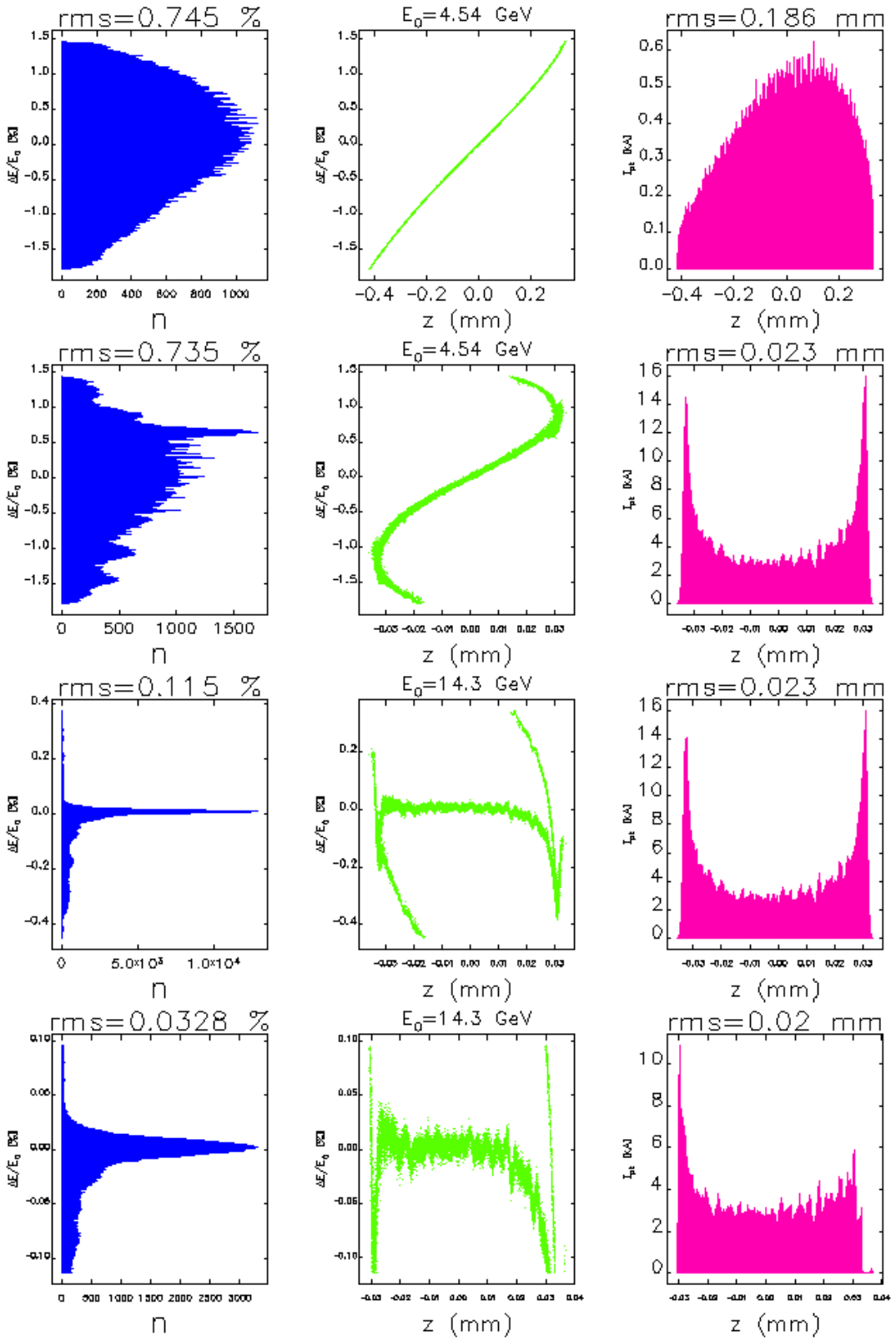

Figure 7.7 Energy (left column) and axial (right column) e^- distributions and longitudinal phase space (center column) after L2 at 4.54 GeV (top row), after BC2 at 4.54 GeV (2nd row), after L3 and DL2 at 14.35 GeV (3rd row), and at undulator entrance, but after 20% of charge is cut from energy tails to show beam core (4th row). Bunch head at left ($z < 0$).

The strong longitudinal wakefield in the L2-linac causes the extreme head and tail portions of the bunch, where the charge is lower, to have a slightly increased slope in the energy-z correlation (see 3rd-order curvature in top row of **Figure 7.7**, center plot). These head and tail sections are then over-compressed by the BC2 chicane (see 2nd row of **Figure 7.7**, center plot) and lead to the large current spikes in the z-distribution of **Figure 7.7** (2nd, 3rd and 4th row of right-side plots). It is difficult to add higher rf harmonics to correct this level, since the energy is high, the bunch is very short, and the offending correlations are now 3rd order, or higher. Finally, the longitudinal wakefield in L3 flattens most of the coherent energy spread into a tight core distribution shown in **Figure 7.7** (3rd and 4th rows). This is an important cancellation which provides the narrow energy spread and depends on the strength of the longitudinal wakefield in L3, the bunch charge, the rf phase of L2, and the bunch length in L2 and L3. Here the projected energy spread is reduced to <0.01% rms. In fact, a level of <0.1% rms is all that is required.

Calculations of the longitudinal wakefield for the micro-bunch in L3 are believed to be accurate to better than 10% (see **Section 7.9**). In order to allow for this potential error in the magnitude of the wakefield, the compression systems require a range over which they may be tuned. To demonstrate the tuning range required, a simulation has been run where the wakefield in L3 is *arbitrarily* scaled up by 20% (a factor of 1.2) and the compression systems were re-tuned. For this extreme case, the bunch length and energy spread at the end of L3 are completely recoverable to the conditions on the bottom row of **Figure 7.7**. The re-tuning produces new parameters, shown along with the nominal parameters in **Table 7.3**. This re-tuning works by increasing the L2 bunch length from 0.19 mm to 0.23 mm (moving L1 rf phase closer to crest), which increases the energy spread in BC2, and is then fully cancelled by the stronger L3-wake.

This simple test demonstrates the flexibility of the system and shows that a precise knowledge of the scale of the longitudinal micro-bunch wakefield is not absolutely necessary prior to construction. It does not, however, address how such a re-tune might be accomplished. Obviously, as in the case of machine commissioning, the beam and rf parameters need to be well measured and an empirical technique developed for tuning the system.

Table 7.3 Compression parameters before and after re-tuning. Changed parameters are in bold and are calculated with the L3 wakefield arbitrarily increased by 20%. The nominal (or unchanged) parameters (repeated from **Table 7.1**) are in standard type.

Beamline	E_{in}	E_{out}	$\sigma_{z\text{-in}}$	$\sigma_{z\text{-out}}$	$\sigma_{\delta\text{-in}}$	$\sigma_{\delta\text{-out}}$	$\lvert\varphi_{rf}\rvert$	$\lvert R_{56}\rvert$
	GeV	GeV	mm	mm	%	%	deg	mm
Linac-1	0.15	0.27	0.83	0.83	0.10	1.67/**1.46**	38.1/**35.4**	—
Linac-X	0.27	0.25	0.83	0.83	1.67/**1.46**	1.78/**1.58**	180	—
BC1	0.25	0.25	0.83	0.19/**0.23**	1.78/**1.58**	1.78/**1.58**	—	35.9/**38.4**
Linac-2	0.25	4.54	0.19/**0.23**	0.19/**0.23**	1.78/**1.58**	0.76/**0.94**	42.8/**42.2**	—
BC2	4.54	4.54	0.19/**0.23**	0.022	0.76/**0.94**	0.76/**0.94**	—	22.5/**22.3**
Linac-3	4.54	14.35	0.022	0.022	0.76/**0.94**	0.02	10.0	—

7.2.6 Beam Jitter Sensitivities

Although it has been optimized, the two-stage compressor system is still sensitive to beam phase and bunch population variations (jitter). **Figure 7.8** and **Figure 7.9** show the final peak current ($I_{pk} \propto Q/\sigma_z$), relative mean energy, $\langle \Delta E/E_0 \rangle$, relative rms energy spread, $(\Delta E/E_0)_{\rm rms}$, and bunch arrival time variations, $\langle \Delta t_f \rangle$, versus both rf-gun timing, Δt_0, and relative charge variations, $\Delta Q/Q_0$, at the injector.

Table 7.4 lists sensitivities for rf phase, rf voltage, and chicane bend power supplies for the various systems. Each sensitivity causes a +12% peak current increase or a +0.1% relative electron energy increase. The photon beam will change by twice this amount. These sensitivities will be used to form a tolerance budget. The pulse-to-pulse rf phase sensitivities per linac are quite tight. However, the common mode phase sensitivity for the entire system is an order of magnitude looser. The gun timing jitter sensitivity and charge jitter sensitivity have been minimized by a careful choice of the linac acceleration and compression parameters (see **Section 7.2.2**).

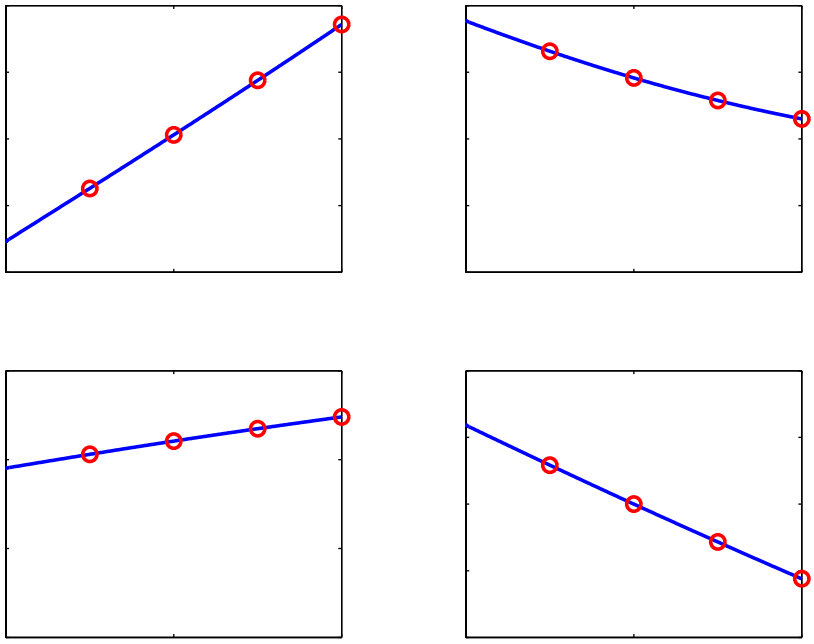

Figure 7.8 Beam energy, $\langle \Delta E/E_0 \rangle$; rms bunch length, σ_z; rms energy spread, $(\Delta E/E_0)_{\rm rms}$; and undulator arrival time jitter, $\langle \Delta t_f \rangle$; all versus gun-timing jitter, Δt_0. A 1.8-ps timing jitter causes a 12% bunch length (or peak current) jitter. A 1.3-ps gun timing jitter causes a 0.1% relative electron beam energy jitter in the undulator.

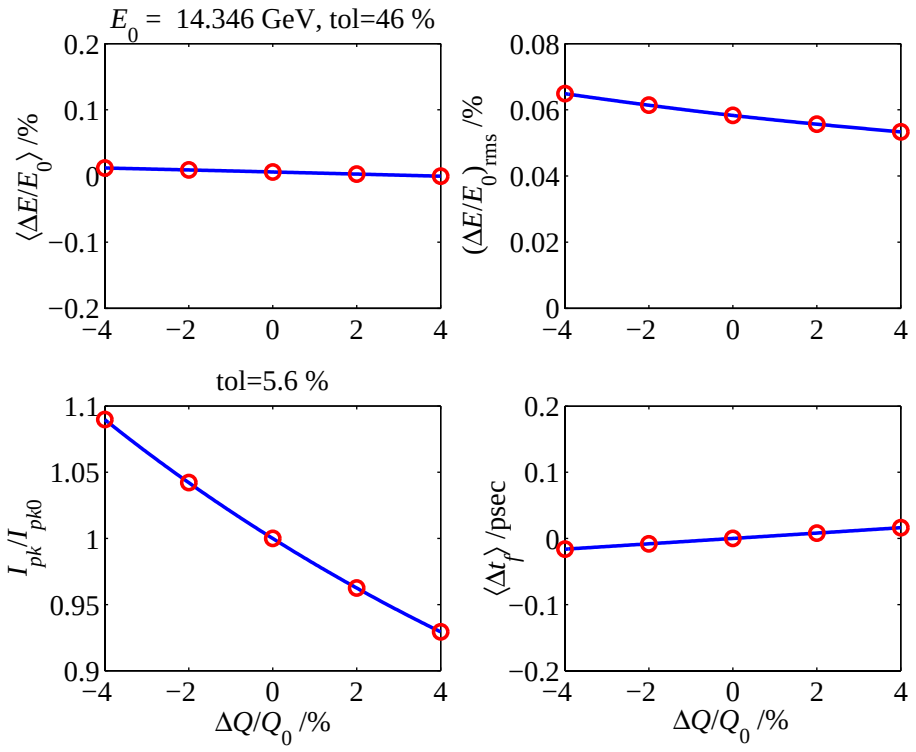

Figure 7.9 Same plots as **Figure 7.8**, but versus relative charge jitter, $\Delta Q/Q_0$, at the gun. A 5.6% charge jitter causes a 12% peak current jitter. The beam energy is, for all practical purposes, insensitive to charge.

The sensitivities listed in **Table 7.4** are used to generate a tolerance budget based on summing random, uncorrelated effects:

$$\sqrt{\sum_{i=1}^{n}\left(\frac{p_{\mathrm{tol}}}{p_{\mathrm{sen}}}\right)_i^2} < 1 \ . \qquad \textbf{(7.9)}$$

The tolerance to be chosen for each parameter is p_{tol}, and the weighting value taken from **Table 7.4** for each sensitivity is p_{sen}. For this budget, only the first fourteen ($n = 14$) sensitivities from **Table 7.4** are applied. If $p_{\mathrm{tol}} = p_{\mathrm{sen}}$ for all i, then the summation produces $n^{1/2}$, or $\sqrt{14}$-times larger peak-current or beam energy jitter than the 12% and 0.1%, respectively, used to calculate the above sensitivities. If the tolerances are chosen such that, $p_{\mathrm{tol}} < p_{\mathrm{sen}}$, for all i, a budget is formed where the less challenging tolerances (e.g., chicane bend power supplies) are pushed very much below their sensitivities, and the more challenging tolerances (e.g., L1 rf phase) are only slightly reduced. **Table 7.5** lists two possible tolerance budgets. If the first budget (column 3, titled $\mathbf{|\Delta I/I_0| < 12\%}$) is used, the relative peak-current fluctuations in the undulator will be held to <12% rms. If the second budget (column 4, titled $\mathbf{|\langle \Delta E/E_0 \rangle| < 0.1\%}$) is used, the final relative beam energy jitter in the undulator will be held to <0.1% rms. If the smaller tolerance from each column is applied (bold-type), both performance requirements ($|\Delta I/I_0| < 12\%$ and $|\langle \Delta E/E_0 \rangle| < 0.1\%$) will simultaneously be met.

The tolerances of **Table 7.5** apply only for pulse-to-pulse jitter, which is too fast to be corrected with fast feedback systems. For variations slower than a few seconds, such as those induced by a temperature change, it is quite simple to hold the beam energy constant in each bend system by monitoring a few beam position monitors (see **Section 7.8.4**). It is also possible to hold the bunch length constant after each of the two compressors by employing a bunch length monitor (see **Section 7.8.2**) and feeding back on both rf phase and voltage upstream of the bends.

Table 7.4 Individual rms sensitivities (p_{sen}) each cause a +12% peak current change (column 3) or +0.1% electron energy change at 14.35 GeV (column 4). All sensitivities listed are approximately linear. These are not tolerances, but individual sensitivities used to form a tolerance budget.

Parameter	Symbol	$\Delta I/I_0 = +12\%$	$\langle \Delta E/E_0 \rangle = +0.1\%$	Unit
mean L0 rf phase	φ_0	+0.67	−3.6	S-band deg
mean L1 rf phase	φ_1	+0.16†	−0.24†	S-band deg
mean LX rf phase	φ_X	−1.1	+12.	X-band deg
mean L2 rf phase	φ_2	−0.22‡	+0.36‡	S-band deg
mean L3 rf phase	φ_3	>+20	+0.47	S-band deg
mean L0 rf voltage	$\Delta V_0/V_0$	+0.29	−0.33	%
mean L1 rf voltage	$\Delta V_1/V_1$	+0.33	−0.34	%
mean LX rf voltage	$\Delta V_X/V_X$	−1.5	+1.9	%
mean L2 rf voltage	$\Delta V_2/V_2$	−1.0	+0.64	%
mean L3 rf voltage	$\Delta V_3/V_3$	>+20	+0.15	%
Gun timing jitter	Δt_0	−1.8	+1.3	psec
Initial bunch charge	$\Delta Q/Q_0$	−5.6	−46.	%
BC1 chicane	$\Delta B_1/B_1$	−0.15	+0.17	%
BC2 chicane	$\Delta B_2/B_2$	+0.76	+0.69	%
Initial bunch length	$\Delta\sigma_z/\sigma_{z_0}$	+5.3	−37.8	%
common L1/LX timing	$\varphi_X=4\varphi_1$	+0.43	−0.26	S-band deg
common net phase	$\varphi_0=\varphi_1=\varphi_X=\varphi_2=\varphi_3$	−4.0	+1.4	S-band deg

† The L1 phase sensitivities become 0.47° and 1.6° (left to right) if BC1 energy is held constant.

‡ The L2 phase sensitivities become 0.36° and 2.7° (left to right) if BC2 energy is held constant.

The tolerances are quite tight for many of the parameters, especially those systems driven by a single klystron (e.g., L1). Since the rf tolerances represent a demand on the average phase or average voltage over the klystrons of that linac, multiple-klystron linacs such as L2 and L3

actually have a per-klystron tolerance which is √26 and √45-times, respectively, looser than the tolerance listed. This means L2 has a per-klystron pulse-to-pulse jitter tolerance of 0.36˚ and 0.36%, and L3 has a per-klystron tolerance of 0.47˚ and 0.34%.

Table 7.5 Tolerance budget (p_{tol}) for <12% rms peak-current jitter (column 3) or <0.1% rms final e^- energy jitter (column 4). The tighter tolerance is in **BOLD** text and both criteria, $|\Delta I/I_0| < 12\%$ and $|\langle \Delta E/E_0 \rangle| < 0.1\%$, are satisfied if the tighter tolerance is applied. The voltage and phase tolerances per klystron for L2 and L3 are $\sqrt{N_k}$ larger.

Parameter	Symbol	$\|\Delta I/I_0\| < 12\%$	$\|\langle \Delta E/E_0 \rangle\| < 0.1\%$	Unit
mean L0 rf phase (2 klystrons)	φ_0	**0.10**	0.10	S-band deg
mean L1 rf phase (1 klystron)	φ_1	**0.10**	0.10	S-band deg
mean LX rf phase (1 klystron)	φ_x	**0.30**	0.8	X-band deg
mean L2 rf phase (28 klystrons)	φ_2	**0.07**	0.07	S-band deg
mean L3 rf phase (48 klystrons)	φ_3	1.0	**0.07**	S-band deg
mean L0 rf voltage (1-2 klystrons)	$\Delta V_0/V_0$	**0.10**	0.10	%
mean L1 rf voltage (1 klystron)	$\Delta V_1/V_1$	**0.10**	0.10	%
mean LX rf voltage (1 klystron)	$\Delta V_x/V_x$	**0.25**	0.25	%
mean L2 rf voltage (28 klystrons)	$\Delta V_2/V_2$	0.10	**0.07**	%
mean L3 rf voltage (48 klystrons)	$\Delta V_3/V_3$	1.0	**0.05**	%
BC1 chicane	$\Delta B_1/B_1$	**0.02**	0.02	%
BC2 chicane	$\Delta B_2/B_2$	**0.05**	0.05	%
Gun timing jitter	Δt_0	1.3	**0.7**	psec
Initial bunch charge	$\Delta Q/Q_0$	**2.0**	5.0	%

A complete simulation of FEL performance in the presence of machine jitter is described in **Section 7.6.3**, where 6D particle tracking is performed repetitively to test the jitter tolerance budget above. The detailed simulation includes CSR and suggests lowering the gun timing jitter tolerance to 0.5 psec, rather than 0.7 psec calculated above. Otherwise the budget is adequate.

The ability of the injector and the SLAC linac to achieve such pulse-to-pulse stability levels can be estimated by extrapolating from past SLC performance. With a beam energy feedback system installed at the end of the SLC linac, the remaining fast relative energy jitter was typically measured at <0.04% rms at 47 GeV with a 120 Hz machine repetition rate. This level of energy error is induced by a phase error of 0.16˚ rms (S-band) in the SLC bunch compressor rf system (at 42 MV), which provides an upper limit on the performance of this single klystron's rms phase stability. The phase stability is actually significantly better than 0.16˚ considering the additional effects of the remaining 210 klystrons and the typical 2% rms charge jitter (which by itself almost accounts for the 0.04% observed energy jitter). Measurements of the rf phase variations in the

SLAC linac are also presented in **Section 7.7.2**, where rms phase variations of <0.1˚ S-band are seen over a period of 10-20 seconds, as described in [13]. Some improvements to RF stability will be made to the linac as described in **Section 7.7**.

Variations much larger than 0.1˚ S-band have also been observed, but these levels are usually associated with changes over a much longer time scale, such as induced with day-night temperature and atmospheric pressure deviations. Energy and bunch-length feedback systems must address this long-term drift (see **Section 7.8.4**).

7.2.7 Energy Management and Overhead

Each linac section must operate with several spare klystrons to accommodate their inevitable failure rate (except L1 and LX, which each operate on just one klystron). **Table 7.6** lists, for each LCLS linac section, the total number of klystrons potentially available, N_K, the number of klystrons held in reserve, N_R, the nominal rf phase, $|\varphi|_i$, the average energy gain per klystron, $\langle \Delta E \rangle_K$, the beam loading energy loss at $Q = 1$ nC, ΔE_B, and the resulting maximum energy achievable, $E_{\max}$, (assuming an injection energy, E_i).

Table 7.6 Energy management parameters for the four main linac sections. The average energy gain is based on 19.3 MV/m and all LCLS-modified linac structure lengths.

Linac	N_K	N_R	$\|\varphi\|_i$ [deg]	$\langle \Delta E \rangle_K$ [GeV]	ΔE_B [MeV]	E_i [GeV]
L1	1	0	38.1	0.192	<1	0.15
LX	1	0	180	−0.022	<1	0.27
L2	28	2	42.8	0.230	28	0.25
L3	48	3	10.0	0.227	63	4.54

For the average energy gain calculation, all existing linac structure lengths are used, allowing for the linac modifications which eliminate the acceleration of three klystrons and remove several other 3-meter sections (see **Table 7.28**). This will nullify 920-MeV of unloaded energy gain (with respect to the pre-LCLS linac). For future non-LCLS linac operation, this energy is not easily recovered; however, the maximum energy available is still within ~1 GeV of the pre-LCLS linac maximum energy of ~50 GeV.

7.2.8 Alternate Parameters

7.2.8.1 Variable Bunch Charge

The nominal design parameters are described above for a 1-nC bunch, which produces SASE saturation with a 1.2-μm normalized slice emittance and a 3.4-kA peak current. In fact, the LCLS accelerator is flexible enough to be operationally re-configured for a wide variety of beam parameters. In this case, the term operational means that the new parameter set is ‘dialed-in’ from the control room, as opposed to hardware modifications in the tunnel. This flexibility is

demonstrated by studying the new machine parameters required over a wide range of bunch charge values.

The injector's beam emittance and bunch length is first estimated by applying scaling laws derived for a 1.6-cell S-band rf photo-cathode gun [14]:

$$\varepsilon_N\left[\mu\mathrm{m}\right] \approx 1.45 \cdot \sqrt{0.38 \cdot Q\left[\mathrm{nC}\right]^{4/3} + 0.095 \cdot Q\left[\mathrm{nC}\right]^{8/3} + 0.22 \cdot Q\left[\mathrm{nC}\right]^{2/3}}$$
$$\sigma_{z_0}\left[\mathrm{mm}\right] \approx 0.83 \cdot Q\left[\mathrm{nC}\right]^{1/3} \qquad \textbf{(7.10)}$$

Here Q is the bunch charge (nC), ε_N is the normalized rms emittance (μm), and σ_{z_0} is the initial rms electron bunch length (mm) after the gun. The last term in the emittance relation represents a thermal emittance, which scales with the laser spot radius on the cathode. The bunch length scaling constant has been increased here (0.63 mm in reference [14] becomes 0.83 mm), to a less challenging level, in order to be consistent with the 1-nC nominal design described above.

The peak current required for SASE saturation at ~87 m, is given approximately by (see **Chapter 5**)

$$I_{pk}[\mathrm{A}] \approx 233 \cdot \varepsilon_N^3 + 1343 \cdot \varepsilon_N^2 + 834 \cdot \varepsilon_N + 63 \ , \qquad \textbf{(7.11)}$$

where the slice energy spread is assumed to be <0.02% rms, and the mean beta function in the undulator is ~18 m. At the nominal 1-nC charge, the emittance is $\varepsilon_N \approx 1.2\ \mu$m, and the required peak current is $I_{pk} \approx 3400$ A.

For a reduced bunch charge, the emittance, initial bunch length, and required peak current are estimated from **Eqs. (7.10)** and **(7.11)**. A fast optimization linac design code (described in **Section 7.2.2**) is then used to find a new set of acceleration and compression parameters which can provide SASE saturation at the same 87-meter point, and also optimize beam stability. Alternate scaling scenarios are also possible, but this simple example is used here as a demonstration of the configuration flexibility in the LCLS accelerator. **Table 7.7** lists the various machine parameters and a few 'jitter' sensitivities (see **Section 7.2.6**) for six different values of the bunch charge ranging from 0.1 to 1.0 nC. In each case, full 2D tracking calculations are used to verify that the final energy (14.35 GeV), peak current (listed), and energy spread (<0.02% rms) are obtainable. Obtaining the smaller values of emittance with a lower charge needs experimental verification, and various beam diagnostics need to provide adequate resolution at the lower charge, but in any case, the linac design is seen to be quite flexible.

The extreme point at 0.1 nC may be too low, but many of the other low-charge configurations are interesting since the jitter tolerances (last 3 rows) are generally looser. The smaller emittance with lower charge is not necessarily more difficult to preserve in the linac, since the reduced charge eases the effects of coherent synchrotron radiation in the chicanes and transverse wakefields in the linacs. In addition, the shorter initial bunch length allows weaker chicanes and lower values of correlated energy spread throughout the linac sections, both of which also ease emittance preservation issues.

Table 7.7 Machine parameters for six different values of bunch charge and constant saturation length. The final projected relative energy spread is <0.02% rms in all cases.

Bunch Charge →	**0.1**	**0.2**	**0.4**	**0.6**	**0.8**	**1.0**	**nC**
Initial bunch length	390	491	619	709	780	830	μm
Final bunch length	8.3	14	21	23	23	22	μm
Norm. slice emittance	0.54	0.60	0.74	0.89	1.04	1.20	μm
Peak current	0.95	1.11	1.52	2.03	2.66	3.40	kA
L1 rf phase	−35.9	−33.1	−34.6	−27.5	−32.4	−38.1	deg-S
L2 rf phase	−13.1	−27.2	−40.6	−41.9	−42.0	−42.8	deg-S
L3 rf phase	−7.4	−8.2	−7.6	−10.0	−9.7	−10	deg-S
R_{56} of BC1	−41.2	−47.7	−45.9	−60.4	−47.7	−35.9	mm
R_{56} of BC2	−63.6	−33.1	−20.6	−22.5	−23.1	−22.5	mm
energy spread in BC1	0.82	0.91	1.18	0.98	1.31	1.78	%
energy spread in BC2	0.08	0.14	0.29	0.43	0.58	0.76	%
bunch length after BC1	57	62	80	119	157	195	μm
Rms gun $\Delta t_0 \rightarrow 12\%\ \sigma_z$	1.3	5.8	11.	4.7	6.5	4.0	psec
Rms gun $\Delta t_0 \rightarrow 0.1\%\ \Delta E/E_0$	5.8	3.8	2.8	3.4	2.0	1.4	psec
Rms $\Delta Q/Q \rightarrow 12\%\ I_{pk}$	4.9	11.	—	7.0	—	6.0	%

7.2.8.2 Electron Chirp to Facilitate X-Ray Pulse Compression

The nominal final electron bunch length at 1 nC is 22 μm rms or 230 fsec FWHM. If the entire electron bunch achieves SASE saturation, the x-ray pulse length will also be 230 fsec FWHM. This may be too long for some experiments, so an option to reduce the photon pulse length to ~50 fsec is desirable.

Further reduction of the electron bunch length is possible with re-configuration of the compression parameters, but several limitations begin to appear when a significantly shorter electron bunch is used, such as increased horizontal emittance dilution due to CSR in the compressors, increased resistive-wall and roughness wakefields in the undulator, and increased peak-current jitter sensitivity to linac and injector variations. An alternate way in which to shorten the x-ray pulse is to use the nominal electron bunch length, but provide a linear energy gradient (chirp) along the bunch so that the x-ray pulse, which will then also be chirped, may be shortened using optical compression techniques.

An electron chirp can be added in several different ways. Unfortunately, the most intuitive way, shifting the L3-linac rf phase farther off acceleration crest, does not add a significant chirp due to the very short bunch length compared with the S-band rf wavelength. Another possibility involves increasing the BC2 chicane strength to 'over-compress' the bunch, such that the electron bunch length is again set at 22 μm, but the remaining energy-time correlation in the bunch has reversed sign, with respect to the nominal case (see nominal case in **Figure 7.7**). With over-

compression, the L3 longitudinal wakefield will now add to the correlated energy spread, rather than canceling it. Thus, a large correlated electron energy spread (chirp) of ~2% FWHM can be generated at 14.35 GeV. The over-compression in the BC2 chicane, however, forces the bunch to pass through its minimum length (a few microns) inside the chicane, which may destroy the horizontal emittance with the potentially stronger CSR forces. This case requires a subtle calculation including the transverse beam dimensions and cannot, at present, be relied upon to accurately predict machine performance. Therefore, over-compression is presently viewed as a possible option needing experimental verification before it is seen as a realistic chirp strategy.

The most promising method of producing a significant chirp is to reduce the bunch charge from 1 nC to 0.6 nC and operationally re-configure the linac parameters. The reduced bunch charge makes the L3 wakefields weaker, which helps to leave some chirp in the electron beam after L3. The re-configuration is used to further amplify the chirp to ~1% FWHM. This 1% electron chirp may then be used to compress the x-ray pulse by a factor of ~5, to a pulse length of ~50 fsec FWHM (see **Chapter 9**).

The reduced charge also allows the initial bunch length, prior to BC1, to be reduced from 0.83 mm to 0.71 mm rms, and the emittance to be slightly reduced from 1.2 μm to 0.9 μm. This keeps SASE saturation at ~87 meters with a 2.1-kA peak current [see **Eqs. (7.10)** and **(7.11)**]. The machine parameters and sensitivities associated with this configuration are shown in **Table 7.8** along side the nominal parameters. The final 'slice' energy spread in both cases is <0.01% rms, but the gun-timing tolerance is, unfortunately, more challenging in the 0.6-nC case. The 2D tracking output at 14.3 GeV is shown in **Figure 7.10**, where the bunch length is 23 μm, but the correlated energy spread is large and linear at 1% FWHM. Saturation should occur for the leading half of the bunch where the peak current exceeds 2.1 kA. Various other scenarios are also possible, especially if the required final chirp level is reduced.

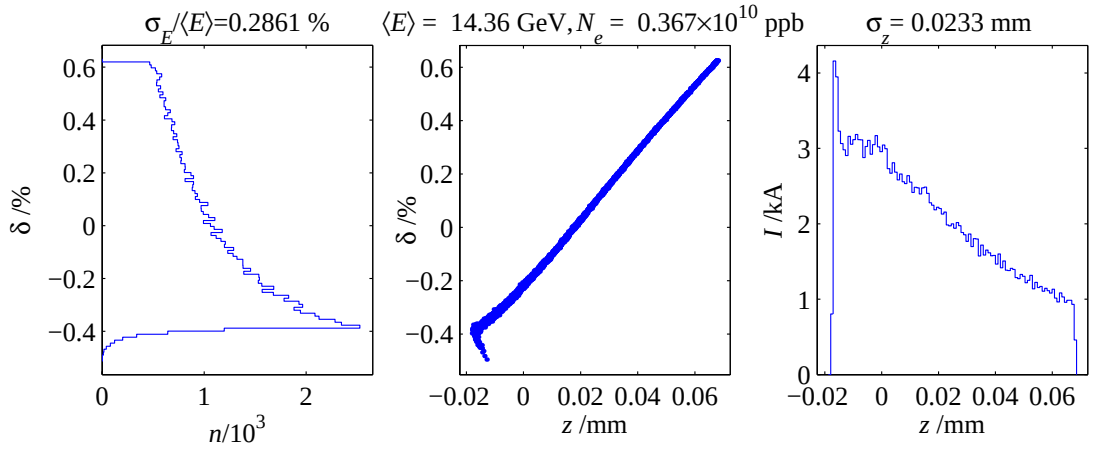

Figure 7.10 Chirped electron beam: energy (left) and axial (right) e^- distributions and longitudinal phase space (center column) at undulator entrance with a reduced charge of 0.6 nC and a desired 1% FWHM electron energy chirp.

Table 7.8 Machine parameters for a 1%-chirped electron bunch and a charge of 0.6 nC juxtaposed against the nominal, 1-nC un-chirped parameters.

Bunch Charge →	**0.6 nC (chirp)**	**1 nC (nominal)**	**units**
Initial bunch length	710	830	μm
Final rms bunch length	23	22	μm
Norm. rms slice emittance	0.9	1.2	μm
Peak current	2.1	3.4	kA
X-band rf voltage	5	22	MV
L1 rf phase	−22.8	−38.1	deg-S
L2 rf phase	−41.3	−42.8	deg-S
L3 rf phase	−10.0	−10.0	deg-S
R_{56} of BC1	−60.1	−35.9	mm
R_{56} of BC2	−20.7	−22.5	mm
energy spread in BC1 (rms)	0.69	1.78	%
energy spread in BC2 (rms)	1.35	0.76	%
energy spread in undulator (**FWHM**)	1.0	0.05	%
bunch length after BC1 (rms)	300	195	μm
rms gun $\Delta t_0 \rightarrow 12\%\ \sigma_z$	0.50	4.0	psec
rms gun $\Delta t_0 \rightarrow 0.1\%\ \Delta E/E_0$	0.64	1.4	psec
rms $\Delta Q/Q_0 \rightarrow 12\%\ I_{pk}$	17.	6.0	%

This scenario provides the ability to compress the x-ray pulse without adding significant technical risk to the preservation of the 6D electron phase space density. Other scenarios are also possible, including the full 1-nC bunch charge and a negative chirp sign, an option which has been simulated in some detail but not presented here. The temporal distribution of the negatively chirped case is less uniform across the bunch and the energy-time correlation is less linear.

7.2.8.3 Long Wavelength SASE Radiation

The LCLS can also be configured for longer undulator radiation wavelengths in a continuum from 1.5 Å up to a maximum of ~15.0 Å. The 15-Å limit of this range is easily arranged by switching off the rf acceleration in the L3-linac, re-scaling the bends and quadrupole magnets beyond BC2, and passing the 4.54-GeV electron beam through the permanent magnet undulator.

At a longer wavelength, the SASE gain saturates in a much shorter distance than at 1.5 Å. This allows the electron beam parameters to be significantly relaxed at 15 Å. With the saturation length chosen in the very safe range of ~60 meters of undulator, the electron beam emittance can then be relaxed to $\gamma\varepsilon_{x,y} \approx 3\ \mu$m and the peak current, with less compression, to 1.9 kA. With the full 1-nC charge, the final bunch length is then 45 μm rms. Other scenarios are possible, including lower charge, but the long (45 μm) bunch relaxes rf phase and voltage jitter tolerances in the

linac, so that the entire linac and injector configuration is technically much less challenging than that required at 1.5 Å.

The final absolute energy spread will decrease by a factor of two with the reduced compression (from ~2.8 MeV to 1.4 MeV), while the relative energy spread will increase with the reduced beam energy (from 0.02% to 0.03%). The very small energy chirp along the electron bunch can be approximately maintained, even after the L3 rf is switched off.

The beta-match at the undulator entrance, due to its permanent magnet focusing, needs to be adjusted to produce ~6-meter average undulator beta functions, as opposed to the ~18-meter beta functions at 1.5 Å (14.3 GeV). The re-match is accomplished using the four QM35-38 quadrupoles at undulator entrance (last four quads at right of **Figure 7.36**).

Table 7.9 lists the machine parameters for the 15-Å case alongside the nominal 1.5-Å case. Parameters not listed here are the same in the two configurations. The same injector beam, shown at top of **Figure 7.6**, is tracked in 2D through the re-configured LCLS accelerator with the L3-linac rf switched off. The final longitudinal phase space at the undulator entrance, at 4.54 GeV, is shown in **Figure 7.11**. The temporal distribution is very flat with a nearly constant 2-kA peak current.

Table 7.9 Machine parameters for 15-Å SASE radiation with a saturation length of ~60 m juxtaposed against the nominal 1.5-Å configuration, both with 1-nC of charge. Energy sensitivity is worse (×3) at left, but also more tolerable (×3) at 15 Å.

Bunch Charge →	**15 Å (long λ_r)**	**1.5 Å (nominal)**	**units**
Final rms bunch length	45	22	μm
Norm. rms slice emittance	3.0	1.2	μm
Peak current	1.9	3.4	kA
L1 rf phase	−35.1	−38.1	deg-S
L2 rf phase	−40.6	−42.8	deg-S
R_{56} of BC1	−40.0	−35.9	mm
R_{56} of BC2	−21.7	−22.5	mm
energy spread in BC1 (rms)	1.59	1.78	%
energy spread in BC2 (rms)	0.72	0.76	%
energy spread in undulator (rms)	0.03	0.02	%
bunch length after BC1 (rms)	200	195	μm
rms gun $\Delta t_0 \rightarrow 12\%\ \sigma_z$	2.3	4.0	psec
rms gun $\Delta t_0 \rightarrow 0.1\%\ \Delta E/E_0$	0.4	1.4	psec
rms $\Delta Q/Q_0 \rightarrow 12\%\ I_{pk}$	11	6.0	%

This is just one possible long-wavelength configuration. Many long-wavelength scenarios are possible including reduced charge, increased peak current, and reduced emittance. This specific

parameter set is described because of its potential as an LCLS startup configuration, with reduced technical challenges on all fronts: injector, linac, and undulator.

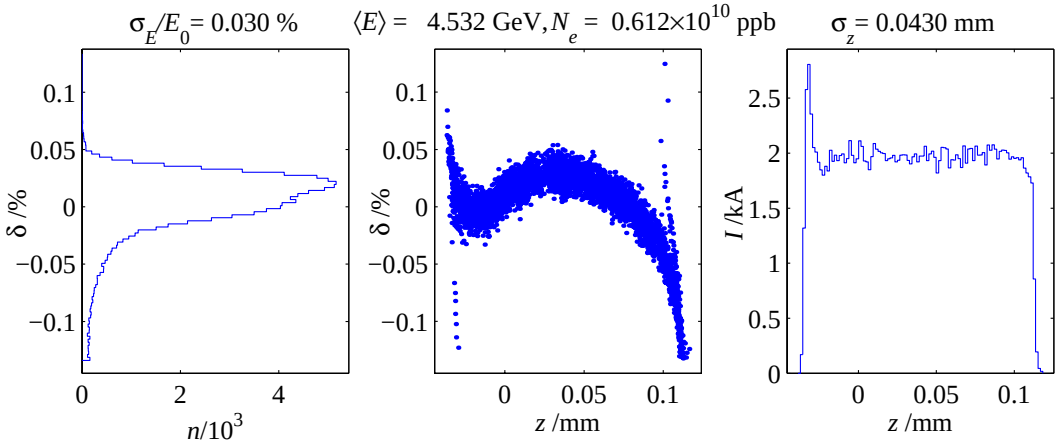

Figure 7.11 Longitudinal phase space of 4.54-GeV electron beam at undulator entrance after re-optimizing the LCLS accelerator to the 15-Å configuration described above.

7.3 Transverse Beam Dynamics

The LCLS accelerator is composed of four separate S-band linac sections L0, L1, L2, and L3 (ignoring the very short X-band section). Each of these linacs requires an individual lattice design in order to minimize emittance dilution due to transverse wakefields and momentum dispersion, both of which are generated through component misalignments. Each linac section has its own particular beam parameters, which motivate the optical design of that linac. For example, a large beam energy spread and short bunch length suggest weak focusing with large quadrupole spacing. **Figure 7.12** shows the nominal rms energy spread and bunch length along the entire LCLS accelerator from the end of L0 at 150 MeV to the entrance of the undulator at 14.35 GeV.

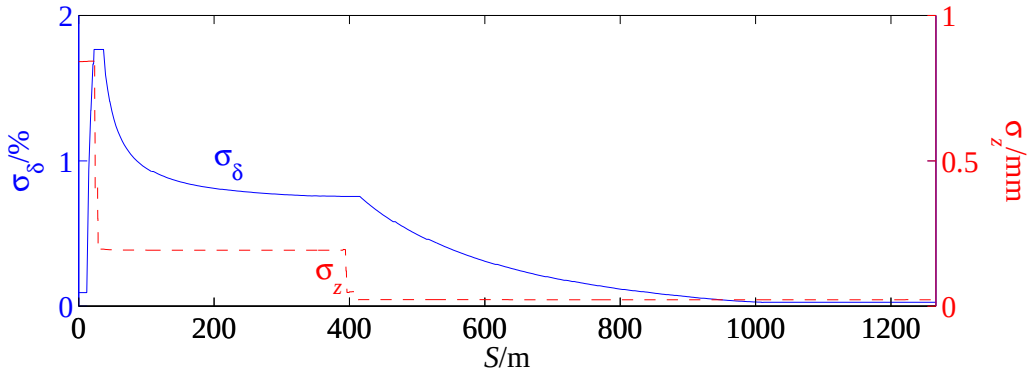

Figure 7.12 Nominal rms energy spread (solid-blue) and rms bunch length (dash-red) along the entire LCLS accelerator from L0-exit at 150 MeV to undulator entrance at 14.35 GeV.

Table 7.10 summarizes the four linacs and their various beam parameters. The final energy after L3 is variable from 4.5 to 15 GeV through appropriate phasing and rf power. The rf phase angles of the various linacs as well as their lengths are chosen in a computer optimization which is described in **Section 7.2.2**.

Table 7.10 Beam parameters of the four separate S-band linac sections (plus X-band linac, LX).

Beam Parameter	Unit	L0	L1	LX	L2	L3
Initial energy	GeV	0.007	0.150	0.272	0.250	4.54
Final energy	GeV	0.150	0.272	0.250	4.54	4.54-15
Active linac length	m	6	9	0.6	329	553
rf phase (crest at 0)	deg	−2	−38.1	180	−42.8	−10
Initial rms energy spread	%	0.20	0.10	1.64	1.78	0.76
Final rms energy spread	%	0.10	1.64	1.78	0.76	0.02
rms bunch length	mm	0.83	0.83	0.83	0.19	0.022

7.3.1 The L0-Linac

A more complete description of the L0-linac is given in **Chapter 6**. Linac-0 provides the initial acceleration and transverse emittance compensation from the rf photocathode gun. It is a new beamline constructed at a 35˚ angle with respect to the existing SLAC linac at the start of sector-21 and is situated in an existing, off-axis linac housing. This space was provided in the original SLAC-linac design, which was built with two off-axis injector enclosures at both the one-third and two-thirds locations along the linac (at the end of both sectors 10 and 20). Linac-0 is composed of two 3-meter acceleration sections, each powered by an separate klystron (20-7 and 20-8), and nominally accelerates the electron beam to 150 MeV. It is a space charge dominated system including solenoid focusing, but no quadrupole magnets prior to the 150-MeV point. Following L0 is an adjustable matching section and a transverse emittance diagnostic section, ED0 (see **Section 7.8.1**). The achromatic bend system, DL1 (see **Section 7.5.1**), bends the beam 35˚ onto the SLAC linac axis and into the L1-linac section, which starts at the 21-1b location. The two DL1 bends are located at the 21-1a location where space already exists with no 3-meter rf-section installed there.

The 35° DL1 bend system provides energy and energy spread measurement capability prior to injection into the L1-linac. An energy stabilizing feedback system, a switchable beam dump, and a bunch length monitor will also be located here (see **Secs. 7.5.1** and **7.8.4**).

7.3.2 The L1-Linac

L1 initiates the compression process by accelerating from 150 MeV to 272 MeV off crest, thereby generating the necessary linear energy-z correlation so the first chicane, BC1, will compress the bunch. The L1-linac is composed of three existing 3-meter rf structures 21-1b, 21-1c, and 21-1d (the 21-1a section was never installed in anticipation of just such an intermediate

injector). Because of the large off-crest rf phase angle and the relatively long bunch, the rms energy spread in L1 rapidly increases from 0.1% to 1.7%. Therefore, dispersion generated by misaligned quadrupoles, and transverse wakefields generated by misaligned rf structures, are both potential sources of emittance dilution. At this energy, however, space charge forces are insignificant (see **Chapter 6**).

To choose the best focusing lattice for L1, several lattice designs have been simulated using *Liar* [15] and *Elegant* [10]. These computer programs calculate the transverse emittance dilution along a linac and include both longitudinal and transverse wakefields, random quadrupole, BPM, and rf-structure misalignments and the dispersion these generate. They also provide various trajectory correction algorithms.

Several different quadrupole spacing schemes were simulated (see **Section 7.3.2** of reference-[16]), with a simple 3-meter spacing settled upon. In order to insert quadrupole magnets and BPM-steering pairs at a 3-meter spacing, 18-cm of waveguide will be cut off from the downstream ends of the first two L1 rf sections (21-1b and 21-1c). This same cut-off technique has been used in the past for various SLC modifications.

In order to find the best L1-linac focusing strength, the betatron phase advance per cell (there are only 1.5 cells) was varied from 15° to 90° in 15° steps. The simulations are made with *Liar* and use 300-μm rms random quadrupole, BPM, and rf-structure transverse misalignments (with gaussian distributions cut at 3-σ). These are pessimistic conditions in order to optimize the lattice. The same 10 seeds were then run for each lattice, and one-to-one steering was applied at each BPM in both planes. A horizontal and vertical corrector, and a BPM which reads both x and y, are used near each of the three L1 quadrupole magnets.

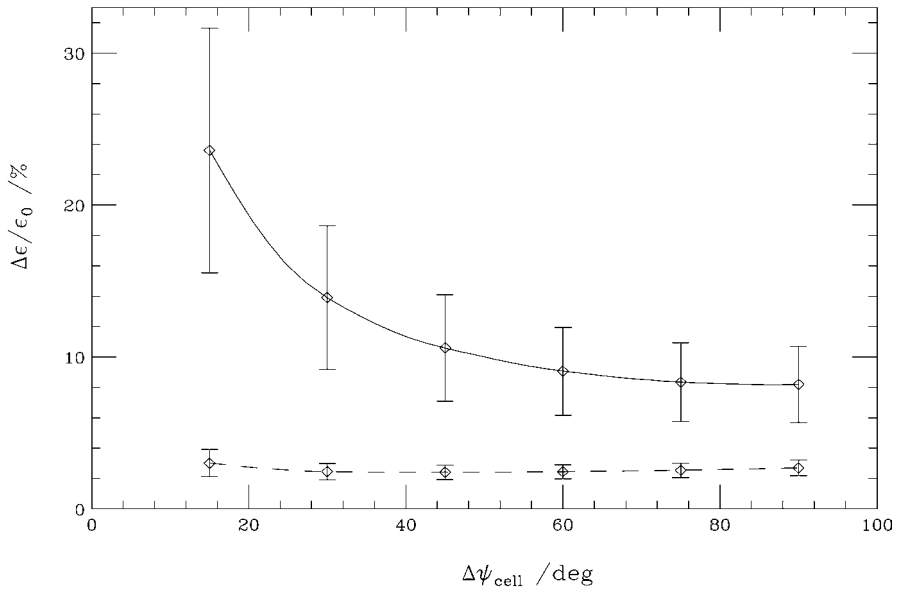

Figure 7.13 Horizontal relative emittance growth (from *Liar*) versus phase advance/cell for L1 lattice over 10 seeds (solid: wakes-ON, dash: wakes-OFF). Quadrupole, BPM, and rf-structure misalignments of 300 μm rms and one-to-one steering are applied. Vertical behavior (not shown) is similar. Error bars show spread over ten seeds.

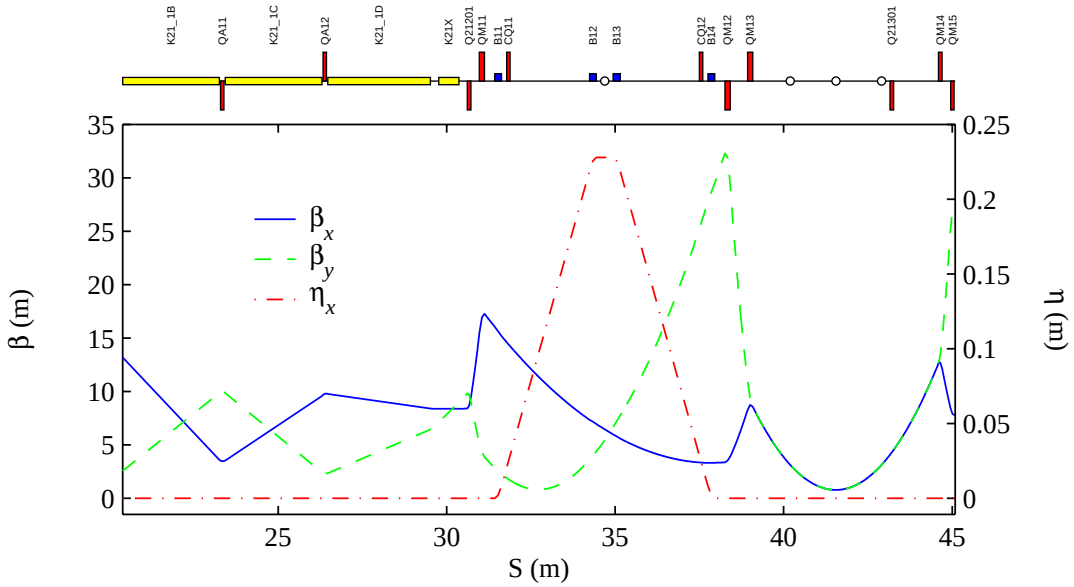

Figure 7.14 Dispersion and beta functions along L1 (S < 30 m) and through BC1 chicane and ED1 emittance diagnostic section (S > 30 m). L1 quad spacing is 3-meters at 75°/cell phase advance. X-band is rf at $S \approx 30$ m. Small circles in top schematic indicate profile monitors.

In fact, beam-based alignment techniques in the SLC linac have been used to align quadrupoles and BPMs to ~100 μm rms [17]. **Figure 7.13** shows horizontal emittance growth versus phase advance/cell with and without transverse wake effects. Error bars are the error on the mean over the 10 seeds. Beta functions and beamline layout are shown in **Figure 7.14** for the lattice at the chosen 75°/cell.

Included in **Figure 7.14**, and following L1, is the BC1 bunch compressor chicane (see **Section 7.4.1**). BC1 is followed by a transverse emittance diagnostic section (ED1, see **Section 7.8.1**), which is included in order to measure the transverse emittance immediately after BC1.

7.3.3 The L2-Linac

The energy spread is large (0.8-1.8%) over the entire 350-meter length of L2, and the bunch is only partially compressed, making L2 the most problematic linac section with respect to transverse emittance dilution. The L2-linac begins at the 21-3b location and ends at 24-6d. The lattice choice for L2 was made using the computer codes *Liar* and *Elegant* and varying the phase advance per cell and the quadrupole spacing. Several spacing schemes were tested including (1) the existing 12-meter spacing, (2) a 6-meter quadrupole spacing over the full L2 length, and (3) a 6-meter spacing for the first 60 meters followed by a 12-meter spacing. Although the shorter quadrupole spacing in the first 60 meters reduced the wakefield induced emittance growth, the reduction was not large enough compared with the increased cost of modifications required. Furthermore, well tested and very effective emittance correction techniques are also possible and are described below.

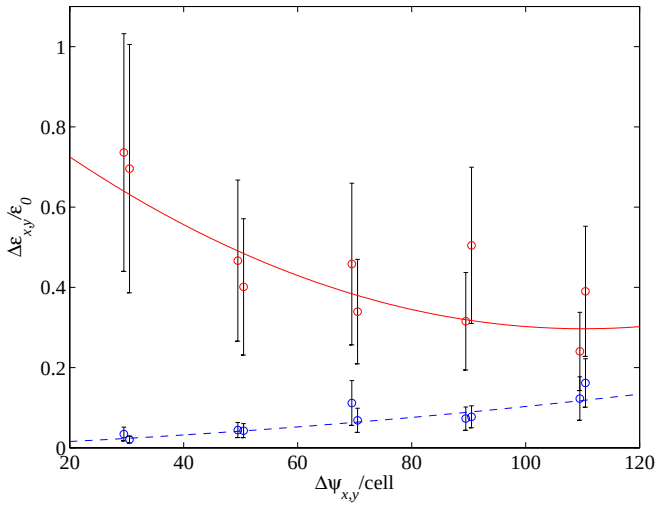

Figure 7.15 Relative mean emittance growth (*x* and *y*) versus phase advance/cell for L2 over 10 seeds (solid-red: wakes ON, dash-blue: wakes OFF). Points with slight left-offset are *x* and right-offset are *y*. Quadrupole, BPM, and rf-structure misalignments of 300 μm rms are used and one-to-one steering (no 'bumps' applied). Error bars show statistical error on mean value over 10 seeds.

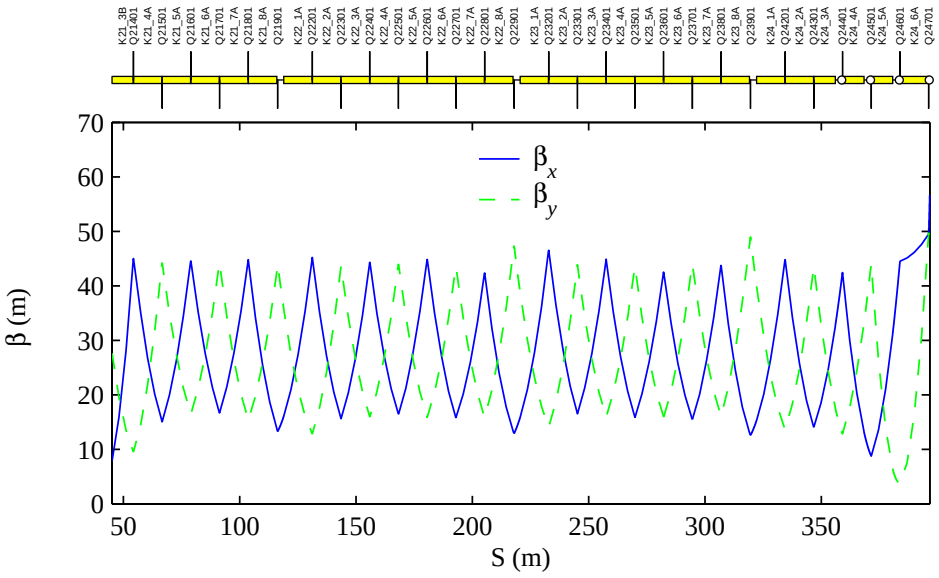

Figure 7.16 Beta functions along L2 at 55°/cell phase advance and 12-meter quadrupole spacing. Small circles in schematic at top indicate profile monitors (wire-scanners) for emittance measurement at the end of L2 (L2-ED).

Using *Liar* to study emittance correction schemes, it was found that even though the L2 emittance growth (not including CSR in the chicanes) can easily reach 50%, localized trajectory 'bumps' can be used to restore the emittance to just 5-10% dilution. **Figure 7.15** shows emittance dilution, with trajectory corrections but no emittance corrections applied, versus phase advance per cell for the existing 12-meter quadrupole spacing over the length of L2. The minimum emittance growth occurs above 90°/cell. The mean growth at 90°/cell is ~30% in each plane if no

further correction is attempted. The choice of 55°/cell is described below. Although **Figure 7.15** suggests a stronger lattice, the improvement is not significant with respect to the statistical spread shown by the error bars. The weaker lattice was chosen for reasons of convenience and in order to reduce the trajectory jitter caused by vibrating quadrupole magnets. A stronger lattice is easily installed simply by changing power supply settings.

Figure 7.16 shows the beta functions through the L2-linac at 55° per cell and a 12-meter quadrupole spacing. Four profile monitors are indicated at the end of L2 as small circles on the schematic. These are wire scanners used to measure the L2 output emittance as correction bumps are empirically optimized. This trajectory-based emittance correction scheme is similar to that used in the SLAC linac for SLC operations [18]. Simulations of trajectory-based emittance corrections were performed using *Liar* with an older design of the L2-linac in reference [16]. In this study the mean value of the emittance over 100 random misalignment seeds was reduced from ~100% to <10% in each plane.

No new magnets are needed in the L2-linac. The existing quadrupoles are used at their present locations. One new low current (25 A) bulk quadrupole power supply is installed in each of sectors 23 and 24 in order to achieve rms regulation tolerances of <0.5% (not easily achieved with the existing 200-Ampere bulk supply per sector). In addition, the existing 20-ampere booster power supplies (one per quadrupole) will be used to adjust the focusing within a sector.

Quadrupole roll and gradient error tolerances are loose at ~0.5° and ~1% rms, respectively ($\Delta\varepsilon/\varepsilon_0 \approx 2\%$ total over 30 quadrupoles). Magnet transverse vibration tolerances are ~1 μm rms. Tolerances on field harmonics (e.g., 12-pole) in the quadrupoles are extremely loose.

7.3.4 The L3-Linac

The L3-linac begins at 25-1a and ends at the end of sector-30 (30-8c). Eight 3-meter sections from 24-7a through 24-8d are removed to install the long BC2 bunch compressor chicane. Note that the section at 25-1c was removed years ago for the NPI gun, but might now be replaced to partially compensate for the 24-7 and 24-8 removals. The short bunch of 22 μm in L3 effectively eliminates transverse wakefields as a source of emittance dilution, and the rms energy spread shrinks from 0.8% down to <0.1% due to the strong longitudinal wakefield in L3. (Note, the rf phase in L3 is set at −10° for slightly improved energy stability, not to alter the beam energy spread.) In this case the dominant emittance dilution mechanism is due to momentum dispersion generated by quadrupole and BPM misalignments. This suggests a weak focusing lattice. *Liar* simulations were run for L3 using the existing SLAC linac 12-meter quadrupole spacing, but varying the phase advance per cell over the set 20°, 30°, 40°, 60° and 90°. **Figure 7.17** shows the horizontal relative emittance growth versus phase advance per cell for L3 with and without transverse wakefield effects. This clearly demonstrates the weak transverse wakefield effect due to the extremely short bunch in L3. Large quadrupole, BPM, and rf-structure misalignments of 300-μm rms were used as well as a one-to-one steering algorithm and the nominal undulator energy of 14.3 GeV.

A phase advance per cell of 33° is chosen for L3 since it is near the minimum emittance dilution. This particular phase (33.5˚/cell horizontally) also allows the center of the last bend of the BC2 chicane to be separated by $2n\pi$ in total horizontal betatron phase from the center of the first bend in the DL2 dogleg. In this way the correlated emittance growth effects of coherent synchrotron radiation in the two bend systems (BC2 and DL2) might be approximately cancelled, rather than added as they would with a $(2n+1)\pi$ separation (see **Section 7.4.2** and **7.5.2**). This even-π symmetry works because the first bend of DL2 bends in a 'left' direction whereas the first bend-pair of DL2 bends to the 'right'.

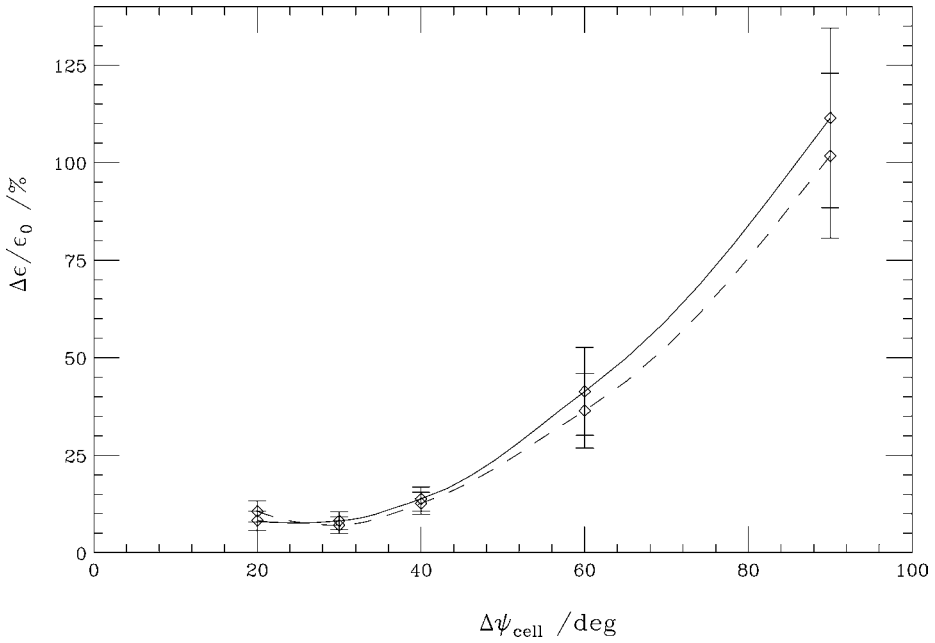

Figure 7.17 Mean relative emittance growth versus phase advance/cell for L3 and 12-meter quadrupole spacing over 10 seeds (solid: wakes ON, dash: wakes OFF). Quadrupole, BPM, and rf-structure misalignments of 300 μm rms were used as well as one-to-one steering (no bumps applied). The phase chosen is 33°/cell.

The L3 phase advance per cell in the vertical plane (33.0˚/cell) is chosen in order to set a $(2n+1)\pi/2$ vertical phase advance between a transverse rf deflecting structure in 25-5a (used for bunch length measurements—see **Section 7.8.2**) and the profile monitor PR31 in DL2. This allows the transverse rf to be used as a diagnostic to analyze the details of the final longitudinal phase space population just prior to the undulator.

The 33˚/cell phase advance also optimizes the phase advance separation of the existing sector-28 wire scanners for an improved x and y emittance resolution. The first and last wires will be relocated to set each wire-to-wire separation at 1.5 cells, or 45° (see **Section 7.8.1**). Beta-functions and beamline layout are shown in **Figure 7.18** for 33°/cell.

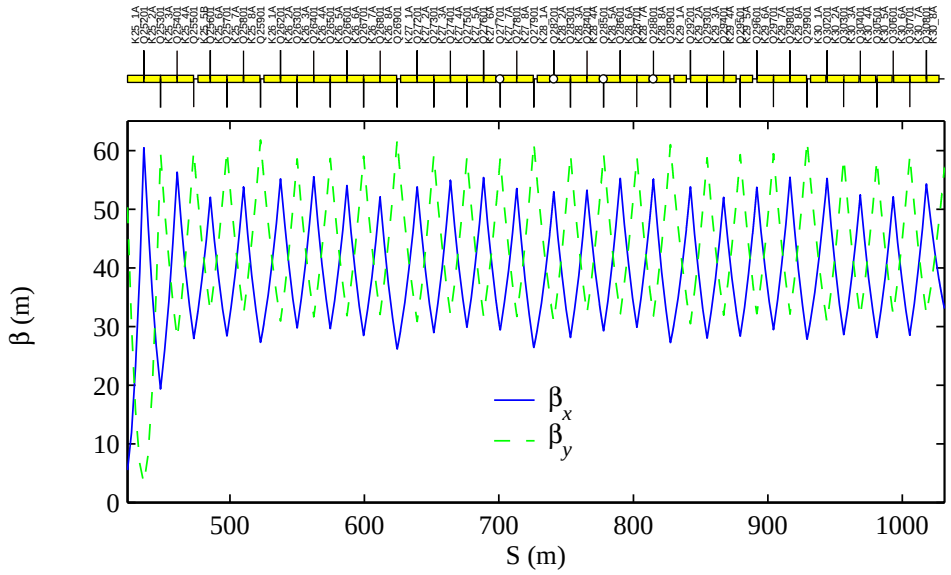

Figure 7.18 Beta functions along L3 at a phase advance of 33°/cell. Four existing sector-28 wire scanners are indicated by small circles in schematic at top (L3-ED: first and last wires are relocated to optimize emittance resolution).

No new magnets are needed in the L3-linac, except those used for matching surrounding the BC2 chicane. One new low current (25 A) bulk quadrupole power supply is installed in each of sectors 25 through 29 in order to achieve rms regulation tolerances of <0.5% (not easily achieved with the existing 200-Ampere bulk supply per sector). In addition, the existing 20-Ampere booster power supplies (one per quadrupole) will be used to adjust the focusing within a sector.

7.4 Electron Bunch Compressors

7.4.1 First Bunch Compressor

The first compression-stage, BC1, is a magnetic chicane designed to introduce the energy dependence of a particle's path length ($\Delta z = R_{56}\delta E/E_0$) needed to compress a 830 μm bunch to 200 μm. Several designs are possible, but the simplicity of a four-dipole magnetic chicane is attractive because it: (1) adds no net beamline bend angle or offset, (2) generates no chromaticity or high order dispersion (with rectangular bends) since it contains no quadrupole magnets, and (3) allows simple tuning of the momentum compaction, R_{56}, with a single power supply.

The short bunch demands a chicane design where coherent synchrotron radiation (CSR) generated within the bends does not significantly dilute the emittance. In addition, the chicane length should be minimized so that the number of removed linac accelerating sections is small. An optimized parameter set has been chosen with a 250-MeV chicane motivated by synchrotron radiation effects and linac longitudinal beam dynamics simulations. This system and its adjacent diagnostics will replace four existing 3-meter rf sections in sector-21 (21-2a,b,c,d). A phosphor screen profile monitor, a BPM, and a horizontal beam collimator will be included at the center of the chicane.

7.4.1.1 Overview and Parameters

The chicane design is set by the need to reduce transverse emittance dilution due to coherent synchrotron radiation (CSR) in the bends, which is most pronounced for short bunches [19], [20], [21], [22], [23]. Since the dominant component of the energy spread generated by CSR is correlated along the bunch, only the projected transverse emittance is altered. The emittance of the bunch slices is typically unchanged. The effect can be minimized by using a weak chicane and a large initial correlated energy spread. A symmetric double-chicane is also possible [16] and can be used to reduce the projected emittance growth. Unfortunately, the added bending for the double-chicane increases the possibility of a CSR-induced micro-bunching instability [3]. For this reason single chicanes are used in the present design.

Table 7.11 Parameters of 1st bunch compressor chicane, BC1.

Parameter	Symbol	Unit	Value
Beam energy	E	GeV	0.250
Initial rms bunch length	σ_{z_i}	mm	0.83
Final rms bunch length	σ_{z_f}	mm	0.19
RMS total incoming relative energy spread (at 250 MeV)	σ_δ	%	1.78
RMS uncorrelated relative energy spread (at 250 MeV)	σ_{δ_u}	10^{-5}	1
Momentum compaction	R_{56}	mm	−35.9
Second order momentum compaction	T_{566}	mm	+53.9
Total chicane length (1st bend to last)	L_{total}	m	6.56
Floor length of each of four dipole magnets	L_B	m	0.20
Floor length of drift between first two and last two dipoles	ΔL	m	2.60
Floor length of drift between center two dipoles	ΔL_c	m	0.50
Bend angle of each dipole	$\lvert\theta_B\rvert$	deg	4.62
Magnetic field of each dipole	$\lvert B\rvert$	kG	3.36
Maximum dispersion in chicane center (≈ beamline excursion)	$\lvert\eta_{\max}\rvert$	m	0.229
Projected CSR emittance dilution ($\gamma\varepsilon_0$ = 1 μm)	$\Delta\varepsilon_{\text{CSR}}/\varepsilon_0$	%	5
CSR-induced relative energy spread (at 250 MeV)	$\sigma_{\delta\text{CSR}}$	%	0.029
CSR- induced relative energy loss (at 250 MeV)	δ_{CSR}	%	−0.068

Motivations and quantitative arguments for the choices of these parameters are described in the following sections. Results of longitudinal beam dynamics simulations have been used to set the final BC1 bunch length at 195 μm rms. The bunch length is adjustable using the R_{56} of BC1 and the rf phase of L1. The center two dipoles of the chicane will be placed on remotely movable

horizontal stages in order to: 1) allow non-LCLS linac operation, 2) ease dipole field quality tolerances, and 3) allow a high-resolution BPM to be placed at the center of the chicane to provide energy feedback. With the dipoles switched off, the BC1 (and also the BC2) chicane can then be straightened out. The maximum horizontal beamline excursion at chicane center is equal to the maximum dispersion, $|\eta_{max}|$, listed in the table. The excursion is toward the tunnel 'wall' (north) to keep the 'aisle' clear.

Figure 7.19 shows the dispersion and beta functions through the BC1 chicane, and **Table 7.11** lists parameters for the chicane. Magnet locations are shown at the top of the figure. This plot and other calculations are made for a net R_{56} of −35.9 mm.

7.4.1.2 Momentum Compaction

The momentum compaction (R_{56}) of a chicane made up of rectangular bend magnets is negative (for bunch head at $z < 0$). For ultra-relativistic electrons and small bend angles, the net R_{56} of the chicane is given in **Eq. (7.12)** where the symbol definitions are taken from **Table 7.11**.

$$R_{56} \equiv \frac{\partial z}{\partial \delta} \approx -2\theta_B^2 \left(\Delta L + \frac{2}{3} L_B \right) . \qquad \textbf{(7.12)}$$

Free parameters are: bend lengths, angles, and drift lengths. The required R_{56} is determined from the desired compression, the energy spread, and the rf phase of L1, which is chosen in the parameter optimization as described in **Section 7.2.2**. The second order momentum compaction (T_{566}) of a rectangular-bend chicane (no quadrupole magnets) is $T_{566} \approx -3R_{56}/2$ [24].

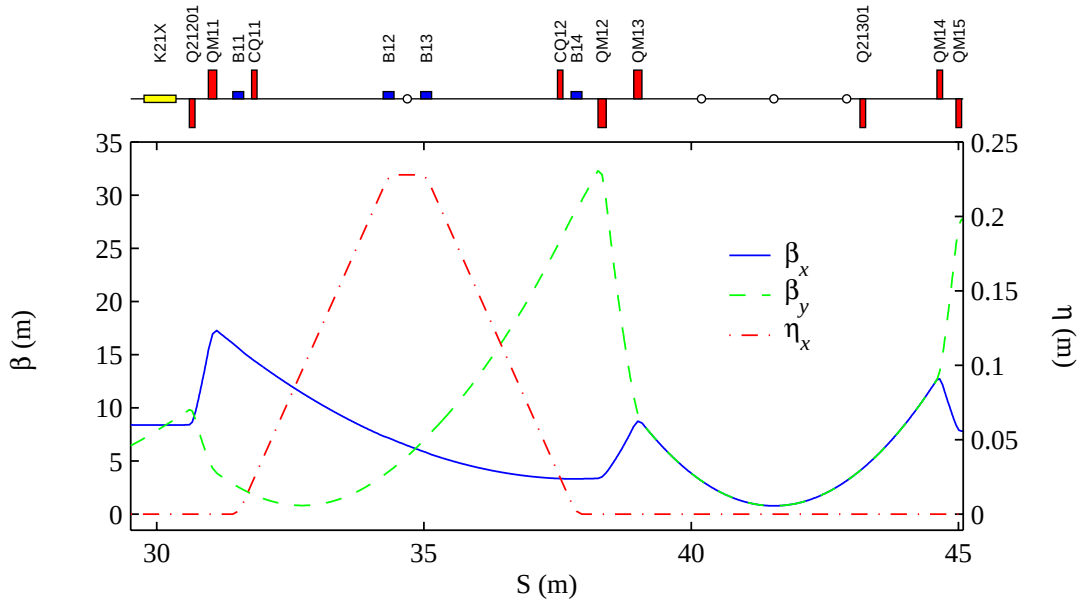

Figure 7.19 Dispersion and beta functions through BC1 chicane for $R_{56} \approx -35.9$. X-band rf structure ('K21X' in yellow) is upstream of first chicane. Energy spread profile monitor is small circle in center of 1st chicane. Two quads inside first chicane are for horizontal dispersion correction and are nominally off.

A beam delay must also be accounted for in the rf phase of the following linac (L2 in this case) as the beam path length increases through a chicane. The phase delay is described in **Eq. (7.13)**, where the rf phase lag is $\Delta\varphi$. The L2 rf phase needs to be delayed with respect to the chicane-off phase by $d\Delta\varphi/dR_{56} \approx \pi/\lambda \approx 1.72°$/mm (or 61.5° S-band with the nominal R_{56} of −35.9 mm):

$$\Delta\varphi = \frac{2\pi\Delta s}{\lambda} = \frac{4\pi}{\lambda}\left[2L_B\left(1-\frac{\theta_B}{\sin\theta_B}\right)+\Delta L\left(1-\frac{1}{\cos\theta_B}\right)\right] \approx \frac{\pi R_{56}}{\lambda} \ . \qquad \textbf{(7.13)}$$

7.4.1.3 Coherent Synchrotron Radiation (CSR)

Introduction

For very short bunches, the coherent component of synchrotron radiation can be significant and may dilute the horizontal emittance by generating energy spread in the dipoles. In this case, however, the energy spread is mostly correlated along the bunch and is not a random effect. For an rms bunch length, σ_z, dipole length, L_B, bend radius, R ($\approx L_B/\theta_B$), and N electrons per bunch, the CSR-induced rms relative energy spread per dipole for a gaussian bunch under steady-state conditions is [20]

$$\sigma_\delta \approx 0.22\frac{Nr_eL_B}{\gamma R^{2/3}\sigma_z^{4/3}} \ , \qquad \textbf{(7.14)}$$

where r_e is the classical electron radius and γ is the Lorentz energy factor. This is valid for a dipole magnet where radiation shielding (see **Figure 7.20**) of a conducting vacuum chamber is not significant; i.e., for a full vertical vacuum chamber height h which satisfies [25]

$$h >> \left(\pi\sigma_z\sqrt{R}\right)^{2/3} \equiv h_c \ . \qquad \textbf{(7.15)}$$

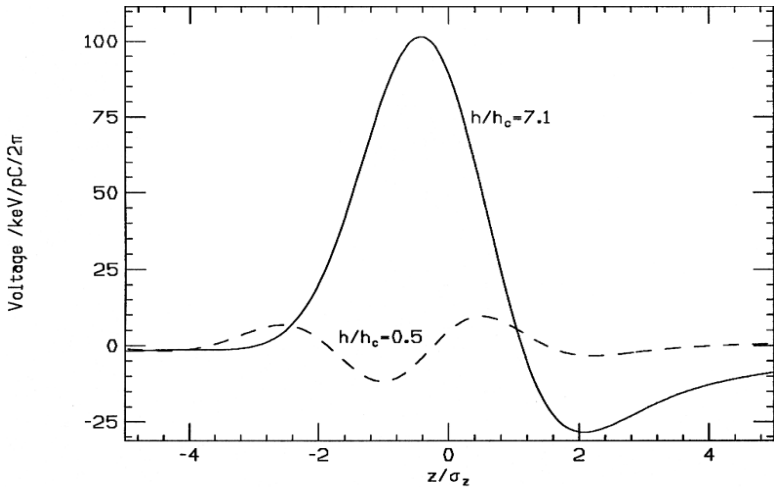

Figure 7.20 Coherent radiation steady-state wake per 2π bend (R = 19.4 m, σ_z = 30 μm, h_c = 5.6 mm) for both shielded (dash: h/h_c = 0.5) and unshielded (solid: $h/h_c >> 1$) coherent radiation of a gaussian bunch. Here the bunch head is at $z > 0$ and $V > 0$ represents energy loss.

Typically, the value of h required to adequately shield the CSR effects is too small to allow an adequate beam aperture (in this case, for $R \approx 2.5$ m, $h << 10$ mm will shield a 190-μm bunch). The shielding will not, however, suppress coherent radiation stemming from current spikes with characteristic length << σ_z. In addition, with very small apertures, geometric or resistive wakefields can also generate emittance dilution. For these reasons it is not planned to incorporate radiation shielding into the chamber design.

In non-steady-state conditions, as the bunch enters the magnet, the CSR fields go through a transient regime as the radiation from the tail of the bunch catches up with the head. The characteristic length required for this transient region is L_0, given by [20]

$$L_0 \equiv \left(24\sigma_z R^2\right)^{1/3} . \qquad \textbf{(7.16)}$$

After the length L_0, and for a gaussian bunch, the fields begin to take on the steady-state form as given in **Eq. (7.14)**. The radiation generated within the bend can also catch-up to the bunch after it exits the bends. This bend-exit transient can be a very important contribution to the emittance growth and must also be included in the calculations.

Since the bunch length shortens through the chicane, the local energy spread induced at each dipole increases, with the final dipole generating the most significant energy spread (the bunch length is virtually constant in the first and last dipoles). The rms horizontal emittance after a single chicane can be written as

$$\Delta x = \int_{\text{bends}} R_{16}(s)\frac{d\delta}{ds}ds \ , \qquad \Delta x' = \int_{\text{bends}} R_{26}(s)\frac{d\delta}{ds}ds \ ,$$

$$\varepsilon^2 = \varepsilon_0^2 + \varepsilon_0\left[\beta\langle\Delta x'^2\rangle + 2\alpha\langle\Delta x\Delta x'\rangle + \left(1+\alpha^2\right)\langle\Delta x^2\rangle/\beta\right] + \langle\Delta x^2\rangle\langle\Delta x'^2\rangle - \langle\Delta x\Delta x'\rangle^2 \qquad \textbf{(7.17)}$$

$$= \varepsilon_0^2 + 2\zeta\varepsilon_0\Delta\varepsilon + \Delta\varepsilon^2 \geq \left(\varepsilon_0 + \Delta\varepsilon\right)^2 , \qquad \zeta \geq 1.$$

Here $R_{16}(s)$ and $R_{26}(s)$ are the standard transfer matrix elements from point s to end of the chicane, β and α are the nominal Twiss parameters at end of the chicane, and ε_0 and ε are the initial and final rms horizontal emittances. The change in centroid coordinates, Δx and $\Delta x'$, pertain to a single longitudinal bunch 'slice'. Their second moments (e.g., $\langle\Delta x^2\rangle$) are ensemble averages over the entire bunch, and ζ is the Courant-Snyder invariant [see **Eq. (7.26)**]. In ideal unshielded, steady-state conditions, where $\langle\Delta x^2\rangle\langle\Delta x'^2\rangle \approx \langle\Delta x\Delta x'\rangle^2$, the relative emittance growth for just the last bend of a single chicane, using **Eq. (7.14)** and **Eq. (7.17),** and a constant gaussian bunch length, σ_z, in that last bend magnet is

$$\frac{\varepsilon}{\varepsilon_0} \approx \sqrt{1 + \frac{(0.22)^2}{36}\frac{r_e^2 N^2}{\gamma\varepsilon_N\beta}\left(\frac{|\theta|^5 L_B}{\sigma_z^4}\right)^{2/3}\left[L_B^2\left(1+\alpha^2\right) + 9\beta^2 + 6\alpha\beta L_B\right]} , \qquad \textbf{(7.18)}$$

with ε_N ($\equiv \gamma\varepsilon_0$) introduced to represent the initial normalized (invariant) emittance. This is typically an underestimate of the growth, since it does not include radiation effects in the rest of

the chicane, which can be significant. It also shows the importance of matching β and α to the phase space distortion effects of the radiation.

Calculations of the CSR-induced emittance dilution have been made using the *TraFiC4* code [22] written at DESY and also using *Elegant* [10] (see below, "CSR Calculations with a Transient Model"), which result in a projected emittance growth of ~5%. The slice emittance is, however, almost unchanged (<<1% increase). Calculations using *TraFiC4* were, however, based on an older chicane design and a gaussian beam [16], [26].

The R_{56} of the BC1 chicane is also intended to be adjustable to allow for correction of the longitudinal phase space of the linac output beam and to provide control of the final bunch length. An R_{56} tuning range of 0 to −65 mm will allow a wide flexibility in the LCLS accelerator to provide for different machine configurations at variable bunch charge, etc.

CSR Calculations with a Transient Model

More complete calculations of the CSR effects on the bunch through BC1 have been made using *TraFiC4*, and also using *Elegant*. Both codes are time domain treatments that include field transients at entrance and exit of the bends. *TraFiC4* is a 3D full-field treatment including *x-z* correlations in the beam at high dispersion points, the space charge forces, and longitudinal as well as transverse forces. The bunch distribution used is, however, typically gaussian, although other possibilities exist. *Elegant* is a 1D line-charge model, which ignores the transverse extent of the beam when calculating the CSR wakefield. This limitation can generate an overestimate of the projected emittance growth, but it is not considered to be a large effect for the LCLS compressor chicanes. *Elegant* also only calculates the longitudinal CSR forces.

In *Elegant*, it is easily possible to use the actual temporal profile of the bunch, tracked from the injector, and to calculate the CSR-generated longitudinal 'wakefields' of this non-gaussian line-charge [27]. The bunch is binned into 500 slices and the CSR-wakefield is calculated using the results of reference [21], which predict the rate of energy change of a particle at point z in the bunch:

$$\frac{dE(z,\phi)}{d(ct)} = -\frac{2r_e mc^2}{3^{1/3}R^{2/3}}\left\{\left(\frac{24}{R\phi^3}\right)^{1/3}\left[\lambda\left(z - R\phi^3/24\right) - \lambda\left(z - R\phi^3/6\right)\right] + \int_{z-R\phi^3/24}^{z}\frac{dz'}{(z-z')^{1/3}}\frac{d\lambda(z')}{dz'}\right\}. \tag{7.19}$$

The bend radius is R, the bend angle is ϕ, the line-charge density distribution is $\lambda(z)$, r_e is the classical electron radius, mc^2 is the rest energy of the electron, and $\lambda(z - R\phi^3/...)$ implies evaluation of λ at $(z - R\phi^3/\ldots)$. This relation can be used to calculate the distribution of the rate of the energy change of the electrons as a function of bend angle ϕ when the bunch enters the bend magnet. The magnets are sliced 10-20 times and **Eq. (7.19)** is evaluated for each slice, allowing for a changing $\lambda(z)$, as shown in the plots of **Figure 7.7**. The energy change continues between

magnets, where radiation in the previous bends can still alter the bunch. This is modeled in *Elegant* by using the bend-exit model outlined in [28].

Figure 7.21 shows the 'real' temporal distribution of the LCLS electron bunch in BC1, as it compresses, and the CSR-wakefield, from **Eq. (7.19)**, within the third bend of chicane-1, using the temporal distribution taken from tracking upstream of BC1. The variable color traces represent the two functions sampled in each of ten points along the bend magnet.

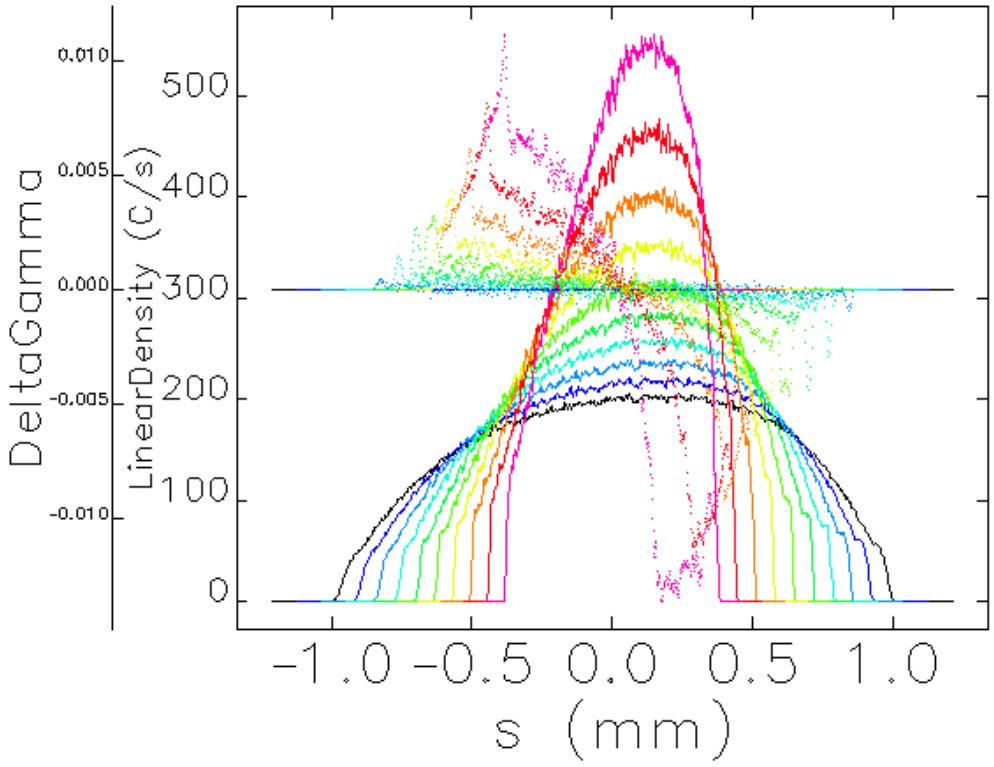

Figure 7.21 Temporal distribution of bunch (solid: "LinearDensity") and CSR-wakefield (dots: "DeltaGamma") within third bend of chicane in BC1. The variable color traces represent the two functions sampled in each of ten points along the bend magnet.

Figure 7.22 shows the position spread in the electron beam, x, without CSR (left) and with CSR (right), versus the axial bunch coordinate, z, plus their distribution projections, at the end of the BC1-chicane, using 2×10^5 tracked particles (similar plot for x'-angle vs. z is not shown). The temporal profile used for $\lambda(z)$ is the 'real' expected temporal distribution with its non-linear energy correlations, shown in the 3rd row of **Figure 7.6** and partially above in **Figure 7.21**, which are based on 6D tracking through the accelerator up to the entrance of the BC1 chicane. The initial bunch length is 830 μm rms, the final bunch length is 195 μm rms, the initial emittance is 1.0 μm, the charge is 1 nC, and the horizontal beta and alpha functions at first bend entrance are $\beta_x \approx 16.7$ m and $\alpha_x \approx 2.0$ (see **Figure 7.19**).

The final emittance is increased by 5% (including all particles), while the slice emittance is unchanged. If the linear energy correlation is removed from the spatial, x, and angular, x',

coordinates (i.e., by slightly altering the residual dispersion after the chicane using the small 'tweaker' quadrupole magnets included in the chicane—see CQ11 and CQ12 labels in **Figure 7.19**), the projected emittance growth is reduced to 1%. This tweaker-quad correction has been successfully tested in simulations, but unfortunately couples energy jitter into horizontal position jitter. For this reason the tweaker-quads will probably only be used to correct dispersion errors.

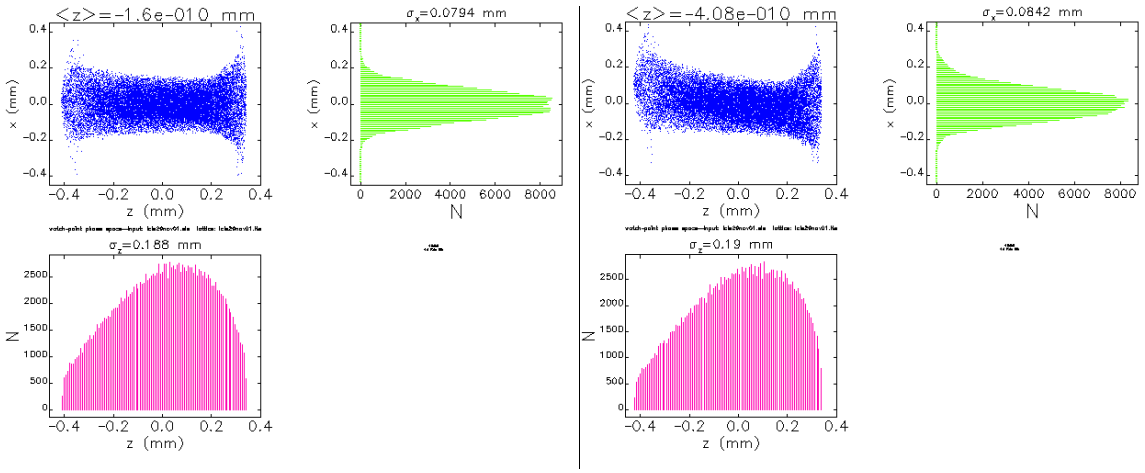

Figure 7.22 Horizontal position, *x*, without CSR (left) and with CSR (right), versus *z*, for LCLS bunch profile (i.e., tracked through upstream systems) after BC1. The projected emittance growth is 5%.

The total energy loss due to CSR is 0.17 MeV (or 0.068%). The change in central trajectory produced by the energy loss in the bends has been corrected in the tracking by steering so that the electron beam does not pass off-center through quadrupoles. The mismatch effect on the horizontal beta and alpha functions at the end of the chicane is negligible.

7.4.1.4 Beam Size, Aperture, and Field Quality

From the parameters in **Table 7.11** (η_{max} and σ_δ), the horizontal rms beam size in the center of the BC1 chicane is 4.1 mm. A reasonable R_{56} tuning range for BC1, allowing a wide range of flexibility, is 0 to −65 mm. The displacement of the center two dipoles is remotely controlled while varying the fields, and hence R_{56}. This also allows the chicane to be straightened out for non-LCLS operations (dipoles off).

Field quality tolerances for the four dipoles are listed in **Table 7.12**. Quadrupole field components (b_1/b_0) are correctable, while sextupole (b_2/b_0) and decapole (b_4/b_0) components, without specialized correction magnets, are not. Magnet roll errors generate anomalous vertical dispersion, which should be correctable with vertical steering. Field quality tolerances on the center pair of dipoles are tight but achievable, especially in consideration of the empirical corrections built into the system (i.e., the tweaker quads).

A pair of adjustable collimator jaws will be included in the center of the chicane, just upstream of a profile monitor, which can be used to cut the horizontal (i.e., energy) tails. The collimator will be nominally open with a full horizontal gap of ~8 cm, but each jaw will be

independently controlled in order to select any energy band. The collimator will be very useful in diagnosing tails in the electron beam. It is not envisioned that any significant collimation will be made during normal LCLS operations. Otherwise this may introduce an intolerably large pulse-to-pulse charge jitter downstream of BC1.

7.4.1.5 Tuning and Correction

Dispersion errors (typically horizontal) are generated by quadrupole field components in the center dipoles of BC1 (see **Table 7.12**). A pair of small correction quadrupoles are included in the chicane (see **Figure 7.19**), with the first one (CQ11) placed near the end of B11 at $\eta_x \approx 24$ mm, $\beta_x \approx 14$ m, and the second (CQ12) just upstream of B14 ($\eta_x \approx 24$ mm, $\beta_x \approx 3.3$ m). Two orthogonal linear combinations of these quadrupoles can then be used to correct emittance dilution due to dispersion errors over a large range. Since the dispersive beam size at these quadrupoles is $\eta_x \sigma_\delta \approx 430\ \mu$m, and the betatron beam size is much smaller at $(\beta_{x,y}\varepsilon_{x,y})^{1/2} < 170\ \mu$m, these quadrupoles have little effect on beta functions. Two orthogonal linear combinations of these quadrupoles can then be used to correct up to ~250% horizontal emittance dilution due to dispersion errors. The specifications for these correction quadrupoles are given in **Table 7.13** and their locations are shown in **Figure 7.19**.

The four dipoles are powered in series with one main power supply so that regulation errors have little effect (**Table 7.4**). The rms regulation tolerance for this main supply is 0.02%. Separate trim coils will also be included in each BC1 main dipole so that compensation can be made for magnet-to-magnet construction variations in the dipole field strength. In addition, vertical dipole correctors will be included nearby to allow vertical steering. The alignment and field strength sensitivities for quadrupole magnets in the BC1 area are shown in **Figure 7.23**. Each sensitivity shown corresponds individually to a summed x and y emittance dilution of $\Delta\varepsilon_x/\varepsilon_{x0} + \Delta\varepsilon_y/\varepsilon_{y0} = 2\%$. Quadrupole field errors affect beam matching and the sensitivities here assume the mismatch has completely filamented and diluted the emittance (a conservative assumption).

Table 7.12 Dipole magnet tolerances for BC1. Field harmonics are evaluated on a 20-mm radius and each entry individually corresponds to a 2% emittance dilution.

Magnet	**Quantity**	**Roll Angle** [mrad]	$\lvert b_1/b_0 \rvert$ [%]	$\lvert b_2/b_0 \rvert$ [%]	$\lvert b_4/b_0 \rvert$ [%]
B11 &B14	1 each	3.9	0.30	22.	100
B12 & B13	1 each	2.6	0.02	0.07	0.28

Table 7.13 Dispersion correction quadrupoles for BC1 chicane-1 for horizontal emittance correction of up to 250% (with $\Delta\varepsilon/\varepsilon \approx 1\%$ step size control).

Maximum Pole-Tip Field [kG]	**Quantity**	**Step Size** [kG]	**Pole Radius** [mm]	**Length** [m]
0.5	2	0.05	50	0.05

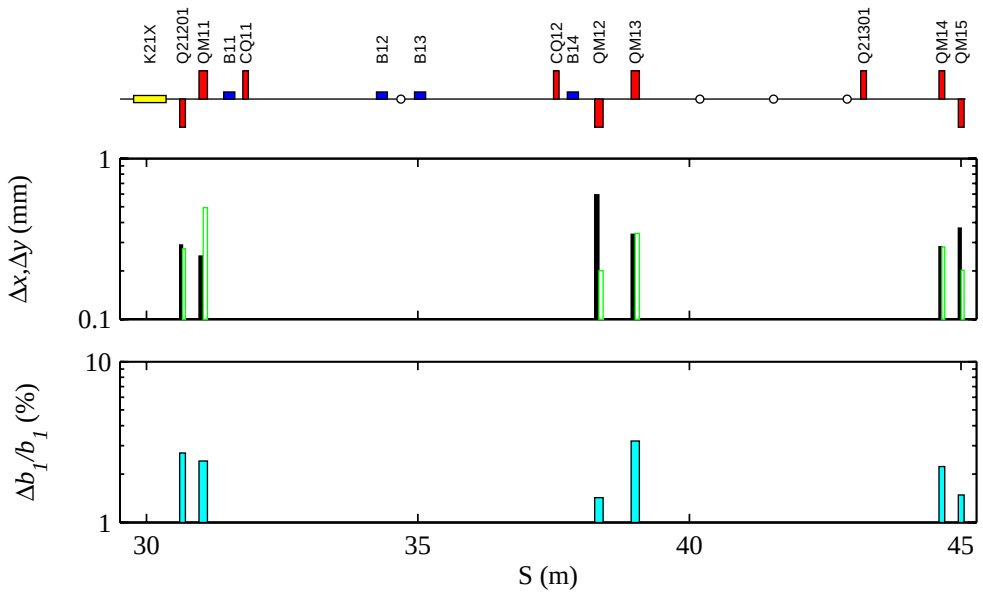

Figure 7.23 Alignment (top: black is *x*, and green/white is *y*) and gradient sensitivities (bottom) for BC1 quadrupoles. Each bar individually corresponds to a 'filamented' emittance dilution of $\Delta\varepsilon_x/\varepsilon_{x0} + \Delta\varepsilon_y/\varepsilon_{y0} = 2\%$.

An insertable tune-up dump will also be included after the BC1 emittance diagnostics (at $S \approx 44$ m of **Figure 7.19**) in order to allow invasive tuning of the BC1 and upstream systems. The dump will need to handle a 1-nC electron beam at 120 Hz and 250 MeV or 30-W of average power.

Finally, a profile monitor (phosphor screen) will be included in the center of the BC1 chicane where the dispersion is large ($\sigma_x \approx 4.1$ mm). This device will allow measurement of the correlated energy spread and therefore will also reveal the temporal distribution of the bunch as it enters the BC1 chicane. A horizontal collimator just upstream of the profile monitor will be used to diagnose beam tails, and one BPM of ≤20-μm resolution will be located in the center of the BC1 chicane. The BPM reading will provide a high-resolution relative energy measurement ($\delta \approx 0.01\%$), per beam pulse (see **Section 7.8.4**). The betatron component of the beam position will be small and also correctable by incorporating ≥2 BPMs up or downstream of the chicane.

7.4.2 Second Bunch Compressor

Like the first compressor, the second compressor, BC2, is a four-dipole magnetic chicane. It is designed to compress a ~200 μm bunch to ~20 μm. The high energy and short bunch demand a chicane design where both coherent and incoherent synchrotron radiation generated within the bends do not significantly dilute the horizontal or longitudinal emittance. In addition, the chicane length is minimized so that the number of removed linac accelerating sections is not too large. An optimized parameter set has been chosen with a 4.54-GeV chicane motivated by synchrotron radiation effects and linac longitudinal beam dynamics simulations. This system will replace the eight existing 3-meter rf sections at the end of sector-24 (24-7a,b,c,d and 24-8a,b,c,d). A

phosphor screen profile monitor, a BPM, and a horizontal beam collimator will be included at the chicane center.

In addition, a short one-period, superconducting wiggler will be located just upstream of the BC2 chicane. This wiggler is used to increase the intrinsic (uncorrelated) energy spread of the beam in order to damp CSR micro-bunching effects in the BC2 chicane [3]. The relative energy spread due to incoherent synchrotron radiation (ISR), $\sigma_{\delta_{ISR}}$, per bend magnet is given by

$$\sigma_{\delta_{ISR}} \approx \frac{1}{L_B}\sqrt{\left(4.13\times10^{-11}\ \mathrm{m}^2\cdot\mathrm{GeV}^{-5}\right)E^5\left|\theta_B^3\right|}, \qquad \textbf{(7.20)}$$

where L_B is the magnet length, θ_B is the bend angle, and E is the beam energy (4.54 GeV in the wiggler). If we use two 7-cm long coils sandwiching two 10-cm long coils, with the field profile shown in **Figure 7.24**, then a 6-Tesla peak field increases the incoherent energy spread to 3×10^{-5} (rather than 3×10^{-6} without wiggler). This is enough to reduce the CSR-induced micro-bunching effect to tolerable levels (see below). The wiggler is then ~60 cm in physical length and composed of superconducting magnets with a local liquid He cryogenics supply in or near sector-24. This scenario has been used in the past to supply the superconducting spin-rotator solenoids presently installed in the SLAC linac at north damping ring entrance and exit.

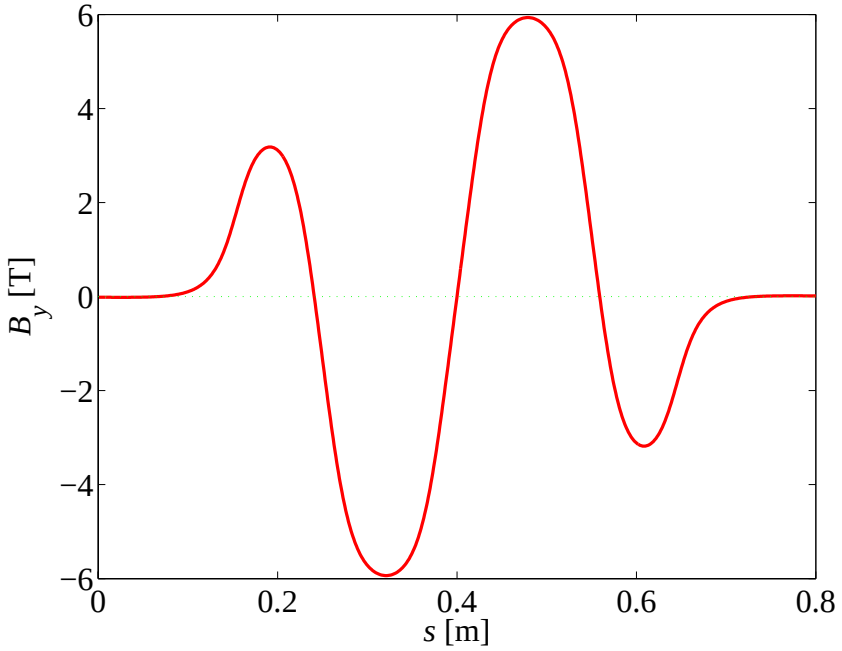

Figure 7.24 Magnetic field profile of one-period superconducting wiggler placed just upstream of BC2 chicane to increase incoherent energy spread to 3×10^{-5} rms at 4.54 GeV, which damps CSR micro-bunching.

The wiggler has almost no effect on bunch length, and CSR effects are small since the bunch length is ~200 μm long throughout the wiggler. The 'slice' horizontal emittance is, however, increased by the spontaneous radiation in the wiggler, where the dispersion is not zero. The beta

function through this wiggler is held to <75 m, which generates a 4% 'slice' emittance growth. This can be further reduced if the beta function is made even smaller, and has not yet been fully optimized.

Figure 7.25 shows the final longitudinal phase space at the undulator entrance (14.35 GeV) both *with* (top) and *without* (bottom) the wiggler switched on. Without the wiggler, the very small incoherent energy spread in BC2 (3×10^{-6} rms at 4.54 GeV) and the effects of CSR cause a severe micro-bunching instability within BC2. Switching on the wiggler increases the incoherent energy spread in BC2 to 3×10^{-5} rms, suppressing the instability. After acceleration to 14.3 GeV and compression by a factor of ~9, this larger incoherent energy spread is only 8×10^{-5} in the undulator, which is well below the safe level of 1×10^{-4}. The wiggler can also be switched off or adjusted to as much as ~7.5 T maximum peak field. This effect is presently under intense study as it may effect many bunch compressor applications.

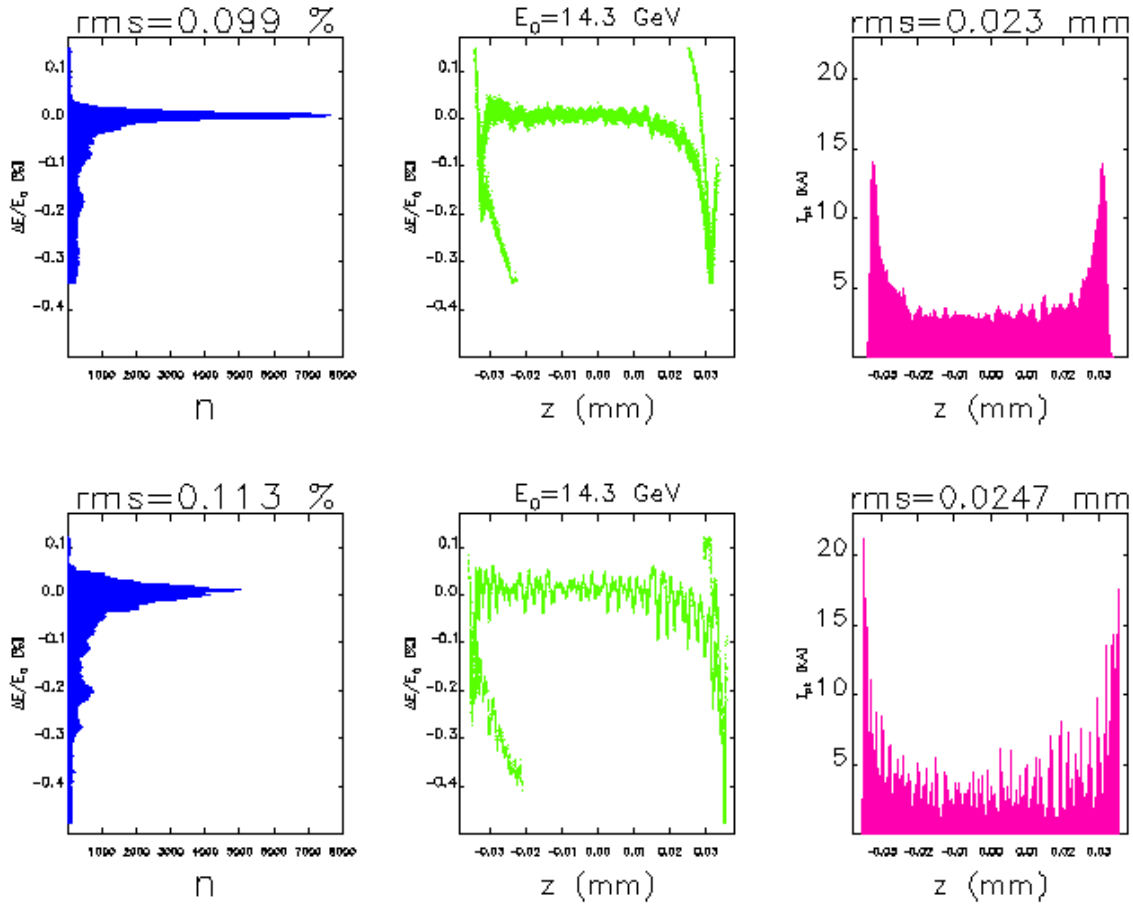

Figure 7.25 Final longitudinal phase space at undulator entrance (14.35 GeV) both *with* (top) and *without* (bottom) superconducting pre-BC2 wiggler switched on.

7.4.2.1 Overview and Parameters

Motivations and quantitative arguments for the choices of these parameters are described in the following sections. Results of longitudinal beam dynamics simulations have been used to set

the incoming BC2 bunch length at 195 μm rms. The bunch length after BC2 is adjustable using the R_{56} of BC2 and the rf phase of L2. The parameters of the BC2 chicane are listed in **Table 7.14**.

Table 7.14 Parameters of 2nd bunch compressor chicane, BC2.

Parameter	Symbol	Unit	Value
Beam energy	E	GeV	4.54
Initial rms bunch length	σ_{zi}	μm	195
Final rms bunch length	σ_{zf}	μm	22
RMS incoming relative energy spread (at 4.54 GeV)	σ_δ	%	0.76
RMS uncorrelated relative energy spread (at 4.54 GeV, with wiggler)	σ_{δ_u}	10^{-5}	3
Net momentum compaction	R_{56}	mm	−22.5
Net second order momentum compaction	T_{566}	mm	+33.8
Total system length (1st bend to last)	L_{total}	m	22.1
Floor length of each of four dipole magnets	L_B	m	0.400
Floor length of drift between first two and last two dipoles	ΔL	m	10
Floor length of drift between center two dipoles	ΔL_c	m	0.50
Bend angle for each of four dipoles	$\lvert\theta_B\rvert$	deg	1.878
Magnetic field for each of four dipoles	$\lvert B\rvert$	kG	12.41
Maximum dispersion in chicane center (≈ beamline excursion)	$\lvert\eta_{\max}\rvert$	m	0.341
Slice emittance dilution due to ISR of chicane only (at $\gamma\varepsilon_0$ = 1 μm)	$\Delta\varepsilon_{\text{ISR}}/\varepsilon_0$	%	0.3
Projected emittance dilution due to CSR (includes all particles)	$\varepsilon_x/\varepsilon_{x0}$	—	2.5
rms ISR relative energy spread of chicane only (at 4.54 GeV)	$\sigma_{\delta\text{ISR}}$	10^{-6}	8.4
rms CSR relative energy spread (at 4.54 GeV)	$\sigma_{\delta\text{CSR}}$	%	0.053
CSR relative energy loss (at 4.54 GeV)	$\langle\delta_{\text{CSR}}\rangle$	%	0.071

A nominal rms final bunch length of 22 μm is used throughout the following descriptions (unless otherwise noted). As in the case of BC1, the center two dipoles will be placed on remotely movable horizontal stages in order to: 1) allow non-LCLS linac operation, 2) to ease dipole field quality tolerances, and 3) to allow a high-resolution BPM to be placed at the center of the chicane. With the dipoles switched off, the BC2 (and the BC1) chicane can then be straightened out. The maximum horizontal beamline excursion at chicane center is equal to the maximum dispersion, $|\eta_{\max}|$, listed in the table. The excursion is toward the tunnel 'wall' (north) to keep the 'aisle' clear. **Figure 7.26** shows the dispersion and beta functions through the BC2 chicane. Magnet locations are shown at the top of the figure. This plot, and other calculations, is made for a net R_{56} of −22.5 mm.

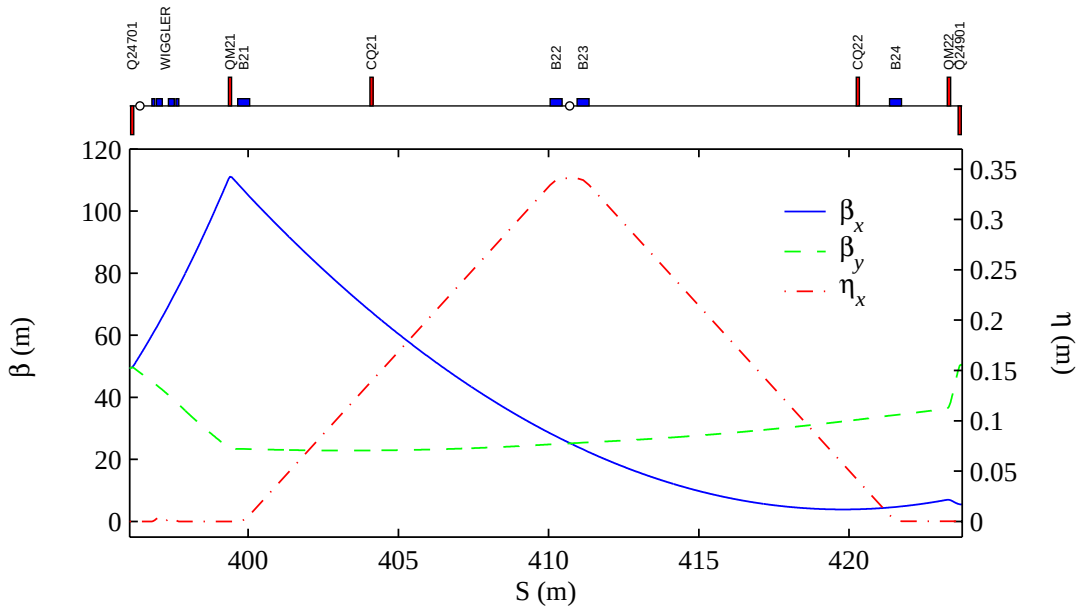

Figure 7.26 Dispersion and beta functions through BC2 chicane for $R_{56} \approx -22.5$ mm. The energy spread profile monitor is indicated by a small circle at the center of the chicane in schematic at top. The two quadrupoles inside the chicane are for dispersion correction and are nominally switched off. The superconducting wiggler is located at $S \approx 397$ m.

7.4.2.2 Momentum Compaction

The momentum compaction (R_{56}) for a chicane is given by **Eq. (7.12)**. The second order momentum compaction is $T_{566} \approx -3R_{56}/2$ (as in BC1). A beam delay as described in **Eq. (7.13)** is also necessary for the L3 rf phase. The L3 rf phase needs to be delayed, with respect to the chicane-off phase, by $d\varphi/dR_{56} \approx \pi/\lambda \approx 1.72°$/mm (or 38.7° with the nominal BC2 R_{56} value of −22.5 mm).

7.4.2.3 Incoherent Synchrotron Radiation (ISR)

Horizontal emittance dilution will occur if significant energy spread is generated anywhere within the chicane (or the wiggler). Synchrotron radiation within the dipoles generates energy spread, which breaks the linear achromaticity of the chicane and therefore dilutes the horizontal emittance. Using a typical symmetric beta function through a single chicane with its maximum, $\beta_{\max}$, at start and end of the chicane and its minimum, $\beta_{\min}$, in the middle, and using symbols defined in **Table 7.14**, then

$$\beta_{\max} = 2\beta_{\min} = 4L_B + 2\Delta L + \Delta L_c \,. \qquad \textbf{(7.21)}$$

The additive ISR emittance dilution [29] can then be approximated, for $\Delta\varepsilon/\varepsilon_0 << 1$, by

$$\Delta\gamma\varepsilon_{\mathrm{ISR}} \approx (8\times10^{-8}\ \mathrm{m}^2\cdot\mathrm{GeV}^{-6})\cdot E^6\left(|\theta_{B1}|^5 + |\theta_{B2}|^5\right)\frac{4\Delta L + 6L_B + \Delta L_c}{2L_B^2}\,. \qquad \textbf{(7.22)}$$

The parameters of **Table 7.14** are chosen such that the relative ISR emittance growth is 0.3% ('slice' emittance growth). This incoherent energy spread is generated through a random process and therefore cannot be corrected. Unlike most other dilution effects in the LCLS accelerator, here the 'slice' emittance is increased, and so the growth is held to a very small level. The energy in BC1 is too low for this effect to be important.

7.4.2.4 Coherent Synchrotron Radiation (CSR)

Introduction

The effects of CSR have been described in **Section 7.4.1** pertaining to the BC1 design. The BC2 compression-stage is also a 4-dipole chicane and the bunch is linearly compressed from 195 μm to 22 μm. Calculations of the CSR-induced emittance dilution have been made using the DESY *TraFiC4* code [22] and *Elegant* [10] (see below, "CSR Calculations with a Transient Model"). The slice emittance is, however, almost unchanged.

Shielding is, however, not practical for BC2 since a full vacuum chamber height of <3 mm would be required to significantly shield the shortest bunch. This presents an aperture restriction and may also generate geometric and/or resistive wakefields comparable to the CSR effects being shielded.

The R_{56} of the BC2 chicane is also intended to be adjustable to allow for correction of the longitudinal phase space of the linac output beam and to provide control of the final bunch length. An R_{56} tuning range of 0 to −50 mm will allow a wide flexibility in the LCLS accelerator to provide for very different machine configurations at variable charge, etc.

CSR Calculations with a Transient Model

More complete calculations of the CSR effects on the bunch through BC2 have been made using *TraFiC4* and also using *Elegant*. The details of the *Elegant* calculation are described in **Section 7.4.1**. **Figure 7.27** shows the additional rms energy spread induced by CSR (top) and the normalized horizontal emittance (bottom) along the DL2 bend system (1st bend to 5 meters after 4th bend). The total accumulated CSR-wakefield energy gradient along the bunch generated within the BC2 chicane is plotted in **Figure 7.28**.

More detail is shown in **Figure 7.29** which plots the temporal distribution of the bunch as it compresses and the evolving CSR-wakefield, from **Eq. (7.19)**, within the third bend of the chicane using the temporal distribution taken from tracking upstream of BC2. The variable color traces represent the two functions sampled in each of twenty points along the bend magnet.

Figure 7.30 shows the angular spread in the electron beam, x', without CSR (left) and with CSR (right), versus the axial bunch coordinate, z, plus their distributions at the end of the BC2-chicane using 2×10^5 tracked particles. The temporal distribution used here is the 'real' expected temporal distribution with non-linear correlations shown in the last row of **Figure 7.6**, which is based on 6D tracking through the entire LCLS up to the entrance of BC2 including the SC-wiggler. The initial bunch length is 195 μm rms, the final bunch length is 22 μm rms, the charge

is 1 nC, and the horizontal beta and alpha functions at first bend entrance are $\beta_x \approx 105$ m and $\alpha_x \approx 5.0$ (see **Figure 7.26**).

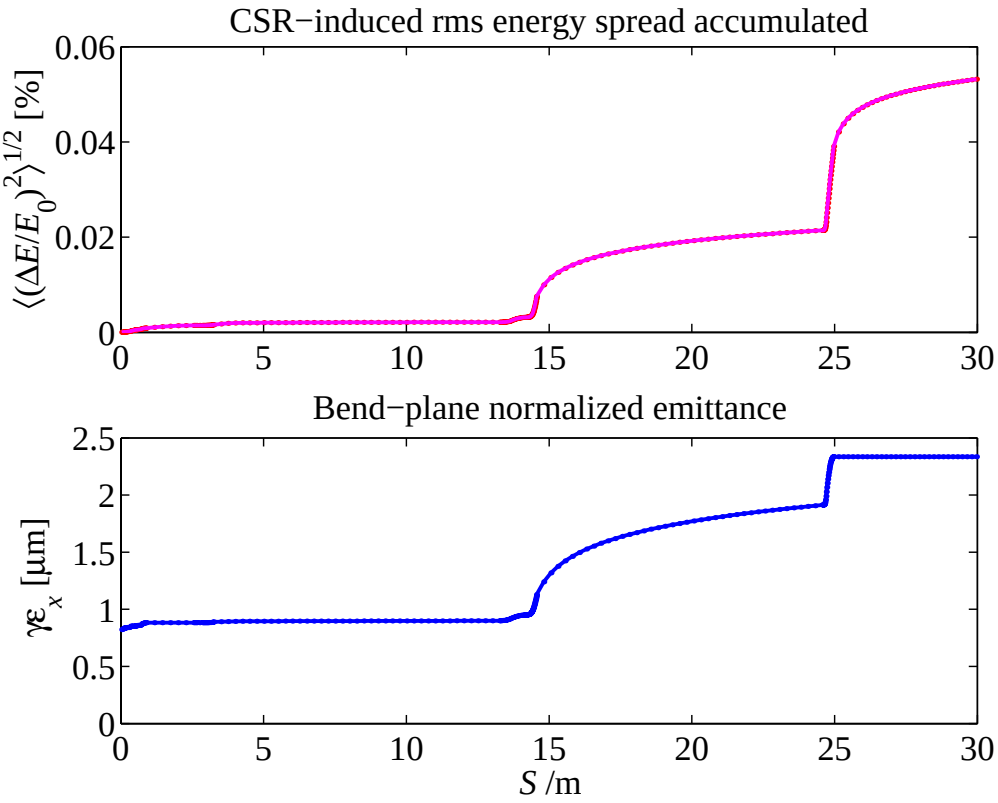

Figure 7.27 Additional rms energy spread induced by CSR (top) and the normalized horizontal emittance (bottom) along the BC2 chicane (1st bend to 5 meters after 4th bend).

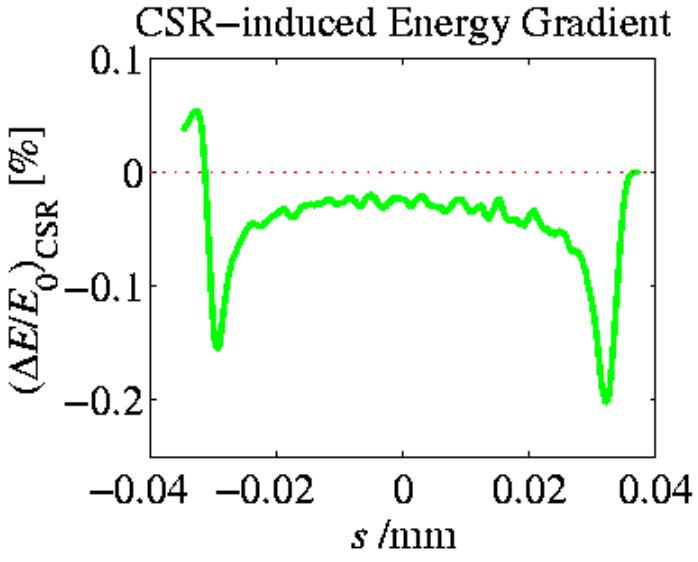

Figure 7.28 CSR-wakefield energy gradient along the bunch generated within the BC2 chicane.

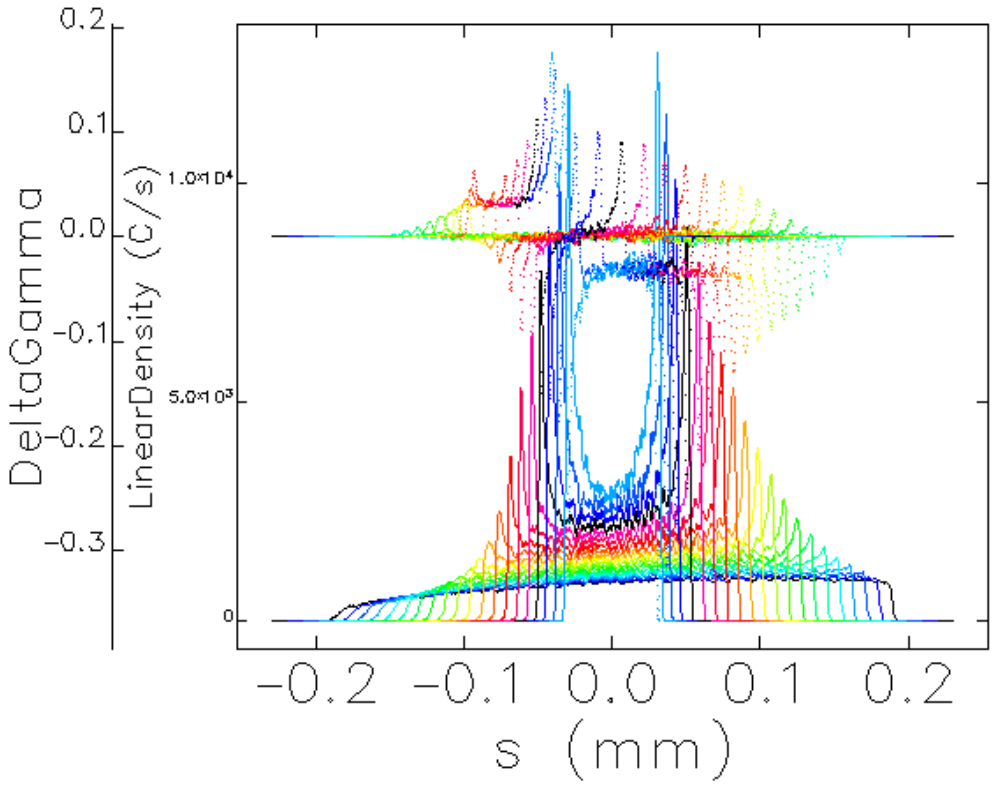

Figure 7.29 Temporal distribution of bunch (solid: "LinearDensity") and CSR-wakefield (dots: "DeltaGamma") within third bend of chicane in BC2. The variable color traces represent the two functions sampled in each of ten points along the bend magnet.

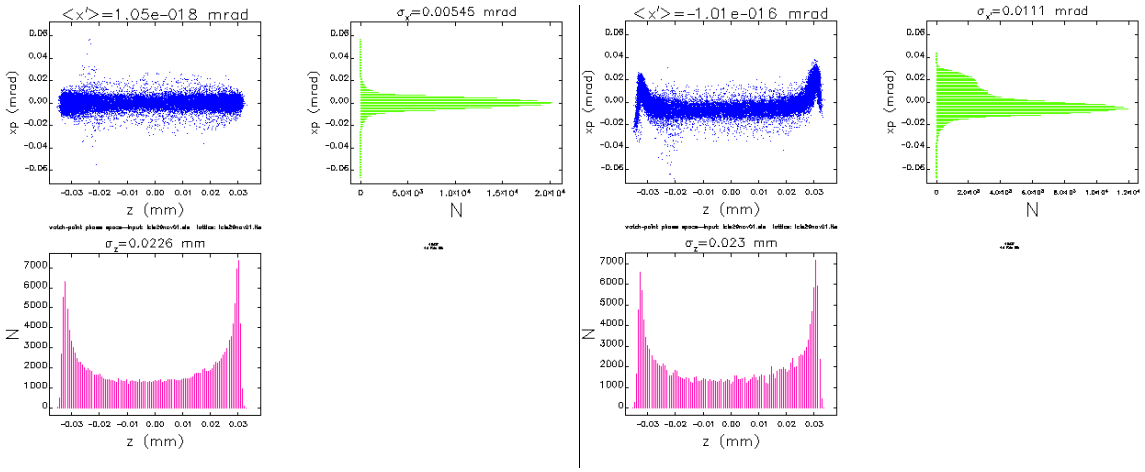

Figure 7.30 Horizontal angle, *x*′, without CSR (left) and with CSR (right), versus *z*, for LCLS bunch profile (i.e., tracked through upstream systems) after BC2. The projected emittance growth is 2.5-times larger (mostly is dominated by effects at bunch head and tail). The slice emittance is almost unchanged.

The final projected emittance is increased by a factor of 2.5, but the slice emittance is nearly unchanged (except for the 7% SC-wiggler effect). The large CSR increase is based on a 1D CSR

model, which has been seen to somewhat overestimate the effect as compared to the 3D model. In addition, the projected emittance growth is due to slice transverse offsets, which dominantly occur at the extreme head and tail of the bunch due to the very high current spikes at these locations. The projected emittance growth calculated by integrating over only the central core of the beam with 75% of the particles is actually only 60%, and this is also only the projected emittance, not the slice.

The total energy loss due to CSR is –3.2 MeV (or –0.071%). The change in central trajectory produced by the energy loss in the bends has been corrected in the tracking by steering so that the electron beam does not pass off-center through quadrupoles. The mismatch effect on the horizontal beta and alpha functions at the end of the chicane is significant ([i.e., $\zeta \approx 1.23$; see Eq. **(7.26)**]), but this is not a mismatch of the individual slices. It is a mismatch of the projected phase space, which should have a limited effect on the SASE FEL gain.

Finally, it is also possible to generate 'slice' emittance growth with the effects of CSR. The slice growth is generated when the longitudinal CSR wakefield has a significant transverse gradient over the width of the bunch [30]. These effects have been studied using *TraFiC4* with a previous, stronger design for BC2, with $R_{56} \approx -30$ mm. The slice emittance growth seen in these calculations was too small to resolve numerically (i.e., <1%).

Transverse CSR Forces

A transverse force or "centripetal force" is described in [31] which originates from radiation of trailing particles and depends on the local charge density along the bunch. The maximum force takes place at the center of the bunch and its effect on transverse emittance is estimated in the reference. This estimate predicts an emittance growth of <<1% for the worst case (last dipole of chicane-2 where bunch is shortest). In addition, calculations with a full-field model, which include the transverse forces, predict tolerable emittance growth (see below, "CSR Calculations with a Transient Model").

7.4.2.5 Resistive Wall Longitudinal Wakefields in the Bends

Longitudinal resistive wall wakefields in the BC2 vacuum chambers also induce energy spread, which may dilute the emittance. The rms relative energy spread generated in a cylindrical vacuum chamber of length L, radius a, and conductivity σ is

$$\sigma_{\delta_{\mathrm{RW}}} \approx 0.22 \frac{e^2 c N L_B}{\pi^2 a E \sigma_z^{3/2}} \sqrt{\frac{Z_0}{\sigma}} \ , \qquad \textbf{(7.23)}$$

where Z_0 ($\approx 377\ \Omega$) is the free space impedance. Note, **Eq. (7.23)** is for a long, gaussian bunch (see **Section 7.9.5**). For parameters of **Table 7.14** using 1 nC, aluminum chambers ($\sigma \approx 3.6\times10^7\ \Omega^{-1}\mathrm{m}^{-1}$), and a = 15 mm through the final bend, where the bunch length is 22 μm, the rms energy spread generated by resistive wake is $\sim 1\times10^{-6}$, which is more than an order of magnitude smaller than the CSR energy spread generated in this final bend. Stainless steel, on the other hand, will generate five times this value and should probably be avoided. The other bends

generate much less energy spread since the bunch is longer there. (The resistive-wall effects in BC1 are an order of magnitude smaller.)

7.4.2.6 Beam Size, Aperture and Field Quality

From the parameters in **Table 7.14** ($|\eta_{max}|$ and σ_δ), the horizontal rms beam size in the center of the BC2 chicane is 2.6 mm. This sets some tolerances on the field quality of the center two dipoles (per chicane) since field harmonics may generate anomalous dispersion, which can dilute the transverse emittance. Without dipole magnet movers, the horizontal displacement of the beam within the center dipoles is dependent on the R_{56} value chosen. For an R_{56} tuning range of 0 to −50 mm, the horizontal dipole aperture required for the center two bends is 52 cm. This is a large aperture dipole with tight field quality tolerances over most of the aperture. To relax this tolerance, and to allow the placement of a high resolution BPM in a small aperture in the center of the chicane, the center two dipoles are mounted on remotely movable stages to physically move the magnets as the bend angles are varied (precise synchronous control is *not* required). This locks the horizontal beam position with respect to the dipole aperture so that good field quality is only needed over an aperture of 3 cm ($12\sigma_x$), rather than 52 cm. It also allows the chicane to be straightened out for non-LCLS operation (dipoles off). This same retractable chicane design has been built and tested at the LEUTL facility at Argonne National Laboratory [32].

In addition, small correction quadrupoles are included in the chicane (CQ21 and CQ22 in **Figure 7.26**) to provide linear horizontal dispersion correction to compensate for errors. Field quality tolerances for the four dipoles are listed in **Table 7.15**. The tolerances on the two center pairs of dipoles are tight but achievable, especially in consideration of the empirical corrections built into the system.

Table 7.15 Dipole magnet tolerances for BC2 chicane (without empirical correction). Field harmonics are evaluated on a 20-mm radius and each entry individually corresponds to a 2% emittance dilution.

Magnet	**Quantity**	**Roll Angle** [mrad]	$\|b_1/b_0\|$ [%]	$\|b_2/b_0\|$ [%]	$\|b_4/b_0\|$ [%]
B21 & B24	1 each	1.8	0.11	14.	100
B22 & B23	1 each	1.7	0.01	0.05	0.5

Quadrupole field components (b_1/b_0) larger than these tolerances are correctable, while sextupole (b_2/b_0) and decapole (b_4/b_0) components, without specialized correction magnets, are not. Magnet roll errors generate anomalous vertical dispersion, which may be corrected with vertical steering or the later addition of small correction skew quadrupoles if necessary. The alignment and field strength sensitivities for quadrupole magnets in the BC2 area are shown in **Figure 7.31**. Each sensitivity shown corresponds individually to a filamented x and y emittance dilution of $\Delta\varepsilon_x/\varepsilon_{x0} + \Delta\varepsilon_y/\varepsilon_{y0} = 2\%$.

A pair of adjustable collimator jaws will be included in the center of the chicane, just upstream of the profile monitor, which can be used to cut the horizontal (i.e., energy) beam tails.

The collimator will be nominally open with a full horizontal gap of ~6 cm, but each jaw will be independently controlled in order to select any energy band. The collimator will be very useful in diagnosing tails in the electron beam. It is not envisioned that any significant collimation will be made during normal LCLS operations. This might otherwise introduce an intolerably large pulse-to-pulse charge jitter or wakefields within BC2.

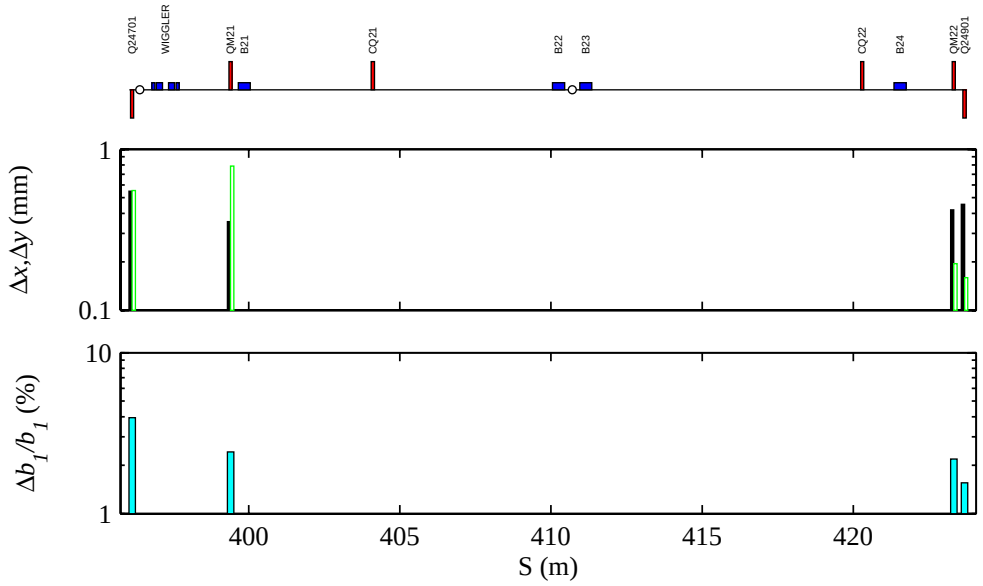

Figure 7.31 Alignment (top: black is *x*, and green/white is *y*) and gradient sensitivities (bottom) for BC2 quadrupoles. Each bar individually corresponds to a 'filamented' emittance dilution of $\Delta\varepsilon_x/\varepsilon_{x0} + \Delta\varepsilon_y/\varepsilon_{y0} = 2\%$.

7.4.2.7 Tuning and Correction

Dispersion errors (typically in the horizontal plane) may be generated by small quadrupole field components in the center two dipoles of the chicane (see **Table 7.15**). A pair of small correction quadrupoles are included in the chicane with the first quadrupole (CQ21) placed near the end of B21 at $\eta_x \approx 139$ mm, $\beta_x \approx 65$ m, and the second (CQ22) just upstream of B24 ($\eta_x \approx 41$ mm, $\beta_x \approx 4$ m). Two orthogonal linear combinations of these quadrupoles can then be used to correct up to ~250% horizontal emittance dilution due to dispersion errors. Since the dispersive beam size at these two quadrupoles is $\eta_x\sigma_\delta \approx 1$ mm and 310 μm, respectively and the betatron beam size is much smaller at $(\beta_{x,y}\varepsilon_{x,y})^{1/2} < 86$ μm, these quadrupoles have little effect on the final beta functions. The specifications for these correction quadrupoles are given in **Table 7.16** and their locations are shown in **Figure 7.26**.

The four main dipoles of the chicane will be powered in series with one power supply so that field regulation tolerances are met (see **Table 7.4**). The rms regulation tolerance for this main supply is 0.05%. Trim coils will be included in each BC2 main dipole for compensation of magnet-to-magnet construction errors in the dipole field strengths. This will also allow some horizontal steering. In addition, vertical dipole correctors will be included nearby to facilitate vertical steering.

Table 7.16 Dispersion correction quadrupoles for BC2 chicane for horizontal emittance correction of up to 250% (with $\Delta\varepsilon/\varepsilon \approx 1\%$ step size control).

Maximum Pole-Tip Field [kG]	**Quantity**	**Step Size** [kG]	**Pole Radius** [mm]	**Length** [m]
2.2	2	0.14	50	0.05

An insertable tune-up dump will also be included after BC2 in order to allow invasive tuning of the BC2 and upstream systems. The dump will need to handle a 1-nC beam at 120 Hz and 4.54 GeV, or 550 W of average power.

Finally, a phosphor screen profile monitor is included in the center of the BC2 chicane where the dispersion is large ($\sigma_x \approx 2.6$ mm). This device allows measurement of the correlated energy spread and therefore also reveals the temporal distribution of the bunch as it enters the chicane. A horizontal collimator just upstream of the profile monitor will be used to diagnose beam tails, and one BPM of ≤40-μm resolution will be located in the chicane center. The BPM reading provides a high-resolution relative energy measurement ($\delta \approx 1.2\times10^{-4}$) per beam pulse (see **Section 7.8.4**).

7.5 Beam Transport Lines

This section discusses the two beam transport lines. The first is a low-energy bend system (DL1) used to transport the electrons from the off-axis injector into the main linac. The second is the high-energy dog-leg (DL2) used for L3-to-undulator transport, as well as energy and energy spread analysis. The DL2 beamline horizontally displaces the undulator axis from that of the main linac in order to protect the undulator from potential beam halo and dark current. In addition, a short vertical bending system (VB) removes the slight (~0.3°) downward slope of the accelerator at the entrance to the undulator. This leveling-bend allows the experimental areas to be located closer to ground level.

7.5.1 Low-Energy Dog-Leg

The function of the low-energy 'dog-leg' (DL1) is to transport 150-MeV electrons from the new injector linac (L0) into the existing SLAC linac. While it is possible to design the dog-leg as a first bunch compression stage, this necessitates a large incoming correlated energy spread of 1-2%. In this case, the chromaticity of the quadrupole magnet within the dog-leg, required for a linear achromat, will generate large second order dispersion which needs sextupole compensation. Due to this, and also the need for easy R_{56} tuning (not natural in a dog-leg), DL1 is designed as a simple transport line. Its design requirements are:

- Provide a horizontal beamline deflection of 35° over a short distance,
- Should not alter the bunch length (i.e., should be nearly isochronous),
- Should introduce no significant transverse emittance dilution,
- Should provide a dispersive section for energy and energy spread measurement.

A simple system that satisfies these conditions is composed of two dipole magnets of equal strength with a field lens located between them to produce a linear achromat. The dipoles are rectangular bends. A profile monitor based on optical transition radiation (OTR) [33] and a BPM at the high dispersion point will provide energy and energy spread measurements.

The momentum compaction, R_{56}, of such a system for ultra-relativistic electrons and small angles is

$$R_{56} \approx \frac{1}{3}\theta_B^2 L_B \ , \qquad \textbf{(7.24)}$$

where θ_B and L_B are the bend angle and length of each dipole, respectively. A 1.3-meter long beamline with two 17.5° bends provides the required deflection and the 20-cm long dipoles produce an R_{56} of +6.3 mm (opposite sign of a chicane). Therefore, an extreme electron which is off energy by 1% will move axially by only 60 μm, which is small compared to the 1-mm rms bunch length. The effect of the second order momentum compaction, T_{566}, is even less. Note, the nominal incoming relative rms energy spread from L0 is actually 0.1% rms. The system is therefore, for all practical purposes, isochronous. Nevertheless, the non-zero R_{56} value and the second order term of $T_{566} \approx 0.14$ m has been taken into account throughout the design and stability optimization, and in the 2D and 6D particle tracking.

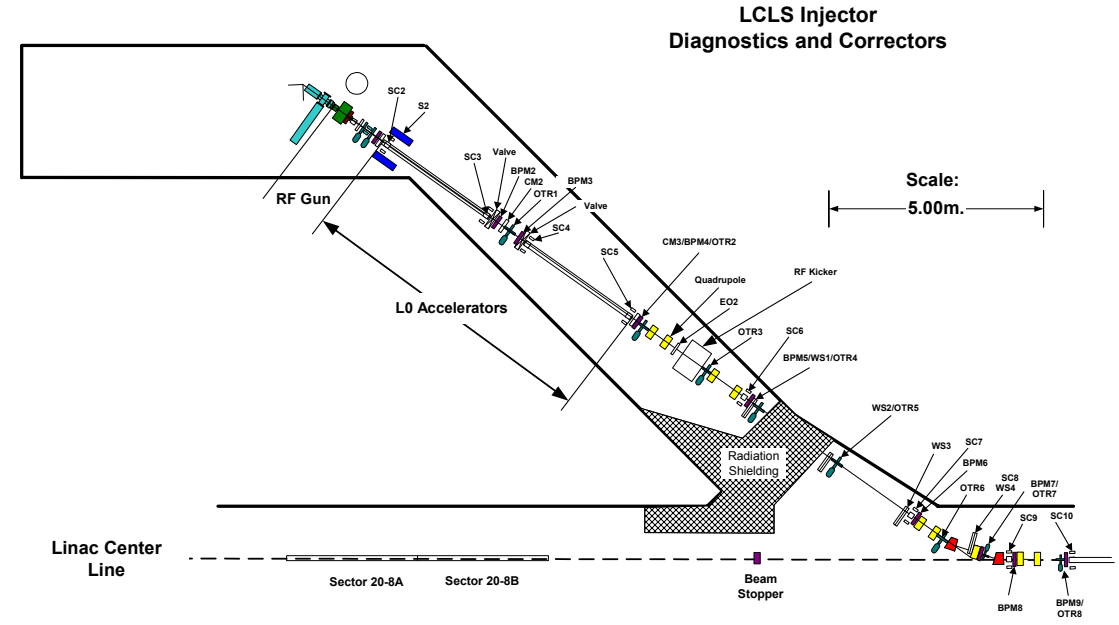

Figure 7.32 LCLS Injector tunnel layout. The L0-linac is composed of the two off-axis accelerator sections. The L1-linac starts with the 21-1B section at right.

7.5.1.1 Layout

The LCLS injector will be housed in an existing off-axis injector tunnel provided by the original SLAC site design. This tunnel is located at the two-thirds point of the SLAC main linac

at sector 21-1 and is oriented at 45° horizontally with respect to the axis of the main linac. The layout of the injector tunnel, with the proposed LCLS beamline installed, is shown in **Figure 7.32**. The gun, injector linac (L0, which is two 3-meter S-band rf sections), emittance diagnostic section (ED0), and 35° bending system are shown, along with variable matching quadrupoles at the L1-linac entrance. Also shown in the figure are the shielding walls required to allow personnel access into the injector tunnel while the main linac is operating (but not the reverse situation).

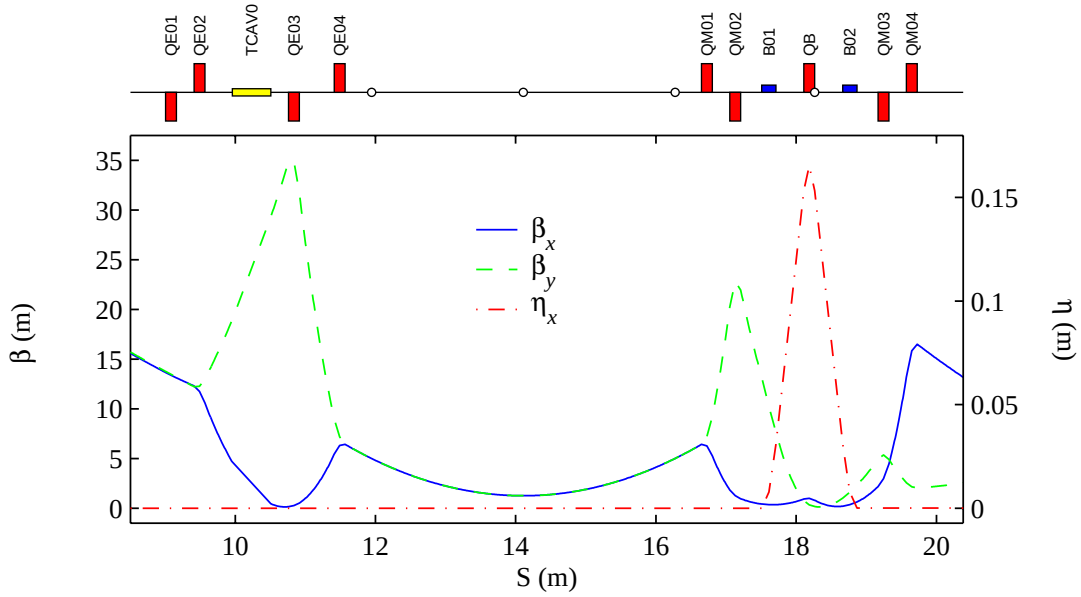

Figure 7.33 Dispersion and beta functions along 150-MeV low energy dog-leg (DL1). Profile monitors are indicated by small circles in top schematic. L0-linac ends at left side ($S \approx 8.7$ m).

7.5.1.2 Parameters

The main parameters of DL1 are summarized in **Table 7.17**. The dispersion and beta functions along the 150-MeV beamline are shown in **Figure 7.33**. Space charge effects on emittance, energy spread, and bunch length are negligible at 150 MeV through the full length of transport from the end of L0 to the start of L1 at 21-1b (see **Chapter 6**).

The four quadrupole magnets (QE01-04; each powered by an independent power supply) just after the L0-linac sections are used to adjust the beta-match into the adjacent 4.7-m drift section, where three profile monitors (OTR and/or wire scanners) are located (see **Figure 7.32** and **Figure 7.33**). This constitutes the emittance measurement section (ED0) at 150 MeV immediately after the L0-linac (see also **Section 7.8.1**). The horizontal and vertical beta functions are forced into the same parabolic sweep through the 4.7-m drift shown in **Figure 7.33**. The profile monitors (PR) are used to measure the *x* and *y* emittances, beta and alpha functions. The PRs are equally separated by

$$\Delta s = \frac{\alpha_0 \gamma \sigma_{\min}^2}{\varepsilon_N} \ , \qquad \textbf{(7.25)}$$

where α_0 is the incoming alpha function ($\alpha \equiv -\beta'/2$), γ is the beam energy in units of electron rest mass, $\sigma_{\min}$ is the rms beam size at the second PR (at the beam waist where the size is smallest), and ε_N is the normalized emittance.

Table 7.17 Parameters of DL1 (the low energy 'dog-leg' beamline).

Parameter	Symbol	Unit	Value
Beam energy	E	MeV	150
Total horizontal deflection (sum of 2 bends)	θ	deg	35
RMS bunch length	σ_z	mm	0.83
RMS energy spread throughout beamline (at 150 MeV)	σ_δ	%	0.10
Momentum compaction	R_{56}	mm	6.3
Second order momentum compaction	T_{566}	mm	140
Length of each of two dipole magnets	L_B	m	0.20
Bend angle of each dipole	$\lvert\theta_B\rvert$	deg	17.5
Magnetic field of each dipole	$\lvert B\rvert$	kG	7.64
Maximum horizontal dispersion	$\lvert\eta\rvert_{\max}$	m	0.165
Projected emittance dilution due to CSR (at $\gamma\varepsilon_0 = 1$ μm)	$\Delta\varepsilon_{CSR}/\varepsilon_0$	%	1
RMS CSR-induced relative energy spread (at 150 MeV)	$\sigma_{\delta\,CSR}$	%	0.008
CSR-induced relative energy loss (at 150 MeV)	δ_{CSR}	%	−0.02

With an incoming alpha function at the first PR of $\alpha_0 = \sqrt{3}$, a constant 60° phase advance is set between each PR. This is the ideal configuration so that the emittance measurement precision is the least sensitive to mismatched incoming beams. The beta function at the waist is chosen based on the desired minimum beam size on the center monitor, $\sigma_{\min}$. For a 65-μm rms beam size at the waist and $\varepsilon_N = 1$ μm at 150 MeV, the beta function at the waist is then $\beta_0 = 1.25$ m, and the incoming beta function, for a 60° phase advance, is four times this value, or 5 meters. Each PR is then separated by precisely $\Delta s = 2.165$ meters. The system provides a robust emittance measurement with optimum precision, minimum beta-mismatch sensitivity, and nominal rms beam sizes (with $\varepsilon_N = 1$ μm) on the PRs of 130 μm, 65 μm, and 130 μm, in order. A similar system is used just downstream of the first bunch compressor, BC1.

7.5.1.3 Coherent Synchrotron Radiation

The effects of CSR (see **Section 7.4.1**) have been studied for the DL1 bends using both *Elegant* and *TraFiC4*. The bunch length is fairly long here (0.83 mm rms), but the bends are strong ($R \approx 0.65$ m). It is possible to completely shield the CSR with a 8.5-mm full height conducting vacuum chamber. Without the shielding, CSR calculations using a transient model with *Elegant* predict an emittance growth of 1%, with a similar result from *TraFiC4* [34]. **Figure**

7.34 shows the temporal distribution of the bunch and the CSR-wakefield, from **Eq. (7.19)**, within the first bend of DL1, using the temporal distribution taken from upstream tracking.

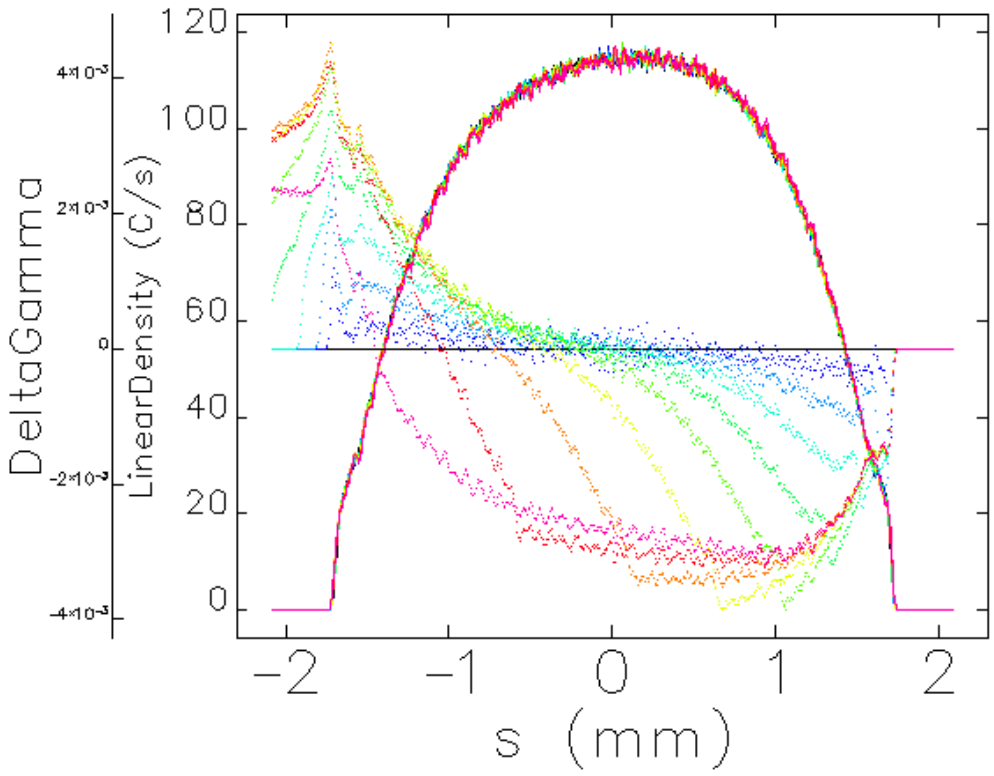

Figure 7.34 Constant temporal distribution of bunch (solid: "LinearDensity") and CSR-wakefield (dots: "DeltaGamma") within first bend of DL1. The variable color traces represent the two functions sampled in each of ten points along the bend magnet.

The variable color traces represent the two functions sampled in each of ten points along the bend magnet. The temporal distribution is nearly constant over the DL1 bend system due to the small energy spread and near-isochronicity of the beamline. The projected emittance growth due to CSR across DL1 bends is small at ~1%.

7.5.1.4 Beam Size, Aperture, and Field Quality

The horizontal beam sizes in DL1 reach peak values of ~100 μm and the sagitta in the bends is 7.6 mm. A 2.5-cm full aperture in the bends is, therefore, adequate. The large dispersion in the DL1 field lens quadrupole, QB, and the strong bends set the tolerances on field quality. **Table 7.18** lists dipole field sensitivities in DL1.

Although the dipoles will be powered in series, their fields may differ slightly due to construction errors. These differences are correctable with trim coils or steering magnets. With the two bend magnets powered in series, the current regulation tolerance is not difficult to meet, at 0.04% rms. This tolerance is set by the path length error induced by a varying field and the need to keep this component of the final electron energy jitter (at 14.3 GeV) stable to <<0.1% (see tolerance budget of **Table 7.5**). The horizontal trajectory oscillations induced by this level of

regulation are insignificant (<<1% of the beam size). Failure to meet the tolerances on the quadrupole content in the bends results in a beta function mismatch (since the dispersion is small in the bends). This mismatch can be compensated with the adjustable matching quadrupoles before and after DL1. The alignment and field strength sensitivities for quadrupole magnets in the DL1 area are shown in **Figure 7.35**. Each sensitivity shown corresponds individually to a filamented emittance dilution of $\Delta\varepsilon_x/\varepsilon_{x0} + \Delta\varepsilon_y/\varepsilon_{y0} = 2\%$.

Table 7.18 Dipole magnet tolerances for DL1. Field harmonics are evaluated on a 20-mm radius and each entry individually corresponds to a 2% emittance dilution.

Magnet	**Quantity**	**Roll Angle** [mrad]	$\lvert b_1/b_0\rvert$ [%]	$\lvert b_2/b_0\rvert$ [%]	$\lvert b_4/b_0\rvert$ [%]
B01 & B02	1 each	14	0.18	30	100

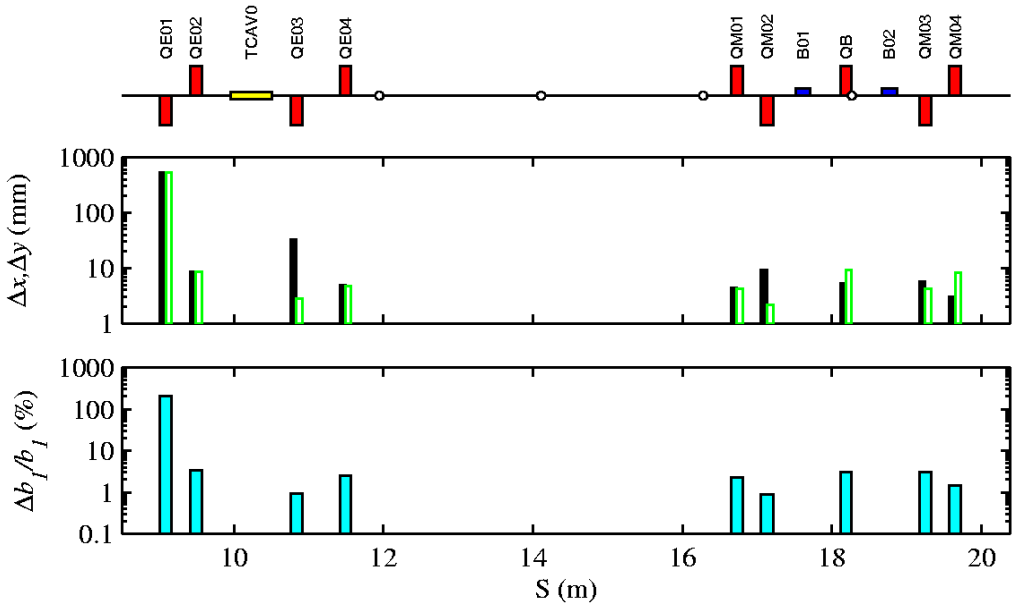

Figure 7.35 Alignment (top: black is *x*, and green/white is *y*) and strength sensitivities (bottom) for DL1 quadrupoles. Each bar individually corresponds to 'filamented' emittance dilution of $\Delta\varepsilon_x/\varepsilon_{x0} + \Delta\varepsilon_y/\varepsilon_{y0} = 2\%$.

7.5.1.5 Tuning and Correction

The DL1 system is quite insensitive to reasonable errors. The emittance and the beam matching can be measured in the diagnostic section following BC1 (BC1 can be switched off if necessary). The field lens, "QB", is adjustable in strength and can be used to partially correct the dispersion if necessary. There are also four independently adjustable quadrupole magnets at the end of the L0-linac, and four more at the input to the L1-linac, any of which can be used to correct the matching in both planes. The beam energy will be held constant in DL1 by monitoring the BPM near the "QB" field lens and adjusting the L0 rf voltage with a feedback loop. The energy spread can be minimized by measuring the horizontal beam profile near "QB" and phasing the L0-linac (see fourth profile monitor in **Figure 7.33**).

In addition, a 55-cm long S-band transverse RF deflecting structure will be located just after the L0-linac (see "RF Kicker" in **Figure 7.32**). This system will be used to 'streak' the bunch for bunch-length, slice emittance, and slice energy spread measurements using screens in the DL1 system. This diagnostic is described in more detail in **Section 7.8.2**.

An insertable tune-up dump will also be included after DL1 in order to allow invasive tuning of the DL1 and upstream systems. The dump will need to handle a 1-nC beam at 120 Hz and 150 MeV or 18-W of average power.

7.5.2 High-Energy Dog-Leg

The requirements for beam transport from the L3-linac to the LCLS undulator are fairly simple. The transport line must:

- Include bends to introduce precise energy and energy spread measurement capability without generating significant CSR or other emittance dilution effects,
- Include precise transverse emittance and matching diagnostics for final verification/tuning prior to undulator,
- Provide adjustable undulator-input beta-matching for the various beam energies (i.e., various radiation wavelengths) desired,
- Not alter the bunch length (must be nearly isochronous),
- Make use of the existing FFTB tunnel and its components wherever possible, as long as the performance of the transport line is not compromised,
- Adjust the vertical beamline angle to remove the 0.3˚ downward linac angle so that experimental areas do not need to be located below ground level.

Energy and energy spread diagnostics are built into a four dipole horizontal inflector beamline (DL2) where the first bend is located just inside the beginning of the undulator hall, which previously housed the Final Focus Test Beam (FFTB). Primarily to meet the small energy spread measurement capability, a doublet of Chasman-Green [35] type cells is used. A cell consists of a dipole pair sandwiching a quadrupole triplet. The horizontal dispersion function in the center of each cell reaches a maximum, while the horizontal beta function converges towards a minimum. A horizontal OTR monitor here ($\eta_x \approx 50$ mm, $\beta_x \approx 1.6$ m) is capable of measuring an rms energy spread of 0.03% at 14.3 GeV with a nominal betatron beam size contribution of only 10% at $\gamma\varepsilon_x \approx 1$ μm (see **Secs. 7.8.2** and **7.8.2.3**).

The Chasman-Green type cells are advantageous since they introduce very little path length energy dependence and generate minimal emittance dilution due to synchrotron radiation. The net system forms a 4-dipole dog-leg (DL2) displacing the beamline horizontally toward the south by 0.45 m. The net R_{56} for the 4-dipole system is set to zero by allowing the dispersion function to reverse sign in half of the bends (see **Figure 7.36**).

Bends of $\theta_B \approx 0.65°$ and $L_B \approx 2.62$ m produce $R_{56} \approx 0$, and a second order term of $T_{566} \approx 73$ mm, which is, for a worst-case energy spread of ~0.1%, completely isochronous (i.e.,

0.073-μm axial position shift per 0.1-% energy deviation). The emittance dilution due to incoherent synchrotron radiation at 14.3 GeV is insignificant at 1%.

In order to include a high-resolution relative energy spectrometer that is insensitive to variable incoming betatron oscillations, the centers of the Chasman-Green cells are separated by a unity optical transformer (+**I**) in the horizontal plane. The signals from two BPMs, one placed at the maximum dispersion point in each cell, are then subtracted to eliminate all incoming betatron oscillations and to enhance the relative energy signal (the dispersion is of opposite sign in the two cells—see **Figure 7.36**). With two BPMs of 10-μm resolution, a relative energy change of 8×10^{-5} can be resolved per pulse. Such resolution will be used in an energy feedback system controlling the L3-linac rf (see **Section 7.8.4**).

Two vertical dipole magnets in DL2 remove the downward vertical angle imposed by the orientation of the SLAC linac. An upward net bend of 0.3˚ is added after the last horizontal bend. This makes the undulator level with respect to gravity. The vertical bends are 0.4 m long and each bend 0.15˚. They are separated by four quadrupole magnets to form a linear achromat (see **Figure 7.36**). These vertical bends are too weak to generate significant momentum compaction or synchrotron radiation (coherent or otherwise).

7.5.2.1 Parameters

DL2 follows the beam switchyard (BSY), which transports electrons from linac to undulator hall. The DL2 parameters are summarized in **Table 7.19**. Beta-functions and dispersion are shown in **Figure 7.36**. The energy spread measuring profile monitor is indicated at $S \approx 1236$ m.

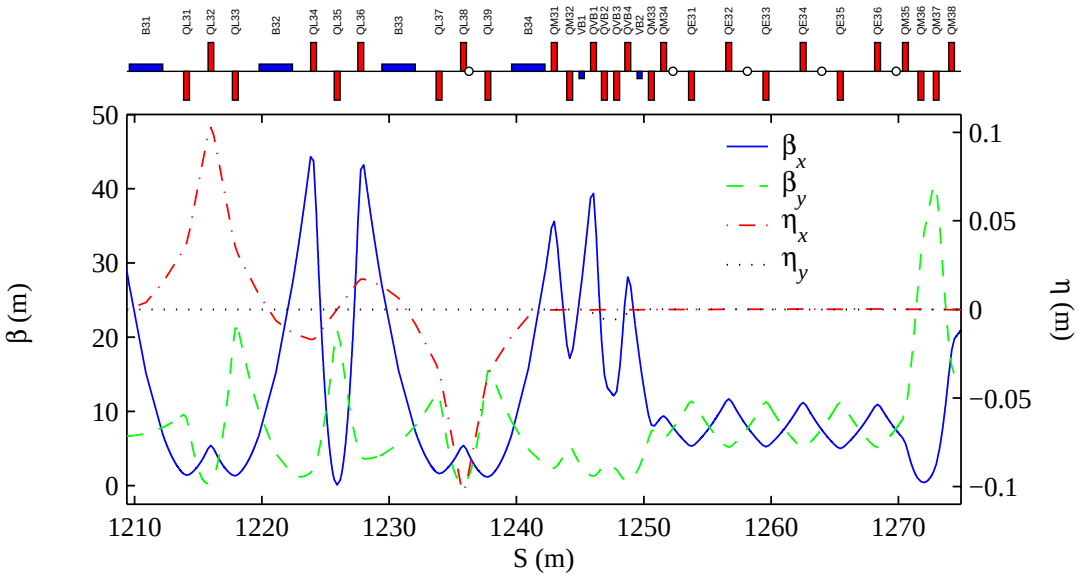

Figure 7.36 Dispersion and beta functions through DL2/ED2 beamline up to undulator entrance. Four-dipole dog-leg (DL2), 2-dipole vertical bend (VB), and final diagnostic section (ED2) are shown. Profile monitors are indicated by small circles in top schematic.

Table 7.19 Nominal parameters of high-energy dog-leg (DL2) beamline.

Parameter	Symbol	Unit	Value
Nominal high-end beam energy	E	GeV	14.35
Total horizontal beamline inflection	Δx	m	0.45
Total vertical beamline angle change (sets a level undulator)	$\Delta\theta_y$	deg	0.30
Nominal rms bunch length throughout dog-leg	σ_z	μm	22
RMS core relative energy spread (14.35 GeV)	σ_δ	%	<0.02
RMS uncorrelated energy spread (14.35 GeV, with wiggler)	σ_{δ_u}	10^{-4}	8
Net momentum compaction	R_{56}	mm	0
Net second order momentum compaction	T_{566}	mm	5
Length of each of four horizontal dipole magnets	L_H	m	2.62
Length of each of two vertical dipole magnets	L_V	m	0.4
Bend angle of each of 4 horizontal dipoles	$\lvert\theta_H\rvert$	deg	0.65
Bend angle of each of 2 vertical dipoles	$\lvert\theta_V\rvert$	deg	0.15
Magnetic field of each horizontal dipole (at 14.35 GeV)	$\lvert B_H\rvert$	kG	2.07
Magnetic field of each vertical dipole (at 14.35 GeV)	$\lvert B_V\rvert$	kG	3.13
Maximum horizontal dispersion	$\lvert\eta_{\max}\rvert$	m	0.103
Emittance dilution due to ISR (at $\gamma\varepsilon_0$ = 1 μm)	$\Delta\varepsilon_{\rm ISR}/\varepsilon_0$	%	0.8
Projected emittance dilution due to CSR (at $\gamma\varepsilon_0$ = 1 μm)	$\Delta\varepsilon_{\rm CSR}/\varepsilon_0$	%	8
RMS ISR relative energy spread (at 14.35 GeV)	$\sigma_{\delta\rm ISR}$	10^{-4}	0.05
RMS CSR relative energy spread (at 14.35 GeV)	$\sigma_{\delta\rm CSR}$	10^{-4}	4.7

7.5.2.2 Coherent Synchrotron Radiation

With constant bunch length over DL2, the optical symmetry is arranged to cancel the CSR horizontal emittance effect arising between bend pairs. The emittance growth is calculated using *Elegant* as well as *TraFiC4* (see **Section 7.4.1)**. The *Elegant* calculations, with a gaussian temporal distribution, result in an emittance growth of 1%. The *TraFiC4* code also predicts 1% for a gaussian temporal distribution. The growth predicted with *Elegant* and using the tracked temporal distribution of **Figure 7.7**, bottom row of plots, is 8% (including all particles, and for $\gamma\varepsilon_0$ = 1 μm), but this is concentrated at the sharp current spikes of the bunch head and tail.

The emittance growth between pairs of bends is 40%, which demonstrates the cancellation symmetry. **Figure 7.37** shows the additional rms energy spread induced by CSR (top) and the normalized horizontal emittance (bottom) along the DL2 bend system (1st bend to 3 meters after 4th bend). To isolate the effects of the DL2 bends, this calculation tracks an LCLS e^- bunch distribution which has not been altered by CSR effects in BC1 or BC2. The full effect with CSR in all bends is examined in **Section 7.6**.

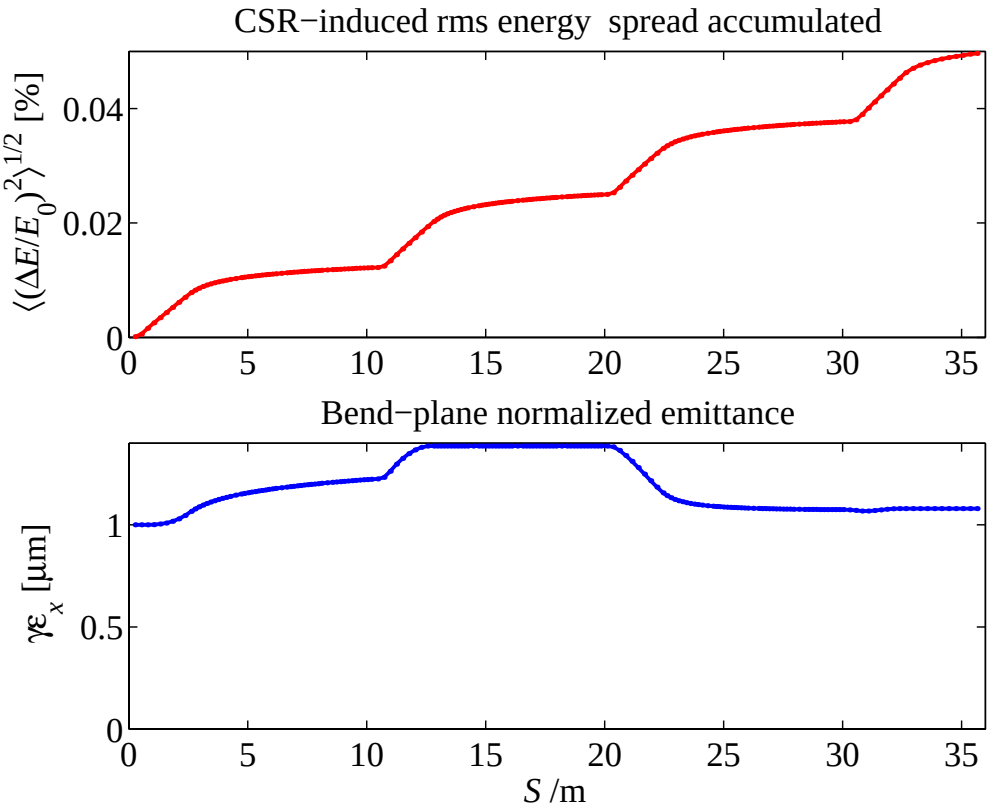

Figure 7.37 Additional rms energy spread induced by CSR (top) and the normalized horizontal emittance (bottom) along the DL2 bend system (1st bend to 3 meters after 4th bend).

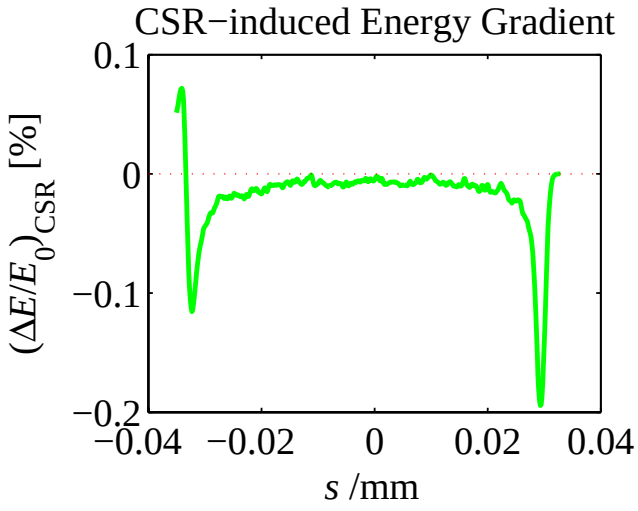

Figure 7.38 CSR-wakefield energy gradient along the bunch generated within DL2 bend system.

The total accumulated CSR-wakefield energy gradient along the bunch generated within the DL2 bend system is shown in **Figure 7.38**. The emittance growth and energy spread is concentrated at bunch head and tail and has little effect on beam parameters sliced on the scale of

the FEL slippage length (~0.5 μm). The energy loss and rms energy spread induced by CSR are 5.5 MeV and 0.047%, respectively.

Figure 7.39 shows the temporal distribution of the bunch and the CSR-wakefield, from **Eq. (7.19)**, within the first bend of DL2, using the temporal distribution taken from tracking upstream of DL2. The variable color traces represent the two functions sampled in each of ten points along the bend magnet. The temporal distribution is nearly constant over the DL2 bend system due to the small energy spread and isochronicity of the beamline. **Figure 7.40** shows the horizontal beam position, x, without CSR (left) and with CSR in all LCLS bends (right), versus axial bunch coordinate, z, for the LCLS bunch profile (i.e., tracked through upstream systems).

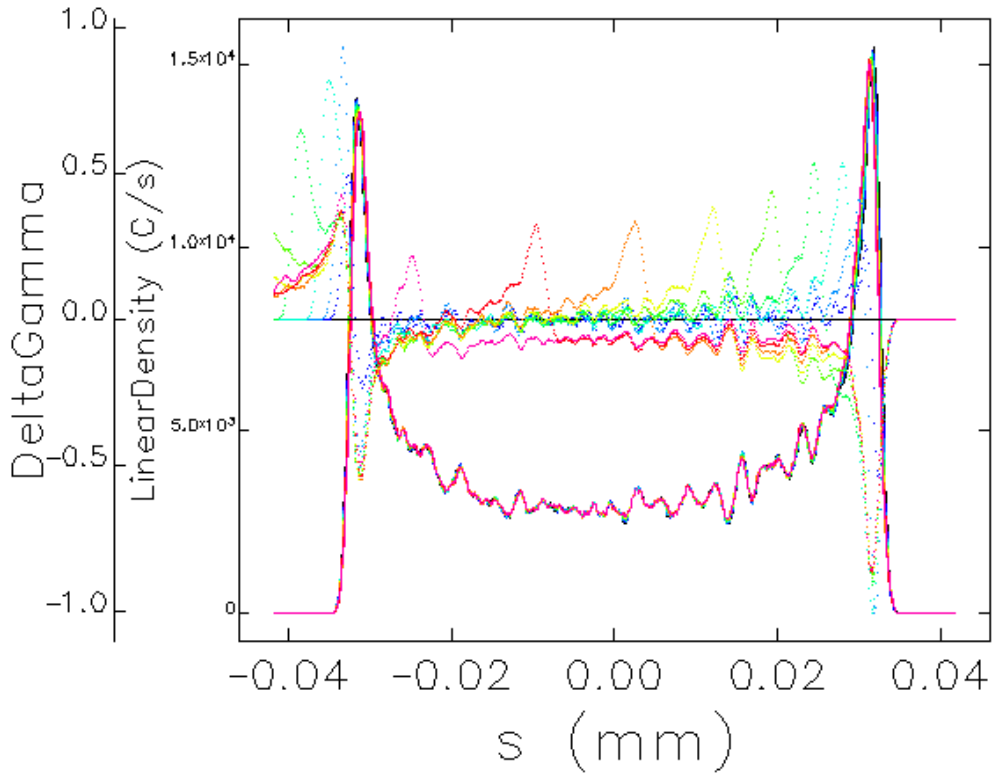

Figure 7.39 Constant temporal distribution of bunch (solid: "LinearDensity") and CSR-wakefield (dots: "DeltaGamma") within first bend of DL2. The variable color traces represent the two functions sampled in each of ten points along the bend magnet.

Since the BC2 chicane also contribute a horizontal emittance growth through correlations of x and x' with z, these might be partially cancelled by 'bucking' the BC2 correlations against those of the DL2 bends. The last bend of BC2 bends to the 'left', while the first bend-pair in DL2 bends to the 'right', so a net horizontal betatron phase advance between these two of $\Delta\psi_x = 2n\pi$ provides the possibility of cancellation. The net phase is set by slight adjustments in the L3-linac phase advance per cell. The BC2/DL2 cancellation is, of course, not completely effective, but at least this arrangement is superior to an odd-π phase advance, which would possibly amplify the emittance growth.

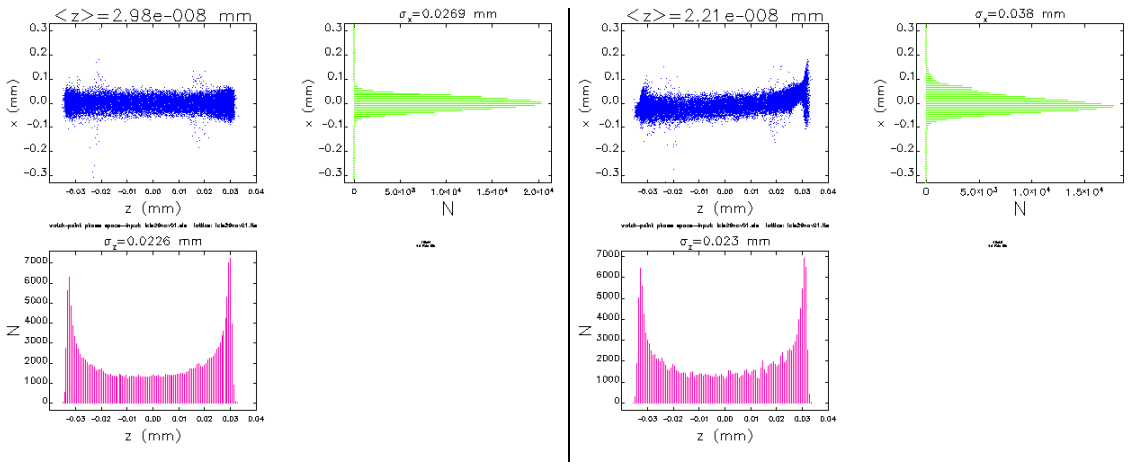

Figure 7.40 Horizontal position, x, without CSR (left) and with CSR (right), versus z, for the LCLS bunch profile (i.e., tracked through upstream systems) after DL2 bends. Projected emittance growth is 2.5 due to CSR in BC2, but dominated by bunch head and tail.

7.5.2.3 Beam Size, Aperture, and Field Quality

The beam size in DL2 reaches a peak value of ~50 μm. A 2.5-cm full aperture is, therefore, completely adequate. The large dispersion in the DL2 quadrupoles sets the tolerances on field quality and gradient errors. **Table 7.20** lists dipole tolerances, while the alignment and field strength sensitivities for quadrupole magnets in the DL2 area are shown in **Figure 7.41**. Each sensitivity shown corresponds individually to a filamented x and y emittance dilution of $\Delta\varepsilon_x/\varepsilon_{x0} + \Delta\varepsilon_y/\varepsilon_{y0} = 2\%$.

Table 7.20 Dipole magnet tolerances for DL2 with an exaggerated 0.05% rms energy spread. Field harmonics are evaluated on a 20-mm radius and each entry individually corresponds to a 2% emittance dilution.

Magnet	**Quantity**	**Roll Angle** [mrad]	$\lvert b_1/b_0\rvert$ [%]	$\lvert b_2/b_0\rvert$ [%]
B31-B34	4	80	2.1	100
VB1 & VB2	1 each	170	5.4	100

The most challenging of these sensitivities are the absolute gradient errors of some of the quadrupoles, $|\Delta b_1/b_1| < 1.5\%$. Although many of these magnets are powered in series, their gradients may differ slightly due to construction errors. A tolerance of <1.5% is not trivially achievable. The effect on the beam, however, is the generation of linear dispersion or beta function mismatch in the undulator. This can easily be tuned-out empirically by adjusting the quadrupoles in DL2. Quadrupole alignment sensitivities are no tighter than 500 μm and do not present a major challenge. Dipole field errors (not listed) are correctable with steering.

A pair of adjustable collimator jaws will be included in the center of the 1st DL2 bend-pair, just upstream of the profile monitor, which can be used to cut beam energy tails. The collimator will be nominally open with a full horizontal gap of ~2 cm, but each jaw will be independently

controlled in order to collimate potential energy tails. The collimator may be useful in diagnosing tails in the electron beam, or for masking beam halo, which generates background radiation in the undulator. It is not envisioned that any significant collimation will be made during normal LCLS operations.

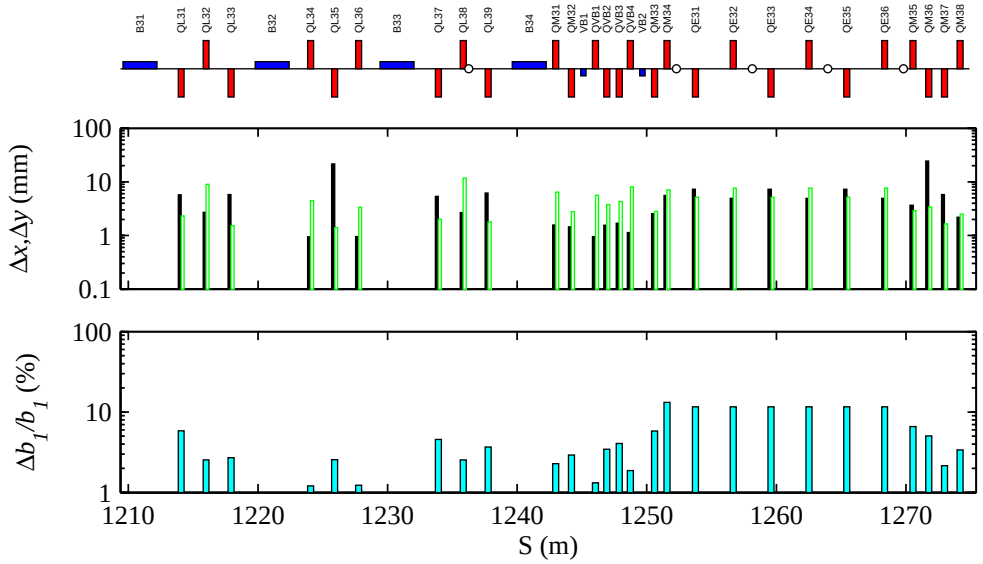

Figure 7.41 Alignment (top: black is *x*, and green/white is *y*) and strength sensitivities (bottom) for DL2 quadrupoles with an exaggerated 0.05% rms energy spread. Each bar individually corresponds to 'filamented' emittance dilution of $\Delta\varepsilon_x/\varepsilon_{x0} + \Delta\varepsilon_y/\varepsilon_{y0} = 2\%$.

7.5.2.4 Tuning and Correction

The dominant error, which will likely arise in DL2, is anomalous linear dispersion or beta mismatch. Quadrupole field strength errors are the most likely cause. The various quadrupoles on separate power supplies will be used in appropriate linear combinations to generate dispersion and matching correction control. The emittance and matching, just prior to undulator entrance, can be measured in the ED2 diagnostic section following DL2.

An insertable tune-up dump will also be included after DL2 in order to allow invasive tuning of the upstream systems. The dump will need to handle a 1-nC beam at 120 Hz and 15 GeV, or 1.8-kW of average power. A fast beam dump will also be located just downstream of the linac and well before the undulator in order to dump the electron beam during conditions of exceptionally poor beam quality. This will help to preserve the permanent magnet undulator fields, and to provide a 'veto' for unwanted pulses. This kicker is only fast enough to veto a 'second' bad pulse.

7.5.3 Dumpline

After leaving the undulator, the "spent" electron beam is separated from the x-ray beam by an array of five permanent magnet vertical dipoles flanked on either side by an electromagnet dipole. These magnets deflect the e^- beam downward into a beam dump. The reason for the permanent

magnets is based on the SLAC Beam Containment System (BCS) philosophy, which discourages power supply excited electromagnets, which could fail. Five permanent magnets and two DC electromagnets are deemed sufficient to guarantee the safe delivery of any electron beam onto trajectories that eventually target in the acceptable region of the dump. The two DC electromagnets are to be operated in series from one unipolar power supply. This together with locked terminal covers at the magnets and the power supply end is sufficient to prevent upward deflection of any electron beam. A meter relay set at a predetermined excitation current value prevents under-deflection of the beam. Should either the meter relay fail or the power supply be set at a value lower than that required for the beam energy, the resulting trajectories would be as shown in **Figure 7.42**. A protection collimator (uncooled) backed by a burn-through monitor (BTM) guarantees beam containment. The particular combination of permanent magnets and DC electromagnets was chosen to minimize the distance from the end of the undulator to the beam dump, to allow operation over an energy range from 2 GeV to 15 GeV and to minimize the vertical range of all trajectories on the dump (see **Figure 7.43**). All magnets are C-type magnets, open to the bottom, to allow easy separation of the x-ray beam from the "spent" electron beam energies.

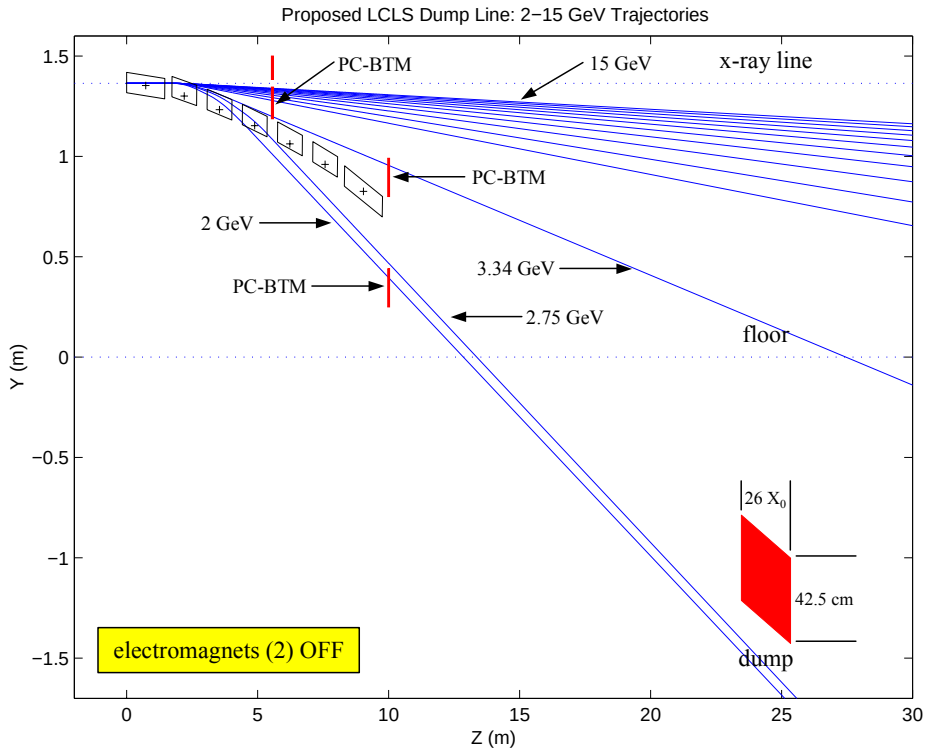

Figure 7.42 LCLS Dumpline 2-15 GeV trajectories: *electromagnets off*. The burn-through monitors (PC-BTM) cover all possible energy beams for the case with tripped electromagnets. The dump is the red block at lower right.

At 15 GeV, the deflection in each permanent magnet is $\theta \approx 0.484°$ for a total bend angle of 2.421° for five magnets. The electromagnets were originally designed and built for the SLAC SLC Linac-to-Arcs matching sections. They were measured to 880A with significant saturation. It

is suggested that 600A should be an upper limit for LCLS. Below that level the excitation curve is linear. At 15 GeV, the deflection in each magnet is then 2.416°. Note, this is approximately the same as the value from all five permanent magnets. The total deflection from five permanent magnets and two electromagnets is then 7.254°.

Lower beam energies are deflected by larger angles and some of the trajectories leave the magnetic field before reaching the last magnet(s) in the array. For example, if 2 GeV is arbitrarily selected as the lower limit, the deflection is 3.632° and the beam will already leave the magnetic field at the end of the first permanent magnet and will not be subject to any of the other magnets' strengths. This effect of the lower energy trajectories "leaving early" and forming straight lines is actually advantageous in that it limits the required vertical size of the beam dump.

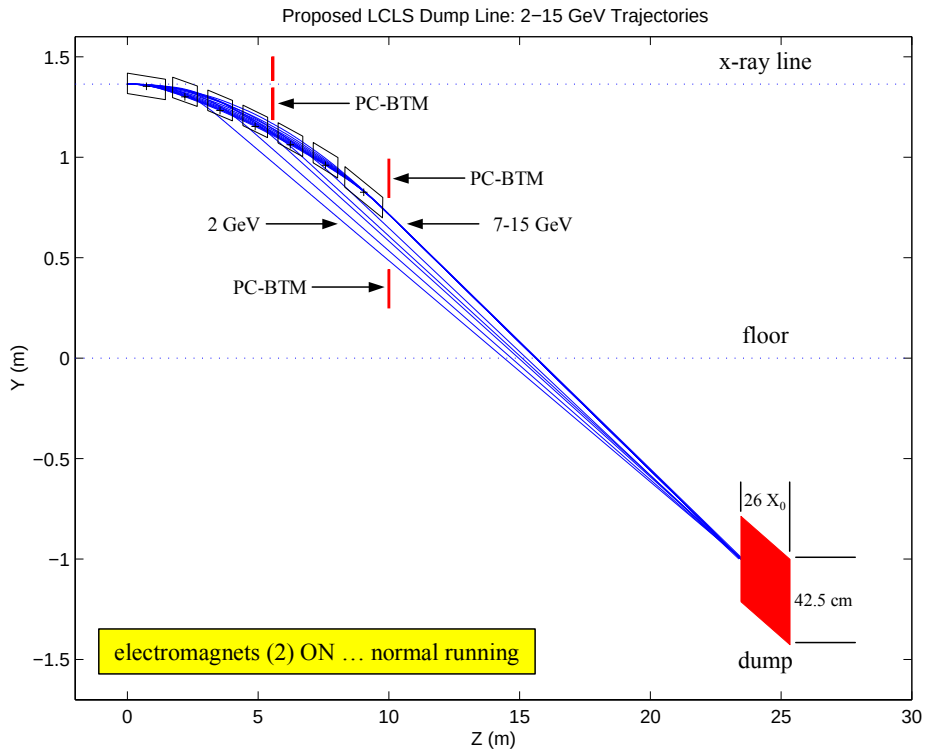

Figure 7.43 LCLS Dumpline 2-15 GeV trajectories: electromagnets on.

7.5.3.1 Beam Containment and Beam Dump

The BCS protection collimator/BTM will be a 3-section device. The first section will contain all electron beam energies above ~3.3 GeV for the case where the first electromagnet dipole is accidentally off. It is optimally located between permanent magnet dipoles #3 and #4 and will cover the vertical region from the x-ray beam down to an elevation just above the magnet poles. The second section will be located down-beam of the second electromagnet dipole and will cover the vertical region from approximately the "allowed" 2-GeV trajectory down to an elevation, which contains at least the "unallowed" 2-GeV trajectory. The third section is above the allowed trajectories at that location and covers those trajectories, which could not be collimated at the first

location.

The collimator sections consist of 3-inch thick carbon steel slabs of appropriate transverse size which act as shower builders, followed by standard BTM's of comparable transverse size. If they are incorporated into the vacuum chambers, the slabs would be stainless steel.

As can readily be seen from the ray trace schematics, the particular arrangement of the electromagnet and permanent magnets results in a small region of beam impingement on the beam dump for all allowed trajectories. This allows in principle the use of the existing FFTB beam dump. It is a device, which was originally designed for the SLC extraction beam dump locations and has a maximum power absorption capacity of 100 kW for appropriate cooling water flow rate. Maximum beam energy rating is 70 GeV. The design is a 16-3/4 inch (425 mm) diameter aluminum cylinder, peripherally water-cooled to minimize radiolysis and cooling water activation. Neither a hydrogen recombiner nor a radioactive water loop is required, i.e. the standard low-conductivity water system (LCW) is sufficient. The dump is 26 radiation-lengths (X_0) long.

The beam dump is to be located below the research yard floor level to more easily shield it than is possible for the present FFTB dump. An elevation of 1 m below ground for the highest trajectory (15 GeV) was selected. This puts the location of the front face of the dump some 24 m downbeam of the entrance to the first electromagnet dipole.

7.5.3.2 Vacuum Chambers

The magnet vacuum chambers are specific to the locations in the dump magnet array reflecting the multi-energy vertical beam stay clear requirements. All chambers are rectangular in cross-section.

The size of the first DC dipole chamber will be approximately the size of the magnet gap and pole width. The first three permanent magnets should share a single chamber to minimize flanges and bellows. The outside width of the chamber will be of the order of the magnet gap. The height will have to be large enough to include not only all the allowed trajectories from 15 GeV down to 2 GeV, but also the unallowed trajectories when either the first electromagnet dipole is off, or when a low energy beam (lower energy than anticipated by the electromagnet current excitation setting) enters the magnetic array. The first protection collimator is built into the chamber and wall, but the BTM is external in air and attached to the chamber.

From this point on, the x-ray beam vacuum pipe is separate from the dump line. The following two permanent magnets also share another rectangular chamber consistent with the beam stay clear requirements of the remaining allowed and unallowed trajectories. The second electromagnet dipole has its own chamber with the second protection collimator built into its lower end wall. The BTM will again be external to the vacuum chamber in air.

Further design study is required to examine the technical feasibility and economic merits of having all five permanent magnet dipoles share one large rectangular chamber including the two protection collimators. Such a chamber is now installed in the six permanent magnets in the FFTB. The remaining vacuum chambers to the beam dump will be of circular cross-section for

economic reasons.

7.6 Six-Dimensional Particle Tracking Studies

In this section the electron beam quality is evaluated by slicing the beam longitudinally after detailed 6D tracking through the injector, compressors, and main linac. The final electron beam density is used to estimate the FEL performance for the nominal LCLS undulator parameters (see also [36]).

7.6.1 Electron Beam Evaluation

The entire LCLS accelerator, from rf-gun to undulator entrance, has been tracked in six dimensions using *Parmela* for the injector, up to 150 MeV, and then tracking these same 2×10^5 macro-particles using *Elegant* [10] for the linac and compressors, up to undulator entrance at 14.35 GeV. The tracking calculations include the following effects:

- An estimated thermal emittance included at the cathode (see **Chapter 6**),
- Space charge forces up to 150 MeV for the LCLS gun and injector,
- Longitudinal and transverse geometric wakefields of the S-band and X-band accelerating structures (transverse wakes are only applied past the L0-linac),
- Bunch compression including all linear and non-linear energy correlations induced in the linacs and compressors,
- Transverse misalignments (past L0) of BPMs, quadrupoles and all 3-meter accelerating structures (BPMs: 150 μm rms, quadrupoles: 150 μm rms, structures: 300 μm rms; all gaussian distributions with 3-σ cuts),
- Trajectory correction (past L0) applied using existing (and planned) steering elements and misaligned BPMs,
- Coherent synchrotron radiation in all bends, with a transient field model integrated over the 'real' evolving *non-gaussian* temporal bunch distribution, and including radiation effects between and after bend magnets [27], [28],
- Incoherent synchrotron radiation effects in all bends, which adds slice emittance and slice energy spread,
- First and second-order lumped optics of each half-magnet (every magnet is split into two pieces),
- Resistive-wall longitudinal wakefields of the micro-bunch in several long sections of 1-inch diameter stainless-steel and aluminum vacuum chambers which are located in the L3-linac and DL2 beamlines.

An example of a final steered trajectory and the related emittance growth over the entire LCLS is shown in **Figure 7.44**. The normalized rms projected emittance here does not include the effects of CSR (see below), and no 'emittance-bump' corrections [18] have been applied to

minimize the emittance growth. The final projected emittance growth for this particular misalignment seed is $\Delta\varepsilon_x/\varepsilon_{x0} \approx 215\%$ and $\Delta\varepsilon_y/\varepsilon_{y0} \approx 160\%$, with $\gamma\varepsilon_{x0,y0} \approx 0.8\ \mu$m. This can be greatly improved by applying well-tested emittance correction techniques [16], [18]. Reference [16] describes a simulation in which 100 different random misalignment cases, with emittance growth of up to 300%, were all corrected to <10% using trajectory bumps. The slice emittance growth along the bunch length also never exceeds ~10% in either plane. The large emittance spikes in the plot at right of **Figure 7.44** occur at locations (e.g., chicanes) where the dispersion is very large and the projected emittance calculation is dominated by dispersion.

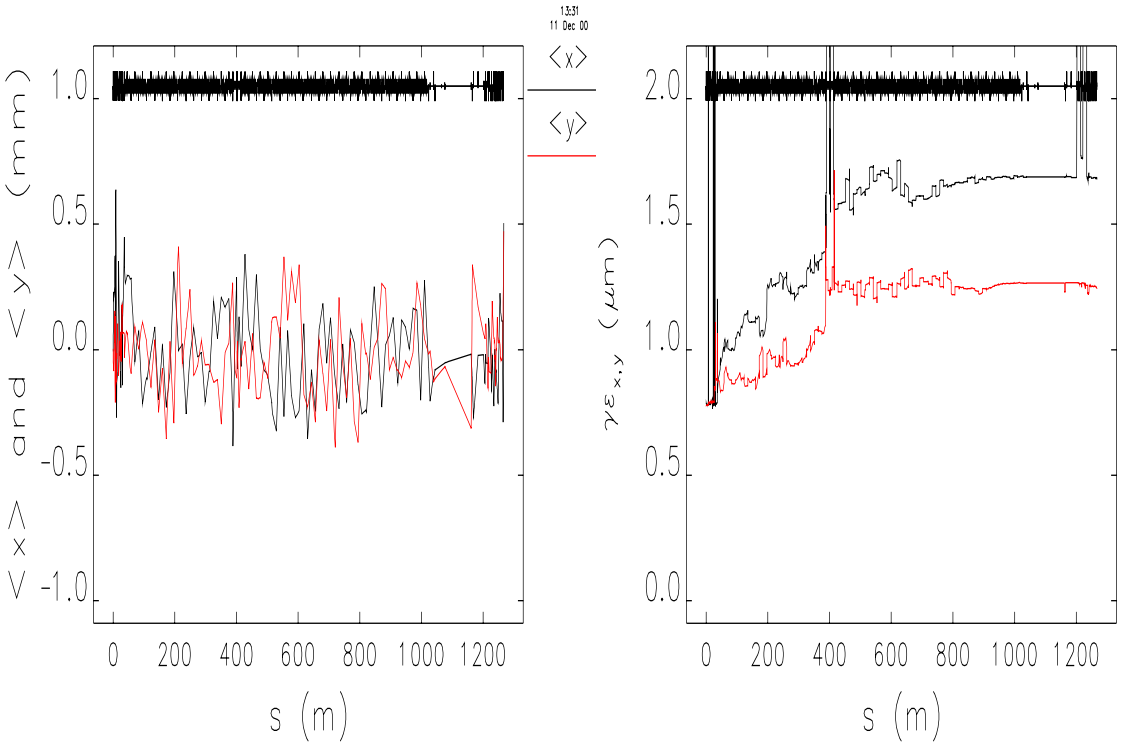

Figure 7.44 An example of *x* (black) and *y* (red) corrected trajectories (left), and projected emittance growth (right; without CSR), given BPM, quadrupole and rf-structure misalignments as described above, along the entire LCLS, from end of L0 to entrance of undulator. The emittance can be corrected using trajectory bumps (not included here).

The projected emittance growth, now including ISR and CSR in every bend magnet, but for perfectly aligned components, is shown in **Figure 7.45**. The net projected horizontal emittance growth is ~2.5, dominated by effects at bunch head and tail, but the slice is still nearly unaffected (see below). The central trajectory has been corrected so that the CSR-generated energy loss in the bends does not cause large betatron oscillations through the linac sections.

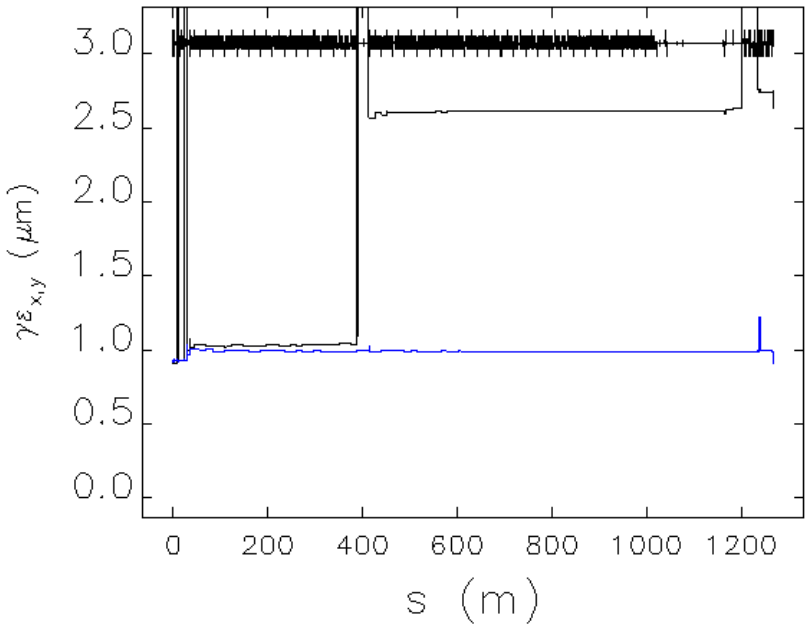

Figure 7.45 Normalized rms projected emittance along the LCLS accelerator, including CSR in every bend magnet, and for perfectly aligned components (black: $\gamma\varepsilon_x$, blue: $\gamma\varepsilon_y$).

The slice emittances, both before and after the accelerator for the case with CSR, is shown in **Figure 7.46**, where "Slice Number" refers to the bunch length coordinate (bunch head at slice-1). The dashed/red lines (x at left, y at right) represent slice emittance at 150 MeV (at L0-linac exit). The solid/blue lines (x at left, y at right) represent slice emittances at 14.35 GeV (at undulator entrance). The large emittance peaks at bunch head and tail at 150 MeV contain very little charge and are washed into the core of the beam after compression and acceleration where they contribute only weakly to the emittance of the core.

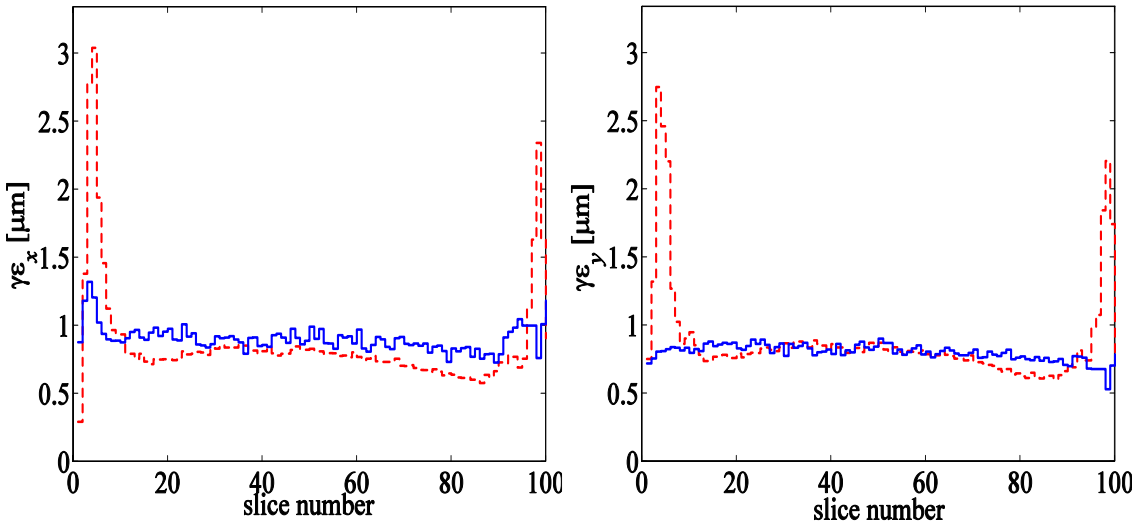

Figure 7.46 Slice emittances (x at left, y at right) at 150 MeV (dash/red) and 14.35 GeV (solid/blue) after entire LCLS accelerator, including CSR. Bunch head is at slice number-1.

The effects of CSR also change the final projected energy spread, but have very little effect on the bunch length. **Figure 7.47** (left) shows the longitudinal phase space at 14.35 GeV at entrance to undulator with CSR effects included in all bends. The rms projected energy spread is 0.1%, including the large tails, but the energy spread of the core slices is <0.01% rms. The spatial *x*-*y* cross-section of the electron beam, including CSR, is shown at right of **Figure 7.47**. Some weak tails out to 10σ are indicated, but the core of the beam is well concentrated. A similar plot (not shown) of x' versus y' shows smaller tails.

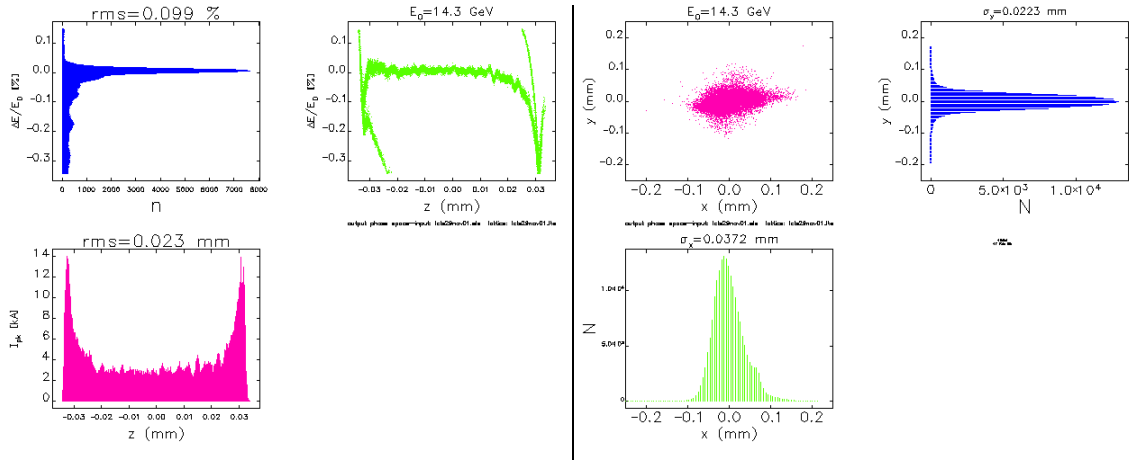

Figure 7.47 Longitudinal phase space (left) and spatial *x*-*y* cross-section (right) of electron beam at undulator entrance at 14.35 GeV, including CSR but for perfect component alignment.

At the left of **Figure 7.48** is the beta-mismatch amplitude per slice. This is defined in **Eq. (7.26)** where the subscripted parameters represent the Twiss parameters of the integrated bunch, while the non-subscripted parameters are the Twiss parameters of each slice. Precise empirical matching of the integrated bunch is possible using profile monitors and adjustments of the DC quadrupole magnets prior to the undulator, but the match of each slice may still vary over the bunch. In fact, matching the integrated bunch may not actually match any of the slices. The transverse RF deflecting structure can be used to help diagnose slice versus projected mismatch effects (see **Section 7.8.2**).

$$\zeta \equiv \frac{1}{2}\left(\beta_0\gamma - 2\alpha_0\alpha + \gamma_0\beta\right) \geq 1 \qquad \textbf{(7.26)}$$

As a simple example, this mismatch amplitude will take a value $\zeta = 1.25$ for $\alpha_0 = 0$ and $\beta/\beta_0 = 2$ (or $\beta/\beta_0 = 0.5$). A mismatch level of $\zeta < 1.5$ in the undulator is desirable [37].

The slice energy spread is also shown in **Figure 7.48** at right. The core of the beam has an rms energy spread of 0.008%. The extreme energy tails ($|\Delta E/E_0| > 0.1\%$) have been cut out here (80% of the particles remain) in order to better reveal the slice energy spread, rather than the extreme tail effects.

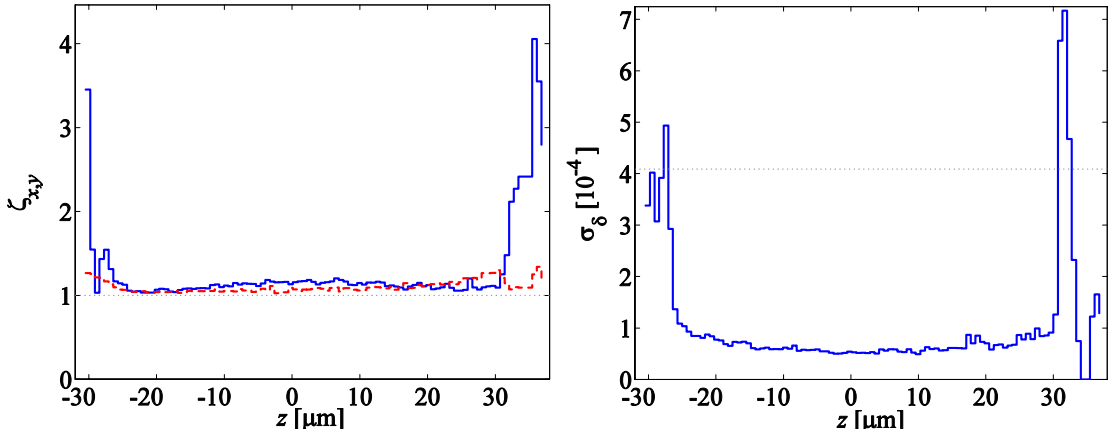

Figure 7.48 Beta-mismatch amplitude (left: *x* solid/blue, *y* dashed/red), and rms relative energy spread (right) and along the bunch at 14.35 GeV, including CSR effects for the 80%-core.

7.6.2 FEL Gain Estimation

Finally, the FEL evaluation described by Ming Xie [38] has been applied to each slice of the bunch. The bunch is sliced 100 times which approximates the worst-case slippage length of the FEL at 1.5 Å (0.7 μm). In this analysis, the electron emittance, peak current, energy, and energy spread of each slice is used to calculate the radiation wavelength, λ_r, the FEL-parameter, ρ, the 3D-power-gain-length, and the saturation power, for the nominal LCLS planar undulator with $K \approx 3.71$, $\lambda_u \approx 3$ cm, $\langle\beta_{x,y}\rangle \approx 18$ m, and $E_0 \approx 14.346$ GeV. **Figure 7.49** shows these 'slice' quantities all plotted against longitudinal position within the bunch. The curves show the parameters calculated over all particles, which are within an energy range $-0.1 \le \Delta E/E_0 \le +0.1\%$, which eliminates 20% of the particles with large energy tails, and therefore the calculations also use a reduced total bunch charge of 0.8 nC. Plots of $\gamma\varepsilon_{x,y}$ and $\zeta_{x,y}$ show *x* (solid) and *y* (dash).

The dotted horizontal lines in the plots represent the full bunch-integrated values, which are in fact irrelevant. **Figure 7.49** shows a 3D power-gain-length of 3.35 m over the longitudinal core of the electron bunch, which would saturate in ~67 m. The dotted lines in the gain-length and power plots are the levels calculated if the bunch-integrated (projected) emittances and energy-spread values are used.

This dimensionless 4D transverse centroid amplitude, $\langle R_4\rangle$, plotted in **Figure 7.49**, reduces to $\langle R_4\rangle = 1$ in the simple instructive case of a one-sigma horizontal oscillation amplitude with $\alpha_x = 0$, $x = \pm(\beta_x\varepsilon_x)^{1/2}$ and $x' = y' = 0 = y$. The effects of CSR in BC2 dominate the variation in $\langle R_4\rangle$, almost completely in the bend-plane (i.e., much more *x* contribution than *y*). In addition, the slice mismatch parameter is shown in *x* and *y*, $\zeta_{x,y}$ (see **Eq. 7.26**), to indicate the beta/alpha function variations along the bunch. The calculation of the gain-length and saturation power does not, however, include the mismatch variation over the slices, $\zeta_{x,y}$, or the transverse oscillation amplitudes of each slice, $\langle R_4\rangle$. These effects, along with undulator wakefields, misalignments, and pole errors, may further increase the gain-length beyond what is shown here.

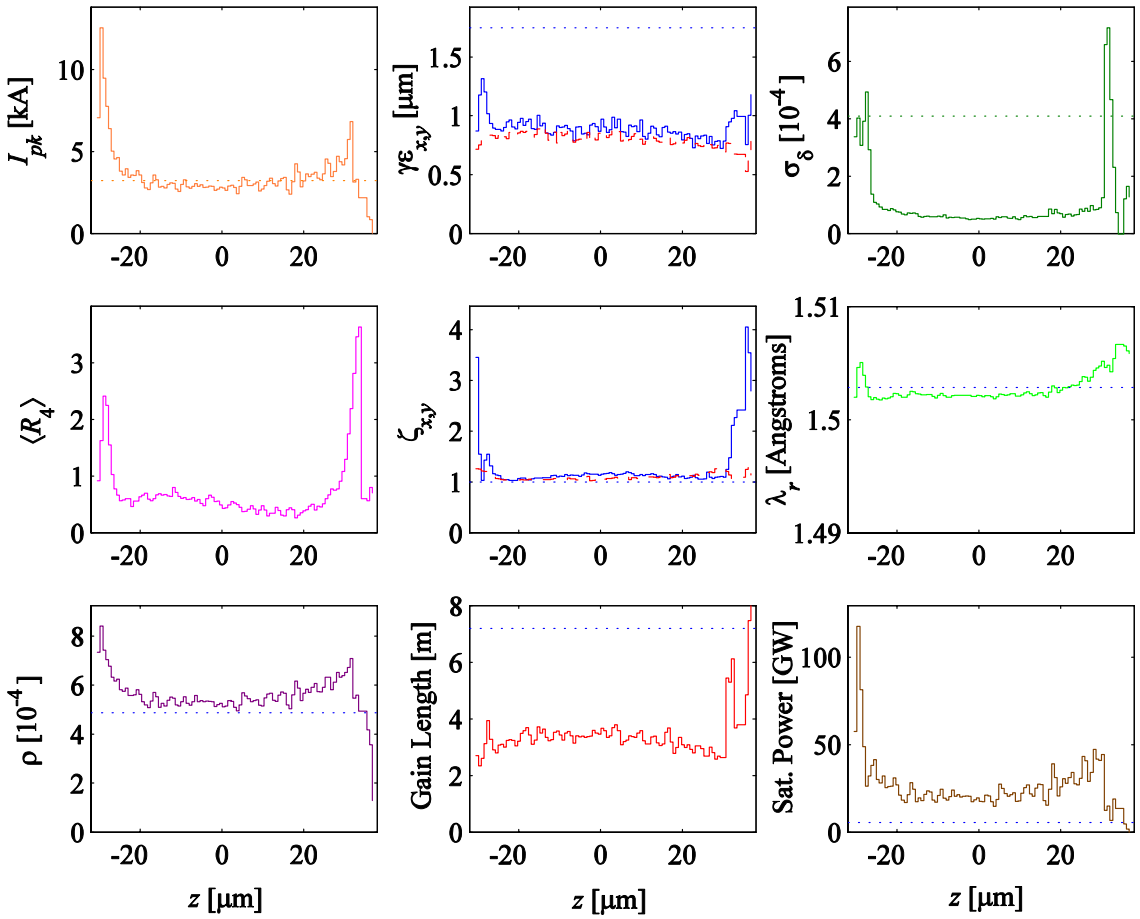

Figure 7.49 Beam and FEL evaluation of the sliced beam at 14.35 GeV using 80% of beam core. The dotted lines represent the bunch-length-integrated values, which are irrelevant.

7.6.3 Beam Jitter Simulations

Full start-to-end jitter simulations have been performed using the tightest (**bold**) tolerances from **Table 7.5** and repetitively tracking the entire system while varying machine parameters such as charge, gun timing, rf phases, and rf voltages, etc. The gun-laser timing jitter is reduced to 0.5 psec here (as compared to 0.7 psec in **Table 7.5**) to reduce the final energy jitter level from 0.1% to 0.06% rms. The simulations apply repeated 6D particle tracking, with 10^5 macroparticles per tracked beam pulse, using the computer codes *Parmela* [11], *Elegant* [10], and *Genesis* [39]. No misalignments are added, so the effects of transverse wakes are not yet included here.

Parmela is used to simulate the photoinjector, ending at 150 MeV, because it includes space charge forces, which are important in the gun and L0-linac. *Elegant* is used for the remainder of the linac, ending at the entrance to the undulator. The macroparticle output of *Parmela* is used directly as input to *Elegant*, which is a 6-D tracking code that includes rf curvature effects, longitudinal and transverse wakefields of the accelerating structures, coherent synchrotron radiation, incoherent synchrotron radiation, and chromatic effects in quadrupoles and dipoles. *Elegant* ignores space-charge forces, which is acceptable because of the high beam energy beyond the 150-MeV injector.

Genesis is used for the FEL calculations. Ideally, *Genesis* would be used to perform full time-dependent calculations for each simulated pulse. However, this would require ~10^7 macroparticles per pulse, and is not practical. Instead, the output of *Elegant* is cut into 136 longitudinal slices; chosen because it is near the number of slippage lengths in the bunch. Each slice is analyzed to obtain relevant first and second moments, i.e., energy, energy spread, centroids of particle position and angle, rms emittances, Twiss parameters, and beam current. Each slice is simulated independently in *Genesis*, under the implicit assumption that slices do not influence each other. The low- and high-energy tails of the beam are also removed, to avoid artificially inflating the rms energy spread.

Jitter is included in the *Parmela* and *Elegant* simulations using gaussian random numbers with a $\pm 3\sigma$ cut-off. The variation in gun charge output, Q, is modeled as $Q = Q_0[1+(0.03)\cdot\Delta\varphi_l]\cdot[1+\Delta E_l/E_l]\cdot[1+\Delta V_g/V_g]$, where $\Delta\varphi_l$ is the laser phase error, $\Delta E_l/E_l$ is the relative laser energy error, and $\Delta V_g/V_g$ is the relative gun voltage error. The coefficient of (0.03) is an empirical value obtained from experiments with a BNL-style gun at the Low Energy Undulator Test Line (LEUTL) at APS/ANL [40].

Table 7.21 Results of start-to-end jitter simulations using *Parmela*, *Elegant*, and *Genesis*.

Parameter	symbol	units	mean	rms	½ quartile range
FEL 3D power gain length	L_g	m	3.53	0.19	0.13
FEL output power	P_0	GW	6.8	1.6	1.0
Relative e^- energy error ($E_0 \approx 14.346$ GeV)	$\Delta E/E_0$	%	0	0.06	0.04
Peak current	I_{pk}	kA	3.3	0.27	0.17
Bunch length (full-width of 80% core slices)	Δt_{FW}	fs	188	19	13
RMS e^- energy spread	σ_δ	10^{-4}	0.8	0.07	0.03
Horizontal normalized emittance	$\gamma\varepsilon_x$	μm	0.80	0.02	0.01
Vertical normalized emittance	$\gamma\varepsilon_y$	μm	0.70	0.01	0.01
Bunch arrival time	$\langle\Delta t\rangle$	fs	0	45	31
Horizontal centroid amplitude (% of beam size)	A_x	%	84	8.0	4.3
Vertical centroid amplitude (% of beam size)	A_y	%	8.0	0.6	0.4

Table 7.21 lists the results of simulations with 227 different beam pulses (i.e., random seeds). The quantities for which statistics are shown are averaged or summed over the central 80% of the slices (the "core slices"), which excludes from analysis the ends of the bunch, which are heavily corrupted by CSR and can be neglected for FEL evaluation. The bunch length is the full length of the core slices. The horizontal centroid amplitude, A_x, for a slice is defined as $A_x^2 = [x^2 + (\alpha_x x + \beta_x x')^2]/(\varepsilon_x\beta_x)$, where x and x' are the position and angle of the centroid of the

slice, α_x and β_x are the projected Twiss parameters, and ε_x is the projected geometric emittance. The vertical centroid amplitude, A_y, is defined in an analogous fashion.

In addition to mean values over the simulated pulses, the table also lists rms deviations and half the quartile ranges. Where meaningful, the rms deviations and quartile ranges are expressed as percentages of the corresponding mean values. The quartile range is the interval containing the central 50% of the samples. Unlike the rms deviation, a few outlier points do not affect it. (For a gaussian distribution, the half-quartile-range is ~70% of the standard deviation.) From this observation one sees that the rms values for the energy spread, horizontal emittance, and horizontal centroid amplitude are all 'pulled' by outlier points.

Figure 7.51 shows gain length strongly correlated with current, energy spread, and horizontal centroid deviation, with the expected sign. For example, higher current produces shorter gain length. One also sees that A_x is on average fairly large, which is surprising given that the trajectory and angle for the ideal beam are steered to zero. However, this is understandable since the steering correction is computed, as in practice, for the entire beam, rather than the core slices with energy tails removed.

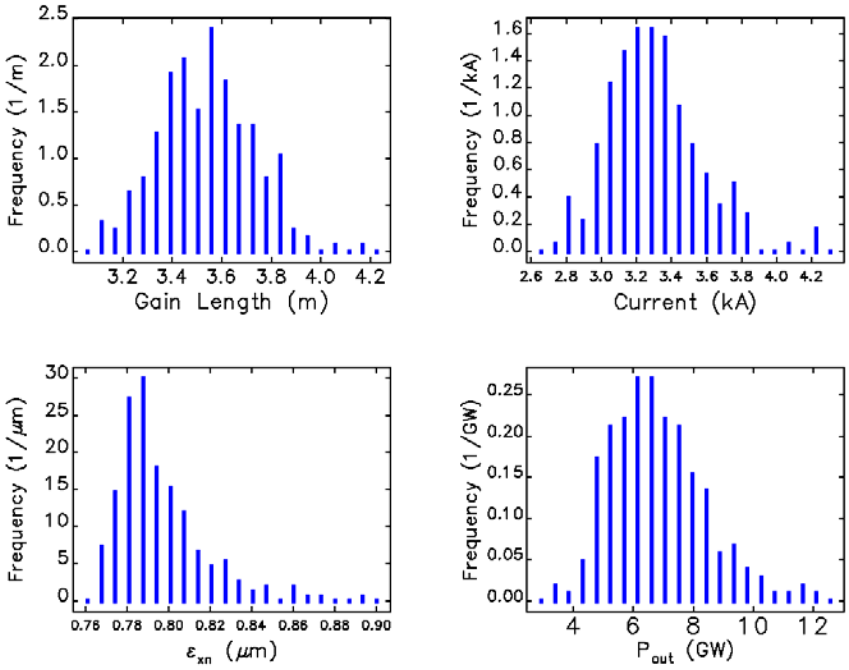

Figure 7.50 Distributions of core-slice-averaged values for the beam and FEL for 227 seeds.

Figure 7.51 shows scatter plots of the core-slice-averaged gain length and core-slice-averaged beam properties for the 227 random seeds (i.e., 227 varied beam pulses).

Computing correlation coefficients between the FEL properties and the jittered parameters indicates which parameters are most responsible for FEL output jitter. This analysis shows that 22% of FEL output power variation is due to gun-laser timing jitter, with another 19% due to L1 rf phase jitter. Similarly, 15-20% of the variation in the light wavelength is due to each of the

quantities laser timing, L0 voltage, L1 phase, and L1 voltage. This illustrates the importance of start-to-end jitter simulation, given that all of these quantities are in the photoinjector or the first section of the linac.

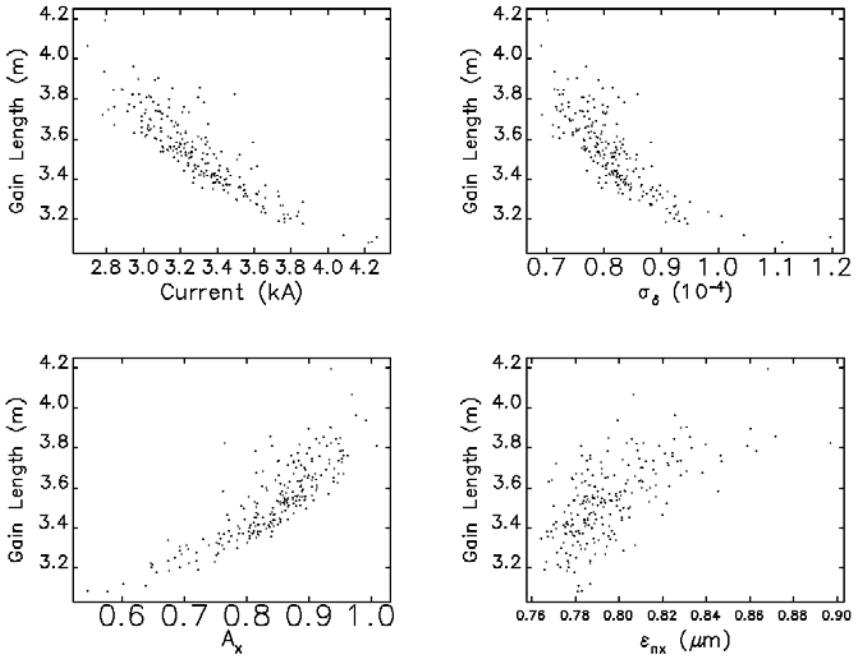

Figure 7.51 Scatter plots of the core-slice-averaged gain length and core-slice-averaged beam properties for the 227 random seeds (i.e., 227 varied beam pulses).

7.7 Radio Frequency Systems

The installed complement of S-band klystrons in the SLAC linac, from sector-21 through sector-30, is capable of accelerating the LCLS beam to the required energy of 14.35 GeV. This includes 6% overhead to allow for klystron failures and maintenance. In addition to setting the electron beam energy, and hence the optical wavelength of the LCLS FEL, precise control of rf phase and amplitude is also required to manipulate the longitudinal phase space of the beam to produce the desired short bunch at the end of the linac. Specifically, the linac rf is used to introduce energy-time correlations for bunch compression and to compensate for wakefields generated by the accelerating structures. This process is supplemented with an additional, higher-harmonic X-band accelerating structure installed ahead of the first bunch compressor. The success of the bunch compression and wakefield compensation schemes requires very tight tolerances for phase and amplitude control of the linac, as described earlier in this chapter.

The jitter tolerance specifies the pulse-to-pulse variation that is acceptable in the linac phase and amplitude parameters and still maintains the desired peak current and energy at the entrance to the undulator. Pulse-to-pulse random variations cannot be corrected by feedback and therefore place upper limits on the phase and amplitude noise level of individual components such as klystrons. Longer-term drifts, ranging from several seconds to several hours, can be corrected by

feedback systems. It is assumed that beam-based diagnostics of relative bunch length and relative energy will be developed with sufficient accuracy to provide feedback for the rf phase and amplitude to control variations slower than ~0.5 Hz.

Some modifications and improvements to the SLAC linac rf system are necessary to meet the tighter tolerances for LCLS operation. The changes must remain compatible with the other SLAC linac functions, chief among which is its role as the injector for the PEP II B-Factory. The rf controls and timing system must coexist with the PEP II injection cycles as well as allow the linac to be switched back to alternate beams for end-station experiments.

Although beam-based feedback will be the final mechanism to stabilize rf phase and amplitude, there are several reasons for keeping the low level rf distribution system as stable as possible. Some development work on feedback tuning algorithms is to be expected before subsystems can be cascaded together. Any extension in the duration over which the beam remains stable and within tolerance makes the task of tuning easier, both during the period of commissioning the accelerator and subsequent operation.

7.7.1 RF Distribution in the Injector and Linac

The major components of the rf system, starting with the gun laser, through the linac and bunch compressors, are shown schematically in **Figure 7.52**. The laser is included in this description since the laser oscillator mode-lock frequency and timing stability are critical to the layout of the low-level rf systems and the phase stability of the beam. **Figure 7.52** shows that there is some rearrangement of the klystrons as a result of the LCLS installation in the SLAC linac, but no new S-band klystron stations, with their associated modulators need be added. This assumes that two of the present klystrons in sector-20, downstream of the positron production area used by PEP II, can be used to power the LCLS injector instead. The loss of a total of three klystrons, plus various section modifications as described in **Table 7.28**, still allows alternate beams to run through the linac for end-station experiments. The only impact is a slightly reduced (~2%) voltage overhead for such beams.

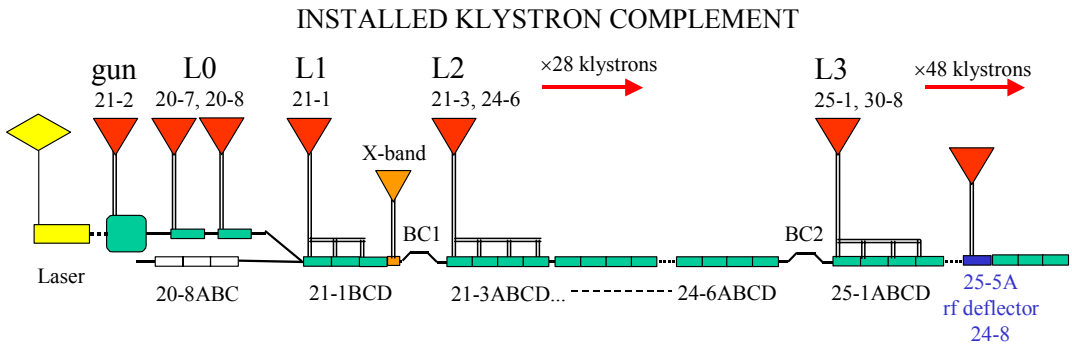

Figure 7.52 Allocation of major components of the LCLS rf system.

The rf gun and the each of the two booster accelerating sections in the L0-linac are each powered by an individual klystron. This is to allow vernier control of the phase and amplitude of the individual sections, which is necessary for both diagnosing and optimizing the performance of the injector at different bunch charges. Individual klystrons also allow the phase and amplitude to be controlled at low power levels with existing technology where electronically controlled devices can provide the necessary fine resolution, pulse-to-pulse response, and reproducibility.

A standard SLAC S-band accelerating section is 3 meters long and normally the power from one klystron is divided equally over four 3-m sections. The L1-linac is made up of only three sections powered by one klystron. The first two sections are shortened by 20 cm to accommodate extra quadrupole/corrector/BPM packages, and the power is divided to give 50% in the first structure and 25% in the other two. The higher gradient in the first structure is slightly advantageous from a beam dynamics point of view.

Following L1, a short X-band rf section, operating at 11.424 GHz, provides 4^{th} harmonic correction to the energy gradient along the bunch before it passes through the first bunch compressor chicane. This section requires a modest power source to operate at 37 MV/m over a length of 0.6 m to generate the needed 22 MV of X-band rf.

The klystrons in the injector and L1 must operate unsaturated to provide for feedback control of the amplitude. A typical operating point would be 5% below the maximum power output of the klystron to allow enough overhead for feedback operation.

The L2 accelerating sections are powered by 26 klystrons plus 2 in standby as spares. The majority of these klystrons can be operated in saturation, with no amplitude control, and having global phase control. Two klystrons near the end of L2 will be operated unsaturated to provide for feedback control of the amplitude. Only one of these two klystrons will be in 'feedback' mode at any one time, with the other reserved as a spare, or as a standard saturated klystron. The feedback klystron will have its phase on-crest to decouple phase and amplitude control. The average phase of L2 will be controlled by feedback adjustment of the phase of the last full sector in L2 (sector-23). This provides a fine resolution control of the average phase, with only one of the four sectors varied, and yet provides adequate dynamic range. Using a sector at high energy will have the least impact on the relative energy profile and hence the focusing lattice in L2.

The L3 accelerating section is powered by 45 klystrons plus 3 klystrons in standby as spares. The majority of these klystrons can be operated in saturation, with no amplitude control, and having global phase control. Two klystrons near the end of L3 will also operate in unsaturated mode to provide for feedback control of the amplitude. The phase for the entire L3 linac will also be controlled by feedback using two or more sectors of L3.

An additional S-band klystron running unsaturated, with independent amplitude and phase control, will power the rf deflecting structure at the 25-5A location in the L3 linac.

7.7.2 Layout and Performance of the Present SLAC Linac RF

The SLAC linac is divided into 30 sectors, of which the LCLS will utilize sectors 21 through 30. The rf distribution for two adjacent, nominal sectors is shown in **Figure 7.53**, showing how the rf power is derived for each sector and distributed to each of the eight klystrons in the sector. A 476-MHz master oscillator located in sector-0 of the linac transmits low-level power along a phase stabilized Main Drive Line (MDL).

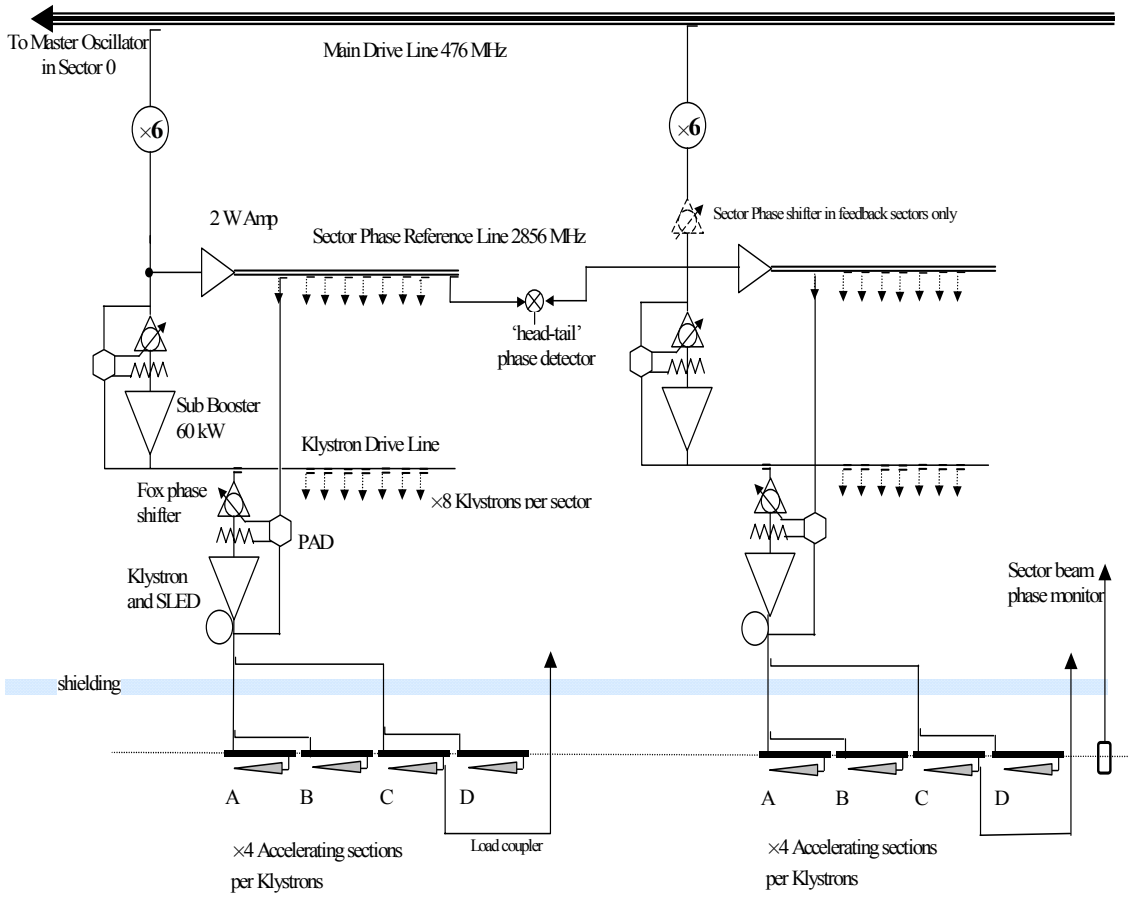

Figure 7.53 Schematic of two adjacent nominal sectors showing distribution of rf power to the klystrons.

An interferometer controls the overall phase length of the MDL to compensate for temperature related diurnal phase variations, an example of which is shown in **Figure 7.54**. At each sector boundary a ×6-multiplier is coupled to the MDL and provides 2856-MHz power for the sector phase reference line and the sub-booster driving 8 klystrons. The sector drive line and the Phase Reference Line (PRL) run the length of one sector and are temperature stabilized over most (but not all) of their length. A 'head-tail' phase detector monitors the phase error between adjacent sectors. Phase errors of the order of several degrees between adjacent sectors are typical in the present distribution system, as shown in **Figure 7.55**, and are the result of imperfect compensation of temperature discrepancies and other various sources.

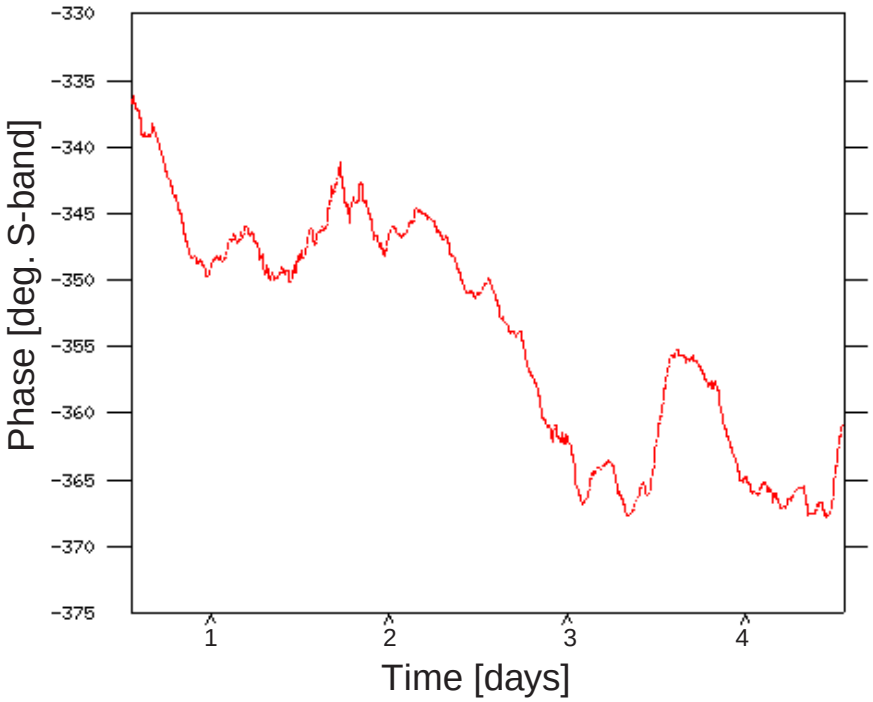

Figure 7.54 Measurement of phase variations seen along the linac main drive line over a period of several days.

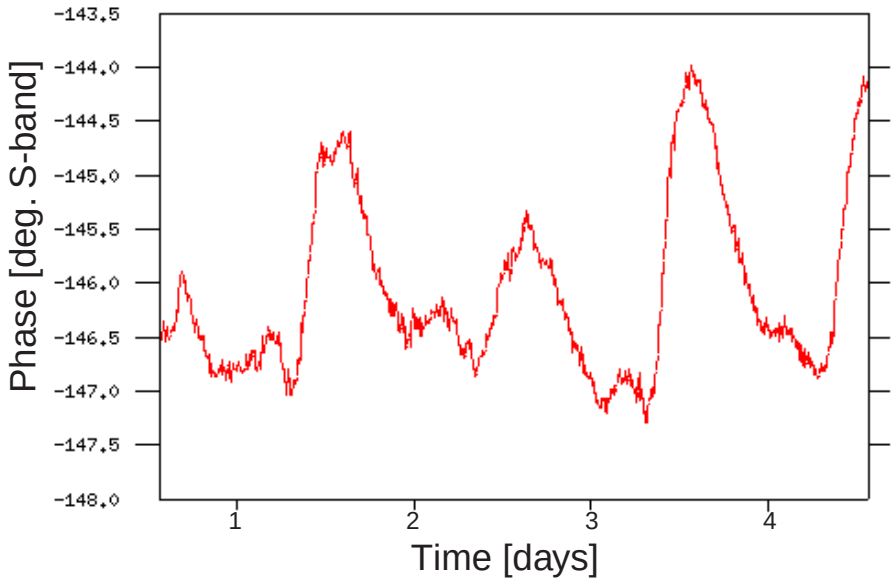

Figure 7.55 Measurement of the phase variations between two adjacent linac sectors over a period of several days.

The control loops for each klystron are shown in greater detail in **Figure 7.56**. The phase variation measured locally at individual klystrons is less pronounced than the errors for the sector drive line.

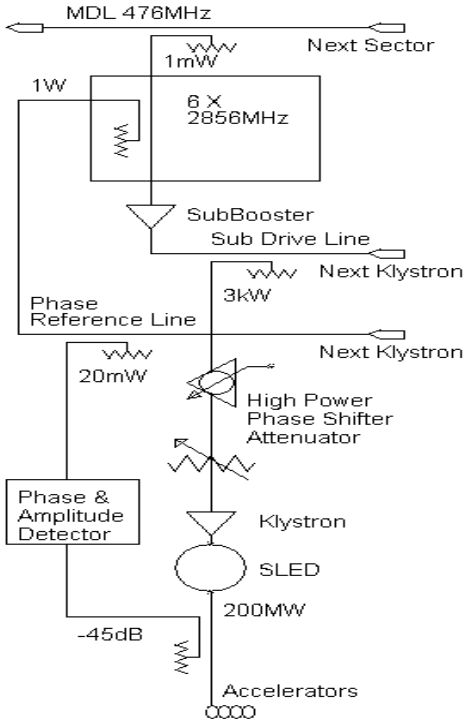

Figure 7.56 Drive power and control loops for a typical linac klystron.

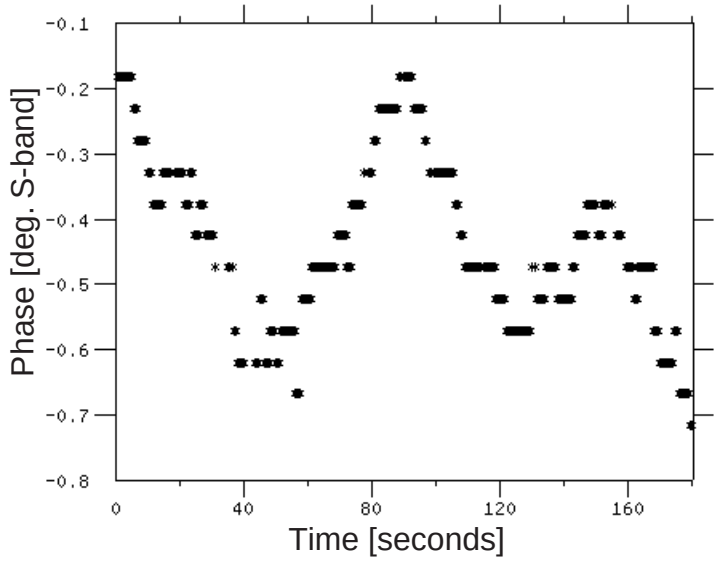

Figure 7.57 Phase variations measured at the PAD of a single klystron over a period of minutes. Each point is an average over 32 beam pulses.

Measurements at the Phase and Amplitude Detector (PAD), in **Figure 7.57**, show typically less than 1º S-band rms phase variation over several minutes. On a 17-second time scale, the pulse-to-pulse phase variation of a single klystron measured at its PAD, shown in **Figure 7.58**, is stable to within 0.07º rms. This data is typical of a sample of 73 operating klystrons that were

scanned during a period when the outside temperature was stable. The pulse-to-pulse amplitude stability over 2 seconds is 0.06% rms, measured at the PAD, as shown in **Figure 7.59**.

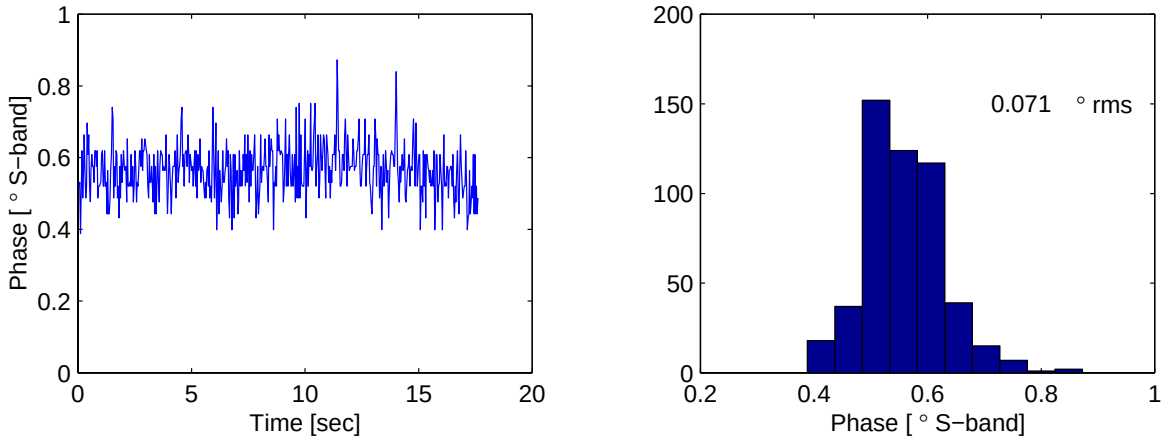

Figure 7.58 Pulse-to-pulse phase variations, and histogram, measured at PAD of a single klystron shows 0.07-degree S-band rms variation over 17 seconds.

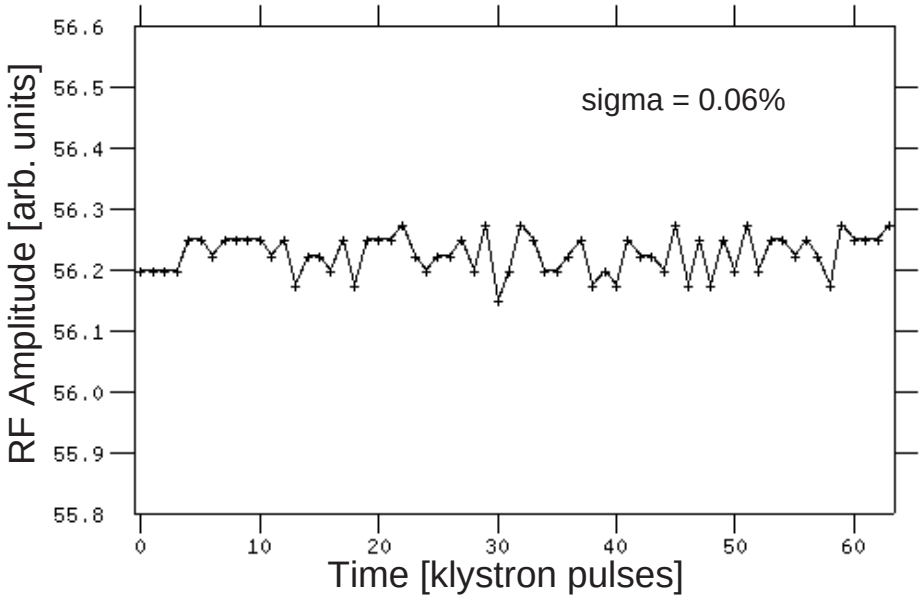

Figure 7.59 Pulse-to-pulse relative amplitude variations measured at the PAD of a single klystron shows 0.06% rms variation over 2 sec (horizontal axis is in 1/30-sec ticks).

Analysis of the performance of the present linac shows that individual SLAC klystrons, when selected for superior stability, can meet LCLS pulse-to-pulse jitter tolerances over a short (~2 sec) time scale. Some improvements are planned for the rf distribution and control system. These will facilitate beam-based feedback control to be applied to the LCLS linac sections. Phase and amplitude control of individual klystrons will be implemented for parts of the linac as well as global sector controls. The phase gymnastics for PEP II injection need to be decoupled from the

LCLS rf distribution while preserving compatibility with the present timing control system. These changes are described in the following section.

7.7.3 Improvements to the RF System

Improvements are being planned for the SLAC linac rf and control systems and will be implemented before LCLS commissioning. The requirements of the subsystems and individual components are reviewed in this section in order that the rf system as whole can function within the tolerance specifications for the LCLS, as opposed to the isolated performance of single klystrons. The reliability of the components is also considered here, since the operating criteria for acceptable noise or drift of components becomes much narrower for LCLS than it has been in the past.

7.7.3.1 Sub-boosters

The present linac uses one klystron sub-booster per sector to provide 60 kW of drive power divided into 8 klystrons. Low power phase control is therefore only done at the input side to the sub-booster klystron and hence changes the phase of all 8 klystrons. The high power mechanical phase shifters on the individual klystrons are only capable of coarser, 0.125° steps. Also they were not designed for pulse-to-pulse operation, typically making only a few tens of phase corrections per day in present linac operation. For comparison, the low-power phase shifter at the input to the sub-booster klystron is electronically controlled and its resolution is within the required tolerances.

The three klystrons in the injector, the L1-linac klystron, and the four feedback control klystrons in the L2 and L3 linacs, as well as the special X-band and rf deflector klystrons, will require individual sub-boosters. This allows low-power phase shifters to be used at each individual klystron, on the input side to its sub-booster, to enable the necessary pulse-to-pulse fine resolution phase control.

The power requirement for individual sub-boosters can be met with solid-state amplifiers. These solid-state-sub-boosters (SSSBs) have the additional advantages of lower noise level and greater reliability than the present klystron sub-boosters.

7.7.3.2 Phase and Amplitude Control Units

Klystrons that are equipped with the new SSSBs and low-power phase shifters will require some revisions to their control systems, as shown in **Figure 7.60**. The existing Phase and Amplitude Detecting units (PADs) meet the LCLS specifications.

The Isolator-Phase-shifter-Attenuator chassis (IPA) contains the high-power mechanical phase shifter. The new SSSB will have an integral low power phase shifter and high power attenuator, both of which will be capable of pulse-to-pulse corrections. In these stations the IPA chassis will no longer be required.

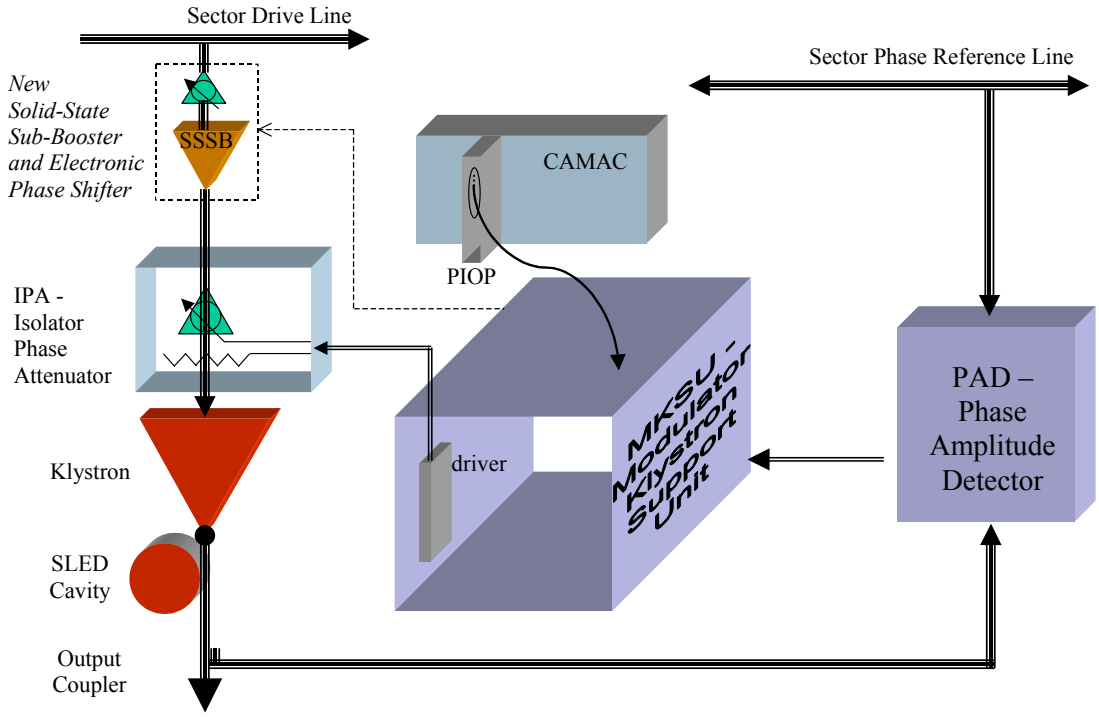

Figure 7.60 Control system components at each klystron station.

The Modulator-Klystron Support Unit (MKSU), which contains the drive hardware for the IPA, will need to be modified to accommodate the additional drivers for a low-power phase shifter and high power attenuator.

A new Parallel Input/Output Processor (PIOP) for the CAMAC control of the MKSU will be designed to accommodate the higher resolution and characteristics of the low-power phase shifter. The new PIOP will also incorporate software to allow for pulse-to-pulse feedback and more diagnostics. The existing PIOP is based on obsolete hardware and cannot be upgraded without extensive redesign work.

7.7.3.3 Master Oscillator

The present Main Drive Line (MDL) transmits 476 MHz along the linac from sector-0 where it is derived from a master oscillator VCO at 8.5-MHz. The 8.5-MHz coincides with the revolution frequency of the damping rings. The frequency shifts on the MDL for the purposes of PEP II injection are not compatible with the fixed frequency, mode-locked laser of the LCLS photoinjector.

A second master oscillator will instead be housed at the LCLS injector, as shown in **Figure 7.61**. This new master oscillator will be phase locked to the MDL to allow for straight ahead beams being run down the LCLS portion of the linac for end station experiments. The master oscillator will be based on a crystal oscillator VCO in a temperature-stabilized oven. The crystal frequency will be chosen to be compatible with the mode-lock frequency of the laser and be a sub-harmonic of 2856 MHz.

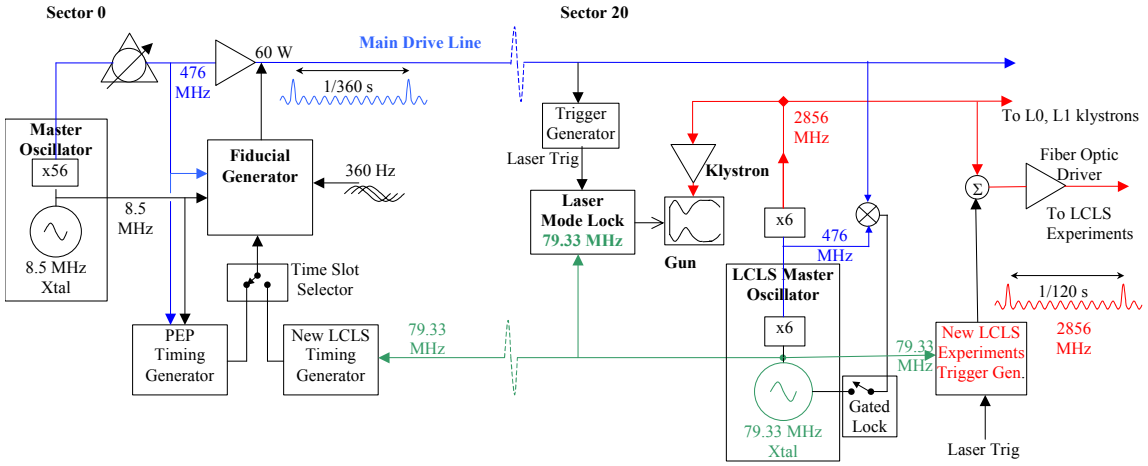

Figure 7.61 Timing and rf distribution in sector-0 and sector-20 of the linac.

The mode-lock frequency of the laser should be as close as possible to 80 MHz, plus or minus one or two MHz deviation at most. This is dictated by the operating range of commercially available lasers that have the best stability properties at the desired wavelength and power for LCLS operation. The present conceptual design uses 79.33 MHz VCO for the mode-lock frequency, which is the 36th sub-harmonic of 2856 MHz. For comparison, the damping ring 8.5-MHz revolution frequency is the 336th sub-harmonic of 2856 MHz. The sector-0 master oscillator VCO and the LCLS VCO frequencies are therefore in the ratio 6:56.

For instrumentation and diagnostics associated with the laser it is convenient to have a phase-locked reference signal close in frequency to 10 MHz. The crystal for the VCO will be at 79.33 MHz and a divide-by-eight module will supply the 9.916-MHz diagnostic reference signal for the laser.

The gun, the L0, and the L1 klystrons are all located close to the LCLS master oscillator and will use this stable 2856-MHz reference as their drive signal. These are the systems with the most stringent phase tolerances and so will share a single, local phase reference.

7.7.3.4 Timing System

The present linac timing system is based on 360-Hz fiducials superimposed on the 476-MHz MDL frequency. Its purpose is to synchronize the beam at the damping ring's 8.5-MHz revolution frequency, and hence the 2856 MHz in the linac, with the phase zero-crossing of the 360-Hz power grid. This feature is to be preserved in the LCLS linac because of shared hardware with the PEP II system.

In order for the LCLS to operate, the fiducial generator must also supply pulses that are synchronized to the zero-crossing of the 79.33-MHz laser mode-lock frequency. This requires a new 79.33-MHz connection from the LCLS VCO to the fiducial generator at the sector-0 master oscillator.

The linac can operate at a maximum of 120-Hz repetition rate, so there are 3 possible "time slots" for it to be synchronized to within the 360-Hz line power cycle. The LCLS beam can

therefore run on a different time slot from the PEP II beam. Beam codes in the timing system will allow PEP II beams to be read out on one time slot and LCLS beams on another. This will allow the same control system hardware, such as the microprocessors, BPMs, etc., to be shared between PEP II and LCLS.

7.7.3.5 Synchronization Pulses for Experiments

As indicated in **Figure 7.61**, a new 2856-MHz phase reference line is planned to provide the LCLS scientific experiments with synchronization pulses. It will take advantage of fiber optic technology to avoid attenuation over the longer distance. Furthermore, only a single fiber is required along the length of the linac, without multiple receivers or couplers enroute. A distribution system for the synchronization pulses is planned in the experimental halls.

7.7.3.6 Beam Diagnostics

Pulse-to-pulse measurements of relative bunch length at 1-10 Hz will be available for feedback control of the rf phase. These will be based on CSR detectors and/or cavity spectral power monitors. The bunch length monitors will be calibrated against the absolute bunch length measurement from the rf deflecting cavity and/or the zero-phasing technique (see **Section 7.8.2**).

Direct measurement of the beam phase with respect to the linac rf is desirable from the point of view of feedback control. However, the thermal sources of phase drift that need to be compensated in the rf distribution system are equally likely to disturb the phase measurement at the 0.1º S-band level required here. A technique of measuring the phase of the beam-induced signal in the accelerating structures relative to the drive rf has been studied. One accelerating structure per klystron is typically equipped with an output coupler on its load, where such measurements can be made. Each sector is also equipped with an S-band beam phase monitor that can also provide some information of the average beam phase with respect to that sector. Both these techniques will be developed as options for phase monitoring and control. This may be a suitable technique for long-term phase control at the 1-deg level in the L3-linac where, with no next bunch compressor, there are no other phase diagnostics.

7.7.3.7 Reliability

Critical klystrons at the gun, L0 and L1 linacs need to be specifically chosen from the complement of SLAC klystrons in order to meet the stability requirements. This sorting technique is presently used in the existing SLAC linac for critical locations in the particle sources and bunch compressors.

7.8 Instrumentation, Diagnostics, and Feedback

Critical to the preservation of the transverse emittance and the generation of a low-energy spread micro-bunch are the precise measurement techniques and correction schemes used to initially commission and maintain the machine. The LCLS accelerator has many phase space diagnostics and correction schemes built into the design. The relevant beamlines and optics are specifically designed to enhance the performance of these critical diagnostics.

7.8.1 Transverse Emittance Diagnostics

There are five different transverse emittance diagnostic stations distributed along the LCLS accelerator, of which four are new installations (the existing sector-28 station [41] will be slightly modified). In three of these cases the emittance measurement is accomplished with four consecutive profile monitors placed along the beamline with appropriate phase advance between monitors to optimize resolution. (Only three monitors are necessary, with four used to improve resolution and provide redundancy.) The two low-energy stations use three consecutive profile monitors over a drift section. These allow non-invasive emittance measurements to be made during normal machine operation, or can also be made using a 'quadrupole-scan' technique, taking advantage of the nominal beam waist on the center profile monitor. The emittance measurement stations and their parameters are summarized below in **Table 7.22**.

Table 7.22 Transverse emittance measurement stations along the LCLS ($\gamma\varepsilon_{x,y} = 1\ \mu$m).

Location	Station Name	Energy (GeV)	σ_x (μm)	σ_y (μm)	No. of Prof. Monitors	Existing
Following L0	ED0	0.150	65-130	65-130	3	No
Following BC1	ED1	0.250	40-80	40-80	3	No
At the end of Linac-2	L2-ED	4.1-4.5	41-72	42-70	4	No
Sector-28 in Linac-3	L3-ED	9.1-10.9	40-55	39-57	4	Yes
Prior to undulator	ED2	14.35	16	16	4	No

The energy range of each diagnostic station listed in **Table 7.22** (e.g., L2-ED) indicates accelerator sections separate the monitors. A range of beam sizes in the table represents the minimum and maximum over the several profile monitors. The ED0, ED1 and ED2 stations listed in **Table 7.22** are dedicated, non-accelerating emittance diagnostic stations designed to produce reasonable sizes in x and y at all monitors. The betatron phase advance between profile monitors (PR) is set to the optimal value for a three or four-monitor station (60˚ or 45°, respectively). These three sections are shown schematically in **Figure 7.33** (ED0), **Figure 7.19** (ED1), and **Figure 7.36** (ED2), with small circles indicating profile monitor locations on the beamline schematics. In the case of ED0 and ED1, drift sections separate the monitors. In ED2, quadrupole doublets separate the monitors. In all cases there exists an upstream variable matching section which can be tuned in order to empirically match the beam. For three (four) monitors, a 60˚ (45°) separation minimizes emittance resolution sensitivity to incoming beta mismatch errors. **Figure 7.62** shows the emittance measurement resolution for the four-PR systems ED2 (solid) versus the phase of an incoming beta-mismatch with a large amplitude of $\zeta = 1.5$, as defined in **Eq. (7.26)**. In this case, the subscripted parameters in **Eq. (7.26)** represent the ideal matched beam and the non-subscripted parameters are the perturbed beam.

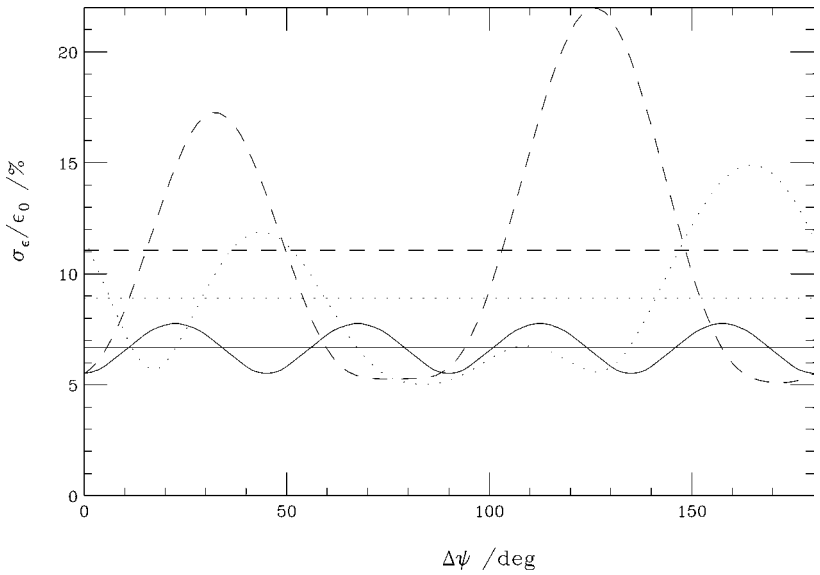

Figure 7.62 Emittance resolution versus beta-mismatch phase for a mismatch level of ζ = 1.5 and beam size resolution of 5%. Resolution is shown for the ED2 sections (solid), the existing SLC sector-28 system (dash) and a modified sector-28 for SLC (dots). Flat lines are the average resolution over all possible beta-mismatch phases.

For comparison, the same resolution sensitivity to mismatch phase is plotted (dash) for the existing linac sector-28 system of the SLC. A modified SLC system is also shown (dots)—(see L3-ED description below). The relative beam size resolution used here is 5%. The average emittance measurement resolution (for ζ = 1.5) for an optimally designed system (6.7%) is nearly a factor of 2 better than that (11%) of a system where profile monitors are a latter addition to an existing optical design (as in the case of the old SLC sector-28 system). The resolution at the worst-case phase is nearly three times better. The equal beam sizes at each of the four profile monitors, in the case of ED2, in both *x* and *y* may also help reduce systematic errors and will simplify the measurement interpretation (i.e., the beam is matched for ED2 when all profile monitors show equal beam sizes).

7.8.1.1 ED0 Emittance Station

The ED0 station (see schematic of **Figure 7.32** or **Figure 7.33**) is used to confirm and optimize the emittance and matching from the injector. It is a resolution optimized three-monitor system (i.e., 60˚ betatron phase advance separates each monitor). This choice is minimally sensitive to incoming beta function errors. For the nominal emittance of $\gamma\varepsilon$ = 1 μm at 150 MeV, the rms matched beam sizes are 130 μm on the two outboard monitors, and 65 μm on the middle monitor. The profile monitors are wire scanners. In addition, the center location, where a beam waist nominally exists, will also include an OTR monitor [33]. This will allow single shot measurements of beam size and also permit 'quad-scans' to be done at this location. The 'quad-scan' is accomplished by varying an upstream quadrupole magnet's gradient and recording the beam size at the various readings. This has the resolution advantage of allowing many more than three beam size measurements to be used in the emittance calculation. It has the disadvantage of

disturbing nominal operations during the 'quad-scan'. The two methods are complementary, and the 3-PR system envisioned allows either method to be used.

7.8.1.2 ED1 Emittance Station

The ED1 station (**Figure 7.19**) is placed directly after BC1. It is crucial for the measurement and empirical correction of dispersion errors generated in BC1. The BC1 chicane can also be switched off to help isolate the different errors of BC1, L1, and DL1. Like ED0, ED1 is a dedicated three-monitor (wire-scanners) emittance measurement section. At 250 MeV the rms matched beam sizes are 80 μm on the two outboard monitors, and 40 μm on the middle monitor. As in the case of ED0, three wire scanners will be used, and an OTR monitor will also be located at the center location where a waist nominally exists.

7.8.1.3 L2-ED Emittance Station

The L2-linac is the most sensitive to orbit variation (note large emittance growth in **Figure 7.15**) and therefore can be expected to require frequent, perhaps daily, emittance optimization. The L2-ED station is placed at the end of L2 (**Figure 7.16**). It is a space-constrained, four-profile-monitor (wire-scanners) station with non-optimal phase advance and an expected emittance resolution of ~10%. This section will be used to empirically minimize the wakefield emittance dilution of L2. Due to space constraints, it is, at present, the least optimized system.

7.8.1.4 L3-ED Emittance Station

The L3-ED station (**Figure 7.18**) is composed of four existing sector-28 profile monitors (wire scanners). The linac optics, however, change somewhat in this area for LCLS operation and therefore a small modification to the existing scanner locations is called for. The first sector-28 scanner will be moved upstream by one cell (24 meters) and the last scanner will be moved downstream by one cell. The LCLS optics then produce an average of 54° per plane between scanners, which is nearly optimal. In fact, the statistical resolution of the SLC configuration is also marginally improved (**Figure 7.62**: dots). The rms beam sizes are not identical at each monitor; however, the phase advance between scanners provides nearly optimal statistical measurement resolution. The L3-ED station will be used primarily to guide BC2 dispersion corrections. Emittance dilution occurring within L3 (see **Figure 7.17**) is expected to be very small due to the short bunch and small energy spread there.

7.8.1.5 ED2 Emittance Station

A final emittance measurement section (**Figure 7.36**) is included just upstream of the undulator entrance. This section will be used to make precise adjustments to the final horizontal and vertical beta functions (using quadrupoles QM33-36 of **Figure 7.36**) and to confirm and optimize the final emittance immediately before the undulator. This emittance measurement section is also used to diagnose potential emittance dilution arising in DL2 through dispersion errors or CSR. Like ED0 and ED1, ED2 is a dedicated emittance measurement section, but with a 16-μm beam size at each monitor in both planes at 14.3 GeV. Four wire-scanners (and redundant OTR monitors at one of these locations) will be used for the profile monitors.

7.8.2 Bunch Length Diagnostics

The peak current delivered to the LCLS undulator is a critical parameter. It is determined by both the charge and the final bunch length. To setup the compression, the bunch length needs to be measured before and after BC1, and after BC2. In addition, once the bunch compressors are set up, a bunch length feedback system will be required for stabilization of the compression. These feedback systems have not yet been fully designed.

The bunch lengths of interest are approximately 1000, 200, and 20 μm rms (10, 2, and 0.2 psec full width, respectively). Measuring 10-psec accurately using a streak camera is fairly standard. The 2-psec measurement is more challenging and probably not reliable. Direct measurement of the final 0.2-psec bunch is quite a different issue. Bunch length monitors [42] designed to use coherent synchrotron radiation (CSR) have demonstrated fast, non-invasive measurements in the LCLS regime. They, however, provide a relative bunch length measurement. Absolute bunch length requires an understanding of the frequency spectrum of the radiation, the various component attenuation functions, and the CSR process.

7.8.2.1 Transverse RF Deflector

A very promising technique to measure the micro-bunch after BC2 is to use a transverse rf deflecting cavity. This idea has been used in the past [43], [44] and has been suggested again recently [45]. The high frequency time variation of the deflecting field is used to 'pitch' or 'yaw' the electron bunch, while the resulting transverse beam width is measured on a simple profile monitor (OTR). This is a reliable, single-shot measure of the absolute bunch length. The technique is completely analogous to a streak camera, but with much better potential resolution. Detailed studies have been made of this technique [46], including wakefield and chromatic effects, and recent beam measurements have also been made [47]. As an additional benefit, 2.44-meter long S-band rf deflecting structures are immediately available at SLAC, where they were fabricated and tested in the early 1960's [48]. A cut-away view of the S-band traveling-wave rf-deflector is shown in **Figure 7.63**.

The bunch length, σ_z, can be calculated from knowledge of the deflecting voltage, V_0, the rf wavelength, λ_{rf}, and the beam energy at the screen, E_s.

$$\sigma_z \approx \frac{\lambda_{\mathrm{rf}}}{2\pi} \frac{E_s}{\left| eV_0 \sin\Delta\psi \cos\varphi \right|} \sqrt{\frac{\left(\sigma_y^2 - \sigma_{y0}^2\right)}{\beta_d \beta_s}} \qquad \textbf{(7.27)}$$

Included here is the product of $(\beta_d\beta_s)^{1/2}\sin(\Delta\psi)$, which is the (measurable) vertical transfer matrix element from angle-to-position and deflector-to-screen. Finally, φ is the rf phase of the deflector ($\varphi = 0$ at zero-crossing) and σ_y and σ_{y0} are the measured vertical beam sizes with rf-on and rf-off, respectively. The voltage of the deflector is easily calibrated using simple BPM measurements as a function of RF phase. **Table 7.23** lists the parameter values associated with this bunch length measurement after BC2. The rf deflecting structure will be placed downstream of the BC2 chicane at 5.4 GeV at the 25-5a location (at $S \approx 475$ m in **Figure 7.18**) where an

existing 3-meter accelerating structure will need to be removed. The screen will be located at the 25-902 location (at $S \approx 520$ m in **Figure 7.18**) where space is available.

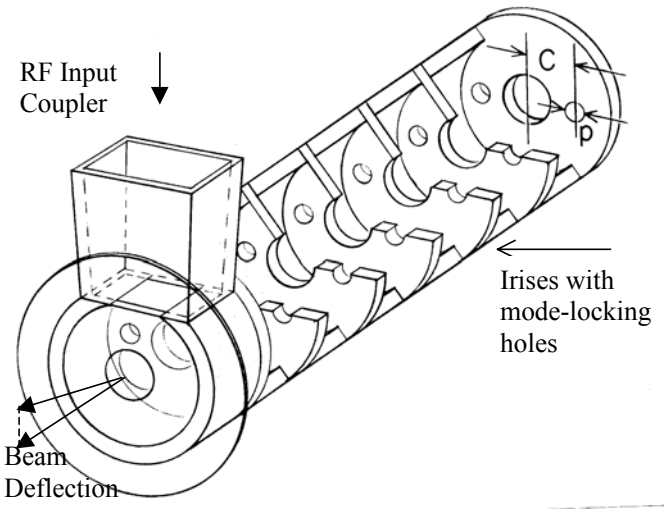

Figure 7.63 Schematic of a SLAC S-band transverse deflecting structure. The kick is vertical here.

Table 7.23 Parameters for bunch length measurement using a 2.44-meter long S-band rf deflecting structure at the 25-5a location and a screen at the 25-902 location.

Parameter	symbol	value	unit
rf deflector voltage	V_0	20	MV
Peak input power	P_0	25	MW
rf deflector phase (crest at 90°)	Φ	0	deg
Nominal beam size at screen	σ_{y0}	76	μm
Beam size with deflector on (two-phase mean)	σ_y	282	μm
Beta function at rf deflector	β_d	56	m
Beta function at screen	β_s	60	m
Betatron phase from deflector to screen	$\Delta\psi$	65	deg
Normalized rms emittance	ε_N	1	μm
Beam energy at deflector	E_d	5.4	GeV
Beam energy at screen	E_s	6.2	GeV
RMS bunch length	σ_z	22	μm

The transverse rf deflector will be powered in a pulse-stealing scheme where the rf is switched on at ~1 Hz, while the machine operates at 120 Hz. An off-axis screen is used to intercept the 'streaked' electron beam, while a pulsed opposite-plane kicker (or an rf phase at non-zero crossing) is used to knock that bunch over and into the screen. The rf 'streak' will be applied vertically ('pitch') so that beam correlations in the *x-t* plane, caused by CSR forces in the

BC2 chicane, might be easily diagnosed. A simultaneous horizontal kicker will be used to move the beam horizontally to the off-axis screen. This keeps transverse wakefields from adding to the beam 'pitch', which would occur if a non-zero deflector phase were used. In addition to being used for bunch length measurements, the 'streaked' beam on the profile monitor also allows the possibility of doing 'slice' emittance measurements [49] in the horizontal plane.

Figure 7.64 shows the effect of a 20-MV vertical deflector. The parameters are those given in **Table 7.23**. The figure shows three plots in two panels (deflector OFF at left and ON at right). At upper left of each panel is the bunch population in *y*-*z* space. At upper right and lower left are the vertical (*y*) and temporal (*z*) projected distributions, respectively (note 22-μm rms bunch length). The particle tracking is performed using *Elegant* and includes wakefields, second-order optical effects of momentum deviations, and the sinusoidal time variation of all rf fields. In this case the 'streak' is in the vertical plane, while a centroid kick is applied horizontally (not visible in these plots). With the 'streak' vertical, but the centroid kick horizontal (using a simple kicker just downstream of the rf deflector), no large transverse wakefields are generated vertically between the deflector and screen.

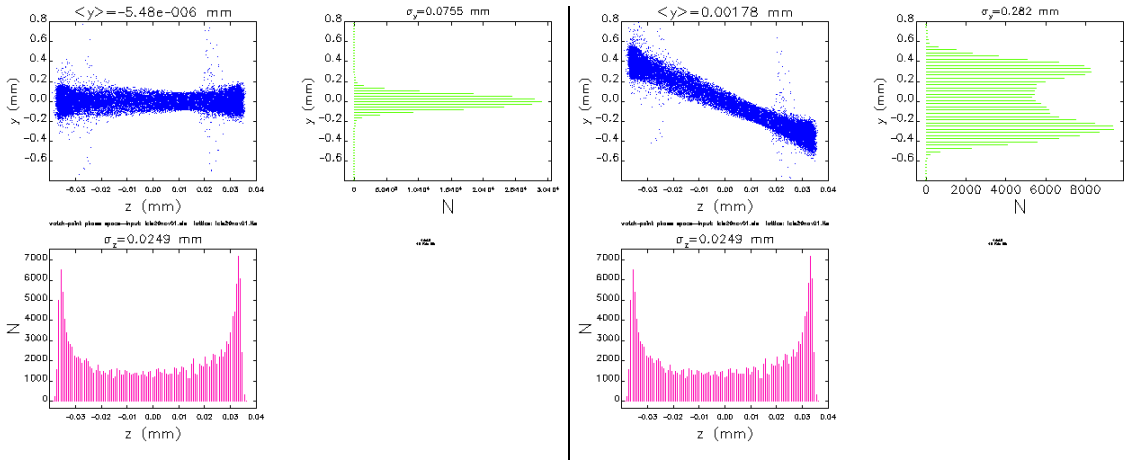

Figure 7.64 Vertical vs. longitudinal space at 25-902 screen with rf deflector OFF (left) and ON (right) showing 'streaked' beam. The rms vertical beam size on the screen is nominally σy0 ≈ 76 μm but increases to σy ≈ 282 μm with rf deflector ON (bunch head at z < 0).

The effects of transverse wakefields upstream of the rf-deflector can introduce an initial *y*-*z* beam correlation ('pitch'), which, for very large levels, might bias the bunch length measurement result. This initial correlation can be mitigated by setting the rf-deflector at each rf zero-crossing point (i.e., 0 and π) in sequence. The three-beam size measurements ($\varphi = 0$, $\varphi = \pi$, and $V = 0$) are then used in parabola-fit (much like a 'quad-scan' emittance measurement) and the systematic error due to the wakefield will be cancelled. In addition, the initial *y*-*z* tilt is measured and might be used to determine upstream trajectory changes necessary to cancel this wakefield (see ref. [47] for real examples of this technique).

As shown in **Figure 7.65**, the temporal structure of the horizontal emittance can also be viewed using the vertical deflector. This will help to diagnose the effects of CSR in the BC2

chicane where *x-z* correlations ('yaw') in the beam are the dominant mechanism for projected emittance growth. The CSR effects of all bends are included in this figure.

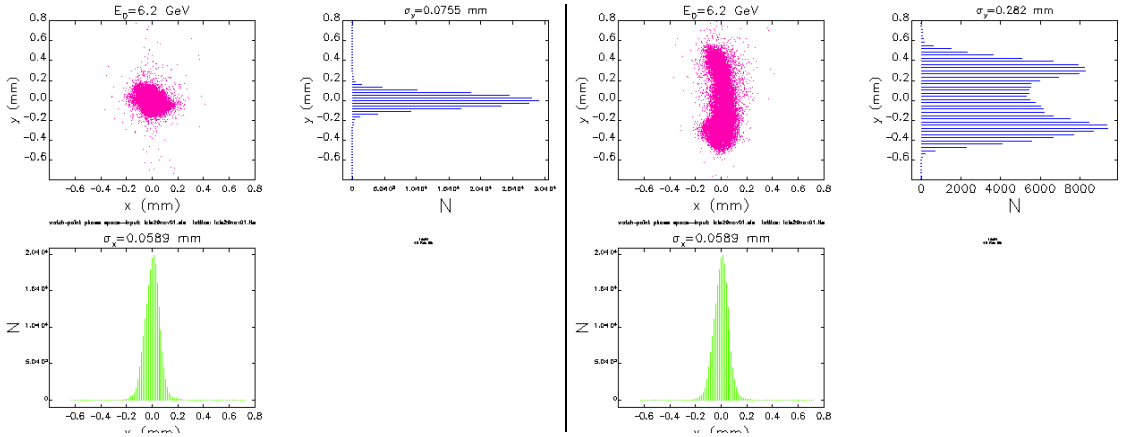

Figure 7.65 Vertical vs. horizontal position on 25-902 screen for V0 = 0 (left) and V0 = 20 MV (right). The rms vertical beam size on the screen is 76 μm (left) and 282 μm (right). In this case, CSR is included for DL1, BC1, and BC2 upstream of the deflector, which generates the variable x-y correlations along the bunch seen at right.

The rf deflector can also be used to make a direct measurement of the detailed electron bunch population in longitudinal phase space. Another OTR screen (PR31) is installed downstream of the deflector, at a location of large horizontal momentum dispersion where the horizontal beta function is small enough so that the horizontal beam extent across the screen represents dominantly the momentum spread in the beam. By switching on the transverse rf as a vertical deflector and allowing the 'pitched' bunch to propagate to this new screen, the vertical extent across the screen then represents the time axis along the bunch, while the horizontal is the energy axis. This requires a stable rf phase ($|\Delta\varphi| < 0.2°$) at zero-crossing (i.e., $\varphi = 0$ or $\varphi = \pi$) so that little trajectory centroid kick is induced over the potentially long distance to the new screen. This also requires the vertical phase advance between deflector and dispersion screen to be approximately $\pi/2 + n\pi$, which has been arranged in the design of the L3-linac optics. This is an infrequent technique, which requires the beam to be dumped after intercepting the screen.

Figure 7.66 shows a simulation of this process through the LCLS, where the deflector is set at 20 MV with no centroid kick, and the screen is located 760 meters downstream at a location (at $S \approx 1218$ m in **Figure 7.36**) with momentum dispersion $\eta_x \approx 50$ mm and beta functions $\beta_x \approx 1.6$ m, and $\beta_y \approx 14.8$ m. The beta functions are still large enough to wash out some of the temporal and momentum resolution, but the image on the profile monitor (at right) is still a good representation of the real bunch population in longitudinal phase. Using this arrangement, the slice energy spread, and its temporal structure, can be measured to a resolution of 0.02% if the horizontal screen image is resolved to 10 μm.

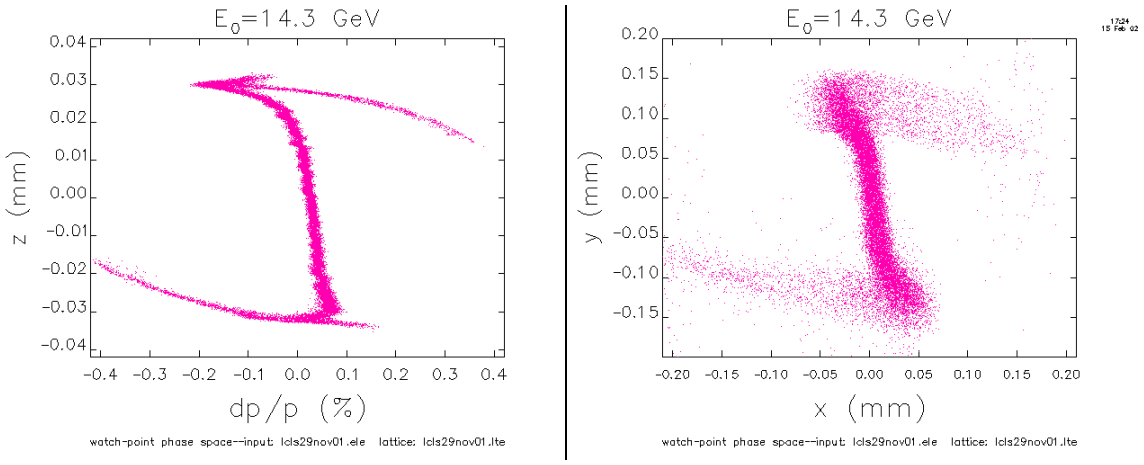

Figure 7.66 Longitudinal phase space (left) [σz ≈ 22 μm] and its PR31 screen reconstruction (right) at S ≈ 1218 m in Figure 7.36 at 14.3 GeV (σy ≈ 90 μm, σx ≈ 40 μm), with rf deflector at 20 MV and no centroid kick (bunch head a bottom: z < 0, y < 0).

In addition, a shorter RF deflector will also be located just after L0 at 150 MeV (see **Figure 7.32**: "RF Kicker" and **Figure 7.33**: "TCAV0"). This structure is just 55-cm long and presently installed in the SLAC linac where it has been unused for many years. A location just after L0 allows it to measure both slice emittance and slice energy spread. With 1-MV applied (1.3 MW), the OTR screen between the DL1 dipoles ($\eta_x \approx 150$ mm) is used to directly measure longitudinal phase space, including slice energy spread, absolute bunch length, and temporal pulse shape. This deflector will be powered by the existing 20-5 klystron. **Figure 7.67** shows a simulation with deflector off and on. The *x*-*y* screen image with deflector on (right) should be compared to the longitudinal phase space plot at top of **Figure 7.6**.

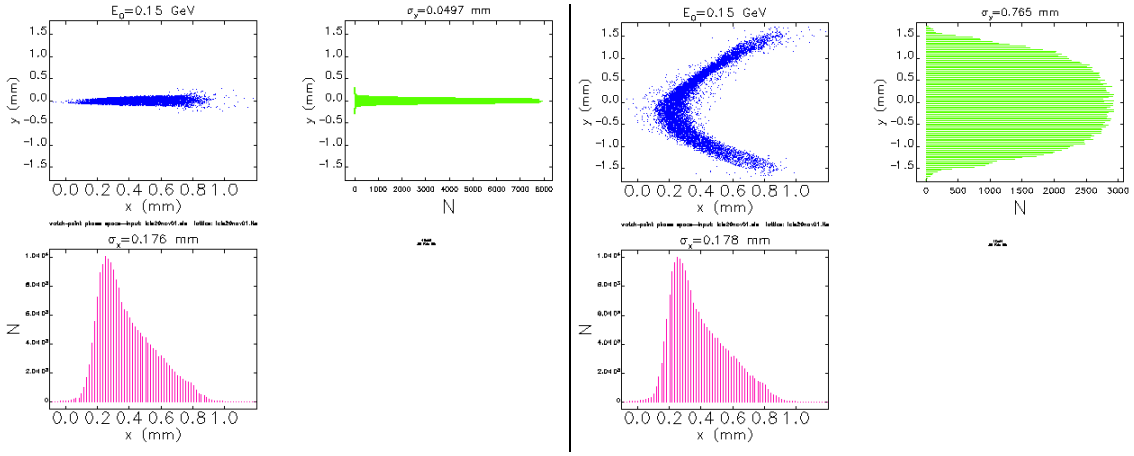

Figure 7.67 Simulated profile monitor between DL1 bends with 55-cm rf deflector OFF (left) and with voltage set to 1 MV (right). The plot at right is a direct measurement of the longitudinal phase space, including slice energy spread and absolute bunch length.

Since the bunch can be 'streaked' in time vertically across a profile monitor, it is also possible to measure the horizontal slice emittance. This is easily accomplished by observing the

beam on the center OTR profile monitor of the ED0 emittance diagnostic section (at $S \approx 14.1$ m in **Figure 7.33**). With a beam waist ($\alpha_x = \alpha_y = 0$) nominally located at this monitor, a quadrupole gradient scan can be done while measuring the sliced horizontal beam size. A simulation of this 'streak' effect is shown in **Figure 7.68**, for nominal quadrupole settings. In addition to slice emittance, the horizontal Twiss parameter variations along the bunch length can also be measured. Of course, the absolute bunch length and temporal profile can also be measured here.

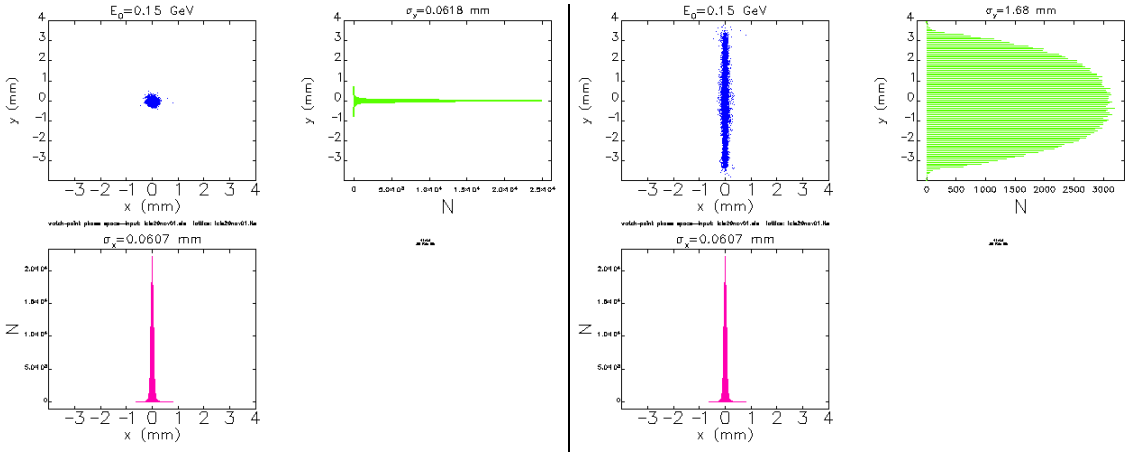

Figure 7.68 Simulated profile monitor in middle of ED0 emittance diagnostic section with 55-cm rf deflector OFF (left) and with voltage set to 1 MV (right). The deflector 'streaks' the beam vertically such that the horizontal slice emittance can easily be measured.

7.8.2.2 RF Zero-Phasing Technique

Beyond the rf-deflectors, CSR detectors will be used as relative bunch length monitors, calibrated using a streak camera for the 10-psec range, and calibrated using the rf-deflector, or a "zero-phasing technique" [50] for the 2-psec and 0.2-psec ranges.

The zero-phasing technique is another way to measure the micro-bunch in an absolute sense, by employing an accelerating rf system at zero-crossing angle to generate correlated energy spread. The transverse beam size is measured in a dispersive region to extract the bunch length. In the LCLS, the entire L3-linac is used as the rf system. The measurement is invasive and performed infrequently to calibrate or crosscheck the CSR detectors. The micro-bunch is transported to the energy spread measuring profile monitor in DL2 (PR31) with a +90° L3 rf phase (i.e., zero crossing producing no acceleration in L3). The measurement is then repeated at a –90° rf phase. The bunch length is then given by the average of the two energy-spread values.

$$\sigma_z \approx \frac{\lambda}{4\pi}\frac{E_i}{E_f - E_i}\left(\sigma_{\delta_1} + \sigma_{\delta_2}\right) \qquad \textbf{(7.28)}$$

Here λ is the rf wavelength (105 mm), E_i is the L3 injection energy (4.54 GeV), E_f is the L3 final energy obtained with the L3 rf phase at crest-phase (14.6 GeV), and σ_{δ_1} and σ_{δ_2} are the two energy spread measurements at +90° and –90°.

This method is simulated in **Figure 7.69**, including CSR and wakefields, and demonstrates an absolute bunch length measurement with an accuracy of a few percent. In all cases shown the beam is not accelerated in L3-linac, for a final beam energy of 4.54 GeV. The 75-μm FWHM bunch length generates FWHM energy spread values of 1.64% (at $\varphi = -90°$, left) and 0.333% (at $\varphi = +90°$, right). When this is used in **Eq. (7.28)**, it reproduces the 75-μm FWHM bunch length to within a few percent. Statistical resolution is dependent on the profile monitor used and should be 5–10%. The horizontal FWHM beam size at the DL2 energy spread profile monitor (PR31; $\eta_x \approx 50$ mm) associated with the three cases is shown at bottom of **Figure 7.69**. Relative bunch length monitors are then calibrated from this, or the rf-deflector measurements. With BC2 switched off, the bunch length after BC1 can also be measured with either of these techniques.

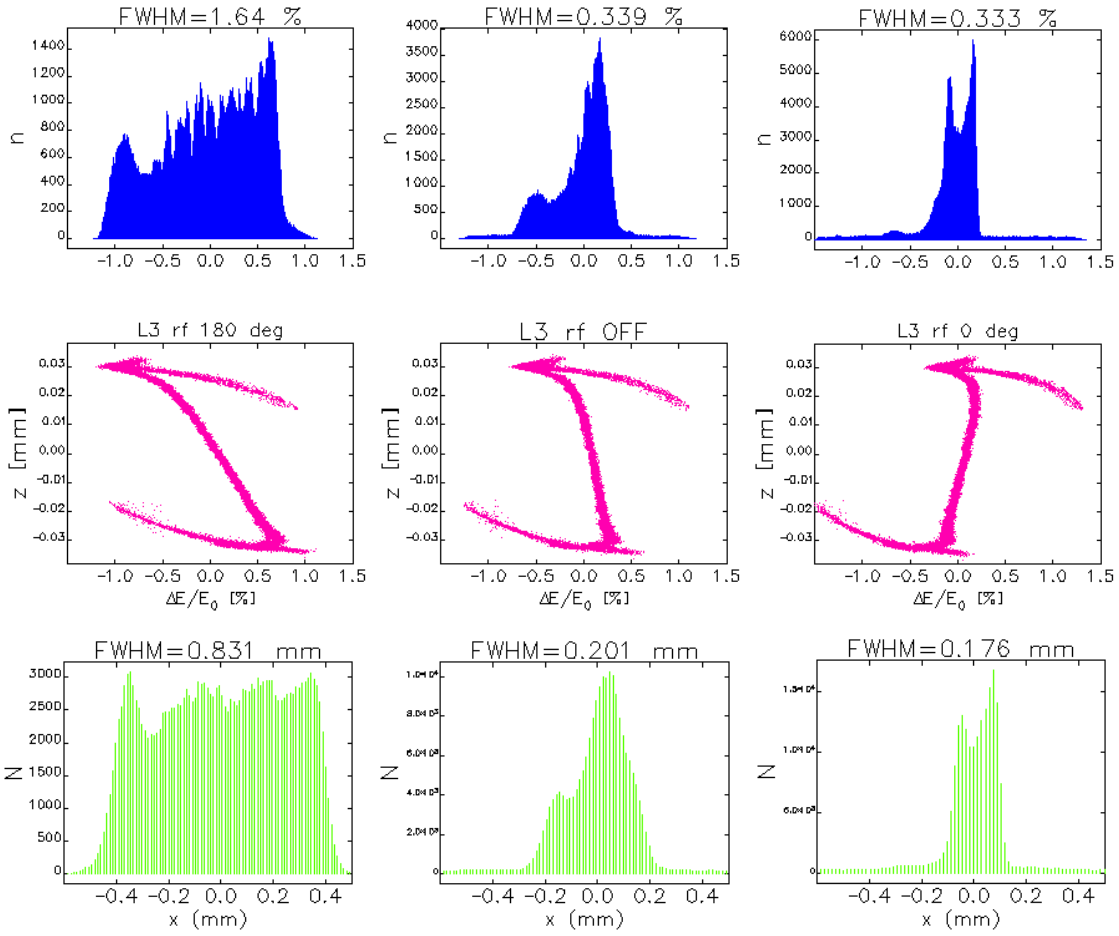

Figure 7.69 Simulated 'zero-phasing' technique for bunch length measurement. Top row is energy distribution after DL2 at 4.54 GeV for −90° (left), rf-off (center), and +90° (right) in L3. Middle row is longitudinal phase space, and bottom row is horizontal beam profile.

7.8.2.3 Electo-Optical Bunch Length Diagnostic

An electro-optical (EO) device will also be employed as a bunch length and bunch arrival-time diagnostic [51]. The concept, as illustrated in **Figure 7.70**, shows a laser pulse with a chirped waveform co-propagating with the electron beam. The active element is a thin (~100 μm) electro-optic crystal such as $LiNbO_3$ through which the pulse propagates. The transmission of

portions of this laser probe is determined according to the dynamic phase retardation induced by the electric field from the electron bunch. Any transmission attributed to intrinsic (static) phase retardation (i.e., without an electron bunch) is cancelled using a pair of polarizers with a biasing optical compensator. Polarizers are positioned up- and down-stream of the electro-optic crystal and are cross-polarized relative to each other. The electric field of the electron bunch modulates the transmitted intensity of the laser pulse in the following way. The short-lived bunch field induces a birefringence that generates phase retardation in the laser pulse. Consequently a polarization component orthogonal to that of the incident pulse can be transmitted to a spectrometer during a 'gated' time interval. The temporal structure of the bunch-induced modulation can come from knowledge of the initial wavelength chirp on the laser waveform. A spectrometer, in this case part of a Frequency Resolved Optical Gating (FROG) device, is used to measure which part of the band has been 'gated' by the electron bunch.

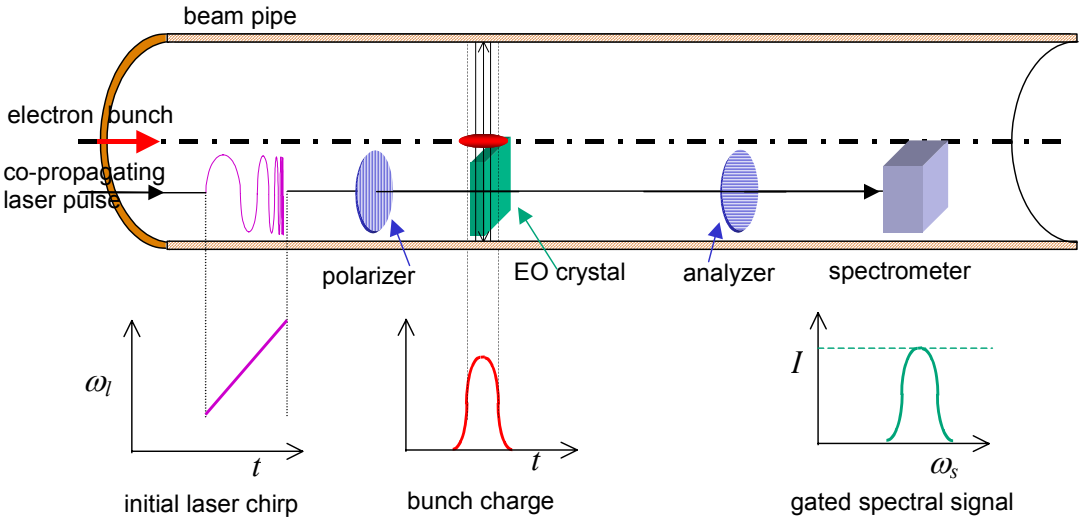

Figure 7.70. The principal of measurement of the electron bunch length by modulation of a chirped laser pulse in an electro-optic crystal by the electric field of the bunch. In practice only the EO crystal is in vacuum. All other optical components are located outside a window.

In order for the FROG to adequately record transmission of a single laser pulse from a single electron bunch a photon flux of 10 μJ is required in the gated spectral signal. This translates into a peak power requirement of ~200 MW. The chirped laser waveform is stretched to a 10-ps duration (thereby allowing up to 10 ps of relative timing jitter between laser and beam). The high peak power and proportionately wide laser bandwidth requirements can be met with a Ti:Sapphire laser oscillator seeding a regenerative amplifier. The extent of the waveform chirp is limited by the pulse bandwidth which can exceed 10 nm. At this high peak power, care is required to remain below the fluence damage threshold near the 1-J·cm^{-2} level in the optical materials. The co-propagating geometry is chosen since a transverse light propagation geometry would require focusing the laser light to micron level spot sizes in the EO crystal in order to preserve temporal resolution. This would exceed damage thresholds by several orders of magnitude. One constraint on the co-propagating geometry is the relative slippage between the

photons slowed down in the crystal and the electric field of the bunch propagating at a velocity equal to *c*. A thin crystal with a low refractive index is therefore appropriate. The extremely high electric field strengths of several GV/m from the 15-GeV, 1-nC LCLS bunch will afford use of EO crystals with 100-μm thickness and relatively low electro-optic coefficients. For comparison quartz has an EO coefficient as low as 0.2×10^{-12} V/m with a refractive index of $n = 1.5$ compared to a more usual EO material such as $LiNbO_3$ with a coefficient of 30×10^{-12} V/m and $n = 2.3$. It is envisaged that such an electro-optic measurement station will be installed in the DL2 beamline to measure the electron bunch length characteristics before it enters the undulator.

7.8.3 Beam Energy Spread Diagnostics

7.8.3.1 DL1 Energy Spread Diagnostics

The energy spread measurement in DL1 is made with a single profile monitor (OTR monitor) located between the two dipoles of DL1 at the point where the horizontal dispersion function reaches a value of $\eta_x \approx -153$ mm with a horizontal beta function of $\beta_x \approx 0.79$ m (at $S \approx 18.5$ m in **Figure 7.33**). For the nominal emittance and nominal energy spread of $\sigma_\delta \approx 0.10\%$ at 150 MeV, the betatron beam size is 52 μm, but the dispersive size is 153 μm. This produces a systematic energy spread measurement error of 6%. The statistical error depends on the profile monitor and should be 5–10%.

7.8.3.2 BC1 Energy Spread Diagnostics

The energy-spread measurement in BC1 is made with a profile monitor (phosphor) located in the center of the chicane at a point where the horizontal dispersion function is $\eta_x \approx 228$ mm and the horizontal beta function converges towards a minimum of $\beta_x \approx 6.5$ m (at $S \approx 34.8$ m in **Figure 7.19**). For the nominal emittance and nominal energy spread of $\sigma_\delta \approx 1.78\%$ at 250 MeV, the betatron beam size is 115 μm, but the dispersive size is 4.1 mm. This produces no systematic error in the energy-spread measurement. The collimator jaws in BC1, upstream of the profile monitor, can be used to select energy bands for diagnostic purposes.

7.8.3.3 BC2 Energy Spread Diagnostics

The energy-spread measurement in BC2 is also made with a single profile monitor (phosphor) located in the center of the first chicane at a point where the horizontal dispersion function is $\eta_x \approx 341$ mm and the beta function converges towards a minimum of $\beta_x \approx 25$ m (at $S \approx 411$ m in **Figure 7.26**). For the nominal emittance and nominal energy spread of $\sigma_\delta \approx 0.76\%$ at 4.54 GeV, the betatron beam size is 53 μm, but the dispersive size is 2.6 mm. As in the case of BC1, this produces no systematic error in the energy-spread measurement. As in BC1, the collimator jaws in BC2, upstream of the profile monitor, can also be used for diagnostic purposes.

7.8.3.4 DL2 Energy Spread Diagnostics

The energy spread measurement in DL2 is made with a profile monitor (a retractable OTR monitor) located where the dispersion function is $\eta_x \approx 91$ mm and the beta function converges towards a minimum of $\beta_x \approx 4.0$ m (at $S \approx 1236$ m in **Figure 7.36**). For the nominal emittance and a core rms energy spread of $\sigma_\delta \approx 0.03\%$, the betatron beam size is 12 μm, but the dispersive size

is 27 μm. The total beam size is then 30 μm, and a horizontal profile monitor produces an energy spread measurement accuracy of 10% at 14.35 GeV. Of course, the betatron beam size can always be subtracted in quadrature if the emittance and beta function are known.

7.8.4 Trajectory and Energy Monitors with Feedback Systems

7.8.4.1 Trajectory Feedback Systems

Trajectory feedback systems will be placed at the entrance of the L2-linac, the L3-linac and at the undulator entrance. As at the SLC [52], these systems will each be composed of approximately ten BPMs which record both *x* and *y* positions, preceded by a set of two horizontal and two vertical fast dipole corrector magnets controlled by a microprocessor based cascaded feedback system. The cascade algorithm isolates each feedback system such that the systems do not all respond to the same trajectory changes.

In order to control transverse orbit variations to better than $1/10^{th}$ of the beam size, the individual one-pulse BPM resolution for the three 10-BPM feedback systems described above needs to be 50 μm, 20 μm and 10 μm rms, respectively (decreasing with increasing energy). Trajectory variations which occur at frequencies below ~10 Hz will be stabilized. Faster variations cannot be damped significantly and will need to be identified at the source. Additional trajectory control systems (e.g., in the L0-linac) are addressed in **Chapter 6**.

Transverse vibrations of quadrupole magnets will generate orbit variations, which if fast enough will not be damped by feedback systems. Tolerance calculations in L2 (strongest quadrupole gradients) indicate that uncorrelated random vibrations of all 28 L2 quadrupoles at the level of 400 nm rms will generate orbit centroid fluctuations in the undulator, which are 6% of the beam size there (6% of 30 μm). Measurements in the SLC indicate that existing linac magnet vibrations are <250 nm [53] with the highest frequency content at 59 Hz and 10 Hz driven by cooling water. These observed vibrations are small enough to limit undulator orbit centroid jitter to below the goal of <20% of nominal beam size. At lower energies in L1 and BC1, most of the new quadrupole magnets are air-cooled.

7.8.4.2 Energy Feedback Systems

Energy feedback systems will be placed in each bending region (DL1, BC1, BC2, and DL2). A single BPM or group of BPMs placed at a high dispersion point will be used to determine energy variations, and upstream rf will be used to stabilize the energy. A group of klystron phases will be used to control the energy while maintaining the correlated energy spread such that bunch compression in each system is also held constant. Similar systems, but without the bunch length control aspect, have been successfully tested at the SLC [54].

DL1 Feedback

The DL1 Energy Feedback System consists of at least 3 BPMs—two placed near the QM02 and QM04 quadrupoles, and a third near QB (see **Figure 7.33**). With this simple system energy variations can be distinguished from betatron oscillations using a linear combination of the three BPMs. The large dispersion at the QB BPM (153 mm) produces a relative energy resolution at

150 MeV of $\delta < 1.5\times10^{-4}$ with a 20-μm resolution BPM, which is almost ten times better than needed (see **Table 7.5**). The energy can be maintained by controlling the output power of one of the two L0 klystrons, which would need to run in an unsaturated configuration. The fast, pulse-to-pulse voltage stability of this unsaturated klystron will, however, still need to be <0.1% rms.

BC1 Feedback

The BC1 Energy Feedback System consists of one BPM—one placed at the center of the chicane (see **Figure 7.19**). The large nominal dispersion in the chicane (228 mm) should produce a relative energy resolution of $\delta \approx 9\times10^{-5}$ with a 20-μm resolution BPMs, which is four times better than needed (see **Table 7.5**). To allow voltage control, the single klystron powering L1 will not be operated in saturation. The fast, pulse-to-pulse voltage stability of this unsaturated klystron will, however, still need to be <0.1% rms. Similarly, the rf phase of L1 will be controlled with a feedback system which maintains a relative bunch length measurement (based on CSR or a resonant cavity) after BC1. Fast energy stabilization using the BPMs and L1 rf voltage at <10 Hz opens the L1 phase tolerance by a factor of three compared with that required with no energy stabilization (i.e., ~0.3˚ rather than 0.1˚ rms — see footnotes of **Table 7.4**). Therefore, the bunch length monitor will provide rf phase feedback but at a much slower rate of <1 Hz.

BC2 Feedback

The BC2 Energy Feedback System is identical to that of BC1 and consists of one BPM at the center of the BC2 chicane. The large nominal dispersion in the chicane (341 mm) should produce a relative energy resolution of $\delta \approx 1.2\times10^{-4}$ with a 40-μm resolution BPMs, which is five times better than the minimum required. To maintain the energy in BC2, one of the 28 klystrons near the end of L2 will be nominally set at ½-voltage (¼-power) and at a crest phase. This voltage-controlled klystron will be at the high-energy end of L2, at 24-5 or 24-6, to reduce the effects on the focusing strength. With respect to the nominal parameters described in **Table 7.1**, the phasing of the remaining 27 powered klystrons needs to be adjusted from −42.8˚ to −43.3˚ and the rf voltage per klystron raised by 2%. The power level of this one klystron will be controlled by the BPM-based energy feedback system at a rate of <10 Hz. The dynamic range for one klystron with ±120 MeV adjustability is then ±2.6% of beam energy at BC2. Larger, manual changes will be implemented by switching on or off spare klystrons. The measured bunch length is held constant by adjusting the rf phase of the last sector or two (23-24) at a slower rate ~1 Hz. A full study of this feedback system has not yet been performed.

DL2 Feedback

The DL2 Energy Feedback System consists of 2 BPMs—one placed at QL32 and another at QL38 (see **Figure 7.36**). Since the 2×2 transfer matrix between these quadrupoles is +**I**, differencing these two x BPM readings will cancel any betatron signal leaving only the energy signal. The large nominal dispersion at the two BPMs (103 mm) produces a relative energy resolution of $\delta \approx 7\times10^{-5}$ with two 10-μm resolution BPMs. This high-resolution relative energy signal may also be useful to the downstream x-ray experiments in order to monitor the fluctuations in the x-ray wavelength. The final bunch length is insensitive to L3 rf phase or voltage, so only the beam energy needs to be well controlled here. Two klystrons in sector-30 at

½-voltage (¼-power) and crest-phase can be used to control the beam energy in DL2. A dynamic range of ±1.7% is then possible. Larger, manual changes can be implemented by switching on or off spare klystrons. The rf phase then only needs to be held constant to a level of a few degrees. This might be done by occasional phase scanning using the BPMs in DL2 to check the beam phase.

In all cases above, the energy resolution is more than adequate to drive feedback systems for stabilization of the compression systems (see **Table 7.5**). The remaining critical items, which need further study, are the resolution and time characteristics of the CSR- or cavity-based bunch length monitors.

7.9 The Wake Functions for the SLAC Linac

7.9.1 Introduction

Obtaining wake functions for the SLAC linac structure that are sufficiently accurate to be used in beam dynamics studies for bunches as short as 20 μm (rms) is not an easy task. It requires an accurate knowledge of the impedance of the structure over a large frequency range, which is difficult to obtain both by means of frequency-domain and time-domain calculations. Direct time-domain integration, using a computer program such as the MAFIA module T2 [55], needs a very large mesh and hence prohibitive amounts of computer time. Even then, errors will tend to accumulate in the results. The approach actually employed, uses a frequency-domain calculation applied to a simplified model of the linac structure, an approach that also has its difficulties. The wake functions obtained are the wakefields excited by a point charge, as a function of distance behind that charge. By performing a convolution over the bunch, the wakefields left by a bunch of arbitrary shape can be obtained.

A SLAC structure is 3 m long; it consists of 84 cells. It is a constant gradient structure, and both the cavity radius and the iris radius gradually become smaller (the change in iris radius is 0.5%/cell) along the length of each structure. In our calculations each SLAC constant gradient structure is broken into five pieces. Each piece is represented by a periodic model with an average iris radius, and the rounded iris profiles are replaced by rectangular ones. The wakefields for the five models are obtained and then averaged to obtain wake functions to represent an entire structure. Questions as to the accuracy and applicability of the calculated wake functions concern primarily:

- The accuracy of the periodic calculations themselves,
- Transient effects and effects at the ends of a structure,
- The fact that the irises vary in the real structure,
- The effects of resistivity/roughness of the iris surface.

7.9.2 The Calculated Wakefields for the SLAC Linac

The wakefields for the SLAC linac structure were first calculated many years ago [56]. The methods and results presented here are essentially the same, though there are some changes in the details (see, for details, where these methods are applied to the NLC X-band structure [57] and the SBLC S-band structure [58]). To obtain the wakefields for each of the representative periodic models, several hundred mode frequencies and loss factors are obtained using computer programs that employ mode-matching techniques. The accuracy of these calculations is not easy to assess. The density of modes obtained is one consistency check, and good agreement is found.

The high-frequency contribution to the impedances is obtained employing the so-called "Sessler-Vainsteyn optical resonator model" [57,59]. It is a simple model that combines the Poynting flux at the iris due to the beam with the diffraction due to light at the edges of a periodic array of circular mirrors. It yields the expected high-frequency dependence of the impedance; e.g., the real part of the longitudinal impedance varies with frequency as $\omega^{-3/2}$. **Figure 7.71** shows the real part of the longitudinal impedance, averaged over frequency bins, for the geometry of cell 45 (a in the plot is the iris radius; 11.6 mm). The dashed curve is the Sessler-Vainsteyn prediction. At the higher frequencies the agreement is seen to be quite good.

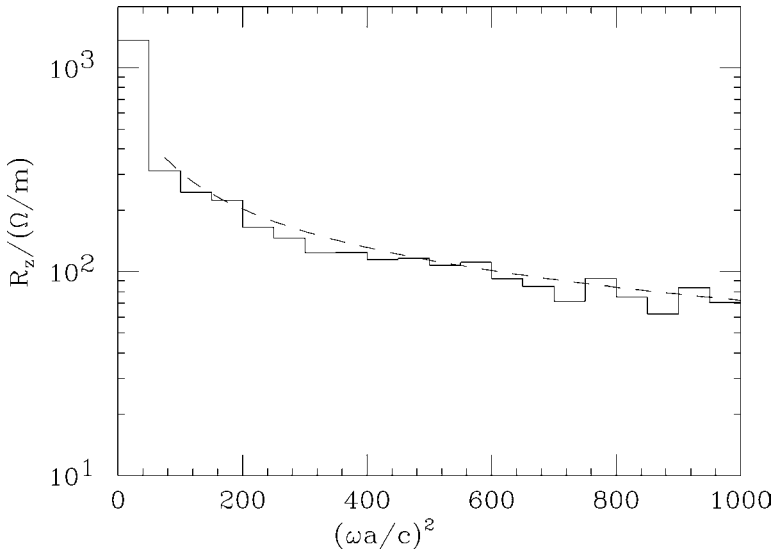

Figure 7.71 The real part of the longitudinal impedance, averaged over frequency bins, for the geometry of cell 45. The Sessler-Vainsteyn prediction is given by the dashed curve.

As a dipole example, the real part of the longitudinal dipole impedance, averaged over frequency bins, for the geometry of cell 45 is plotted in **Figure 7.72**, with the dashed curve again giving the Sessler-Vainsteyn prediction. There appears to be a 15% systematic difference between the two results at high frequencies, probably due to the approximate nature of the Sessler-Vainsteyn model. The agreement, however, is acceptable for our requirements.

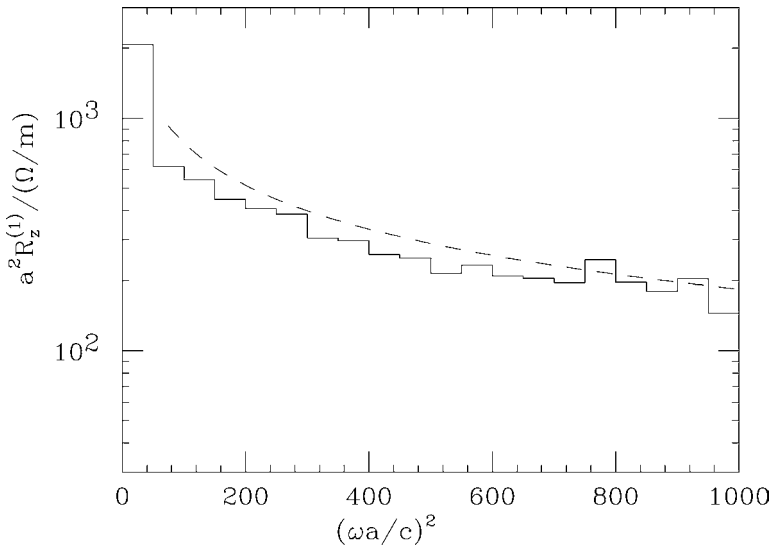

Figure 7.72 The real part of the longitudinal dipole impedance, averaged over frequency bins, for geometry of cell 45. The Sessler-Vainsteyn prediction is given by dashed curve.

The longitudinal wakefield of the 5 representative cells—cells 1, 23, 45, 65, and 84—is given in **Figure 7.73**, and the average (with the end cells weighted by one half), representing the whole structure, is given by the dashes.

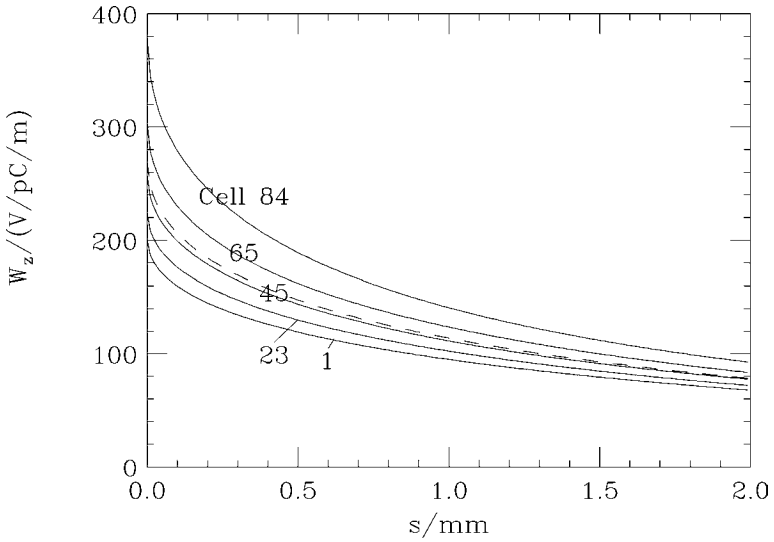

Figure 7.73 The longitudinal wakefield of representative cells in the SLAC structure (solid curves). The average represents the whole structure (the dashes).

One important consistency check is that for each model structure, the longitudinal wakefield at the origin must satisfy [60]

$$W_{\parallel}(0) = \frac{Z_0 c}{\pi a^2} \ , \qquad \textbf{(7.29)}$$

with $Z_0 \approx 377\ \Omega$ and a the iris radius. In all cases the computed values are low, but in no case by more than 4%. Similarly, the transverse wakefield of the representative cells is given in **Figure 7.74**, and the average, again representing the whole structure, is given by the dashes. The transverse wakefield of the representative cells must satisfy **Eq. (7.30)** [57]. In all cases the agreement is within 1-2%.

$$\frac{d}{ds}W_{\perp}(0) = \frac{2Z_0 c}{\pi a^4} \tag{7.30}$$

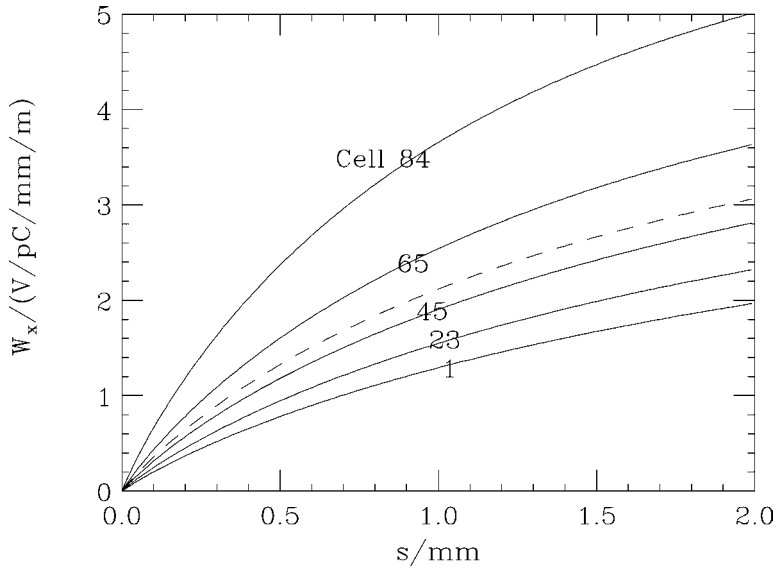

Figure 7.74 The transverse (dipole) wakefield of representative cells in the SLAC structure (solid curves). The average represents the whole structure (the dashes).

7.9.3 Discussion

The calculated wakefields are asymptotic in that they apply only after the beam has traversed a critical number of cells N_{crit}. For a gaussian bunch, for the total loss obtained using only the asymptotic wake functions to be within a few percent of the loss when transient effects are also included, requires that [58]

$$N_{\text{crit}} = \frac{\alpha a^2}{p\,\sigma_z} \tag{7.31}$$

with $\alpha \geq 0.5$, p the structure cell length, and σ_z the bunch length. The transient region is largest for short bunches. In the LCLS the bunch is shortest after the second bunch compressor where $\sigma_z \approx 22\ \mu$m. Taking, in addition, a = 1 cm and p = 3.5 cm, then $N_{\text{crit}} \approx 70$, which represents about 80% of the length of one structure or 0.5% of the length of the third linac. In most of the SLAC linac the 3-m structures are combined in groups of four, with nearly no extra space in between them; the groups of four are separated by about 20-cm of beam tube, and every 100 m there is an extra 4 m of beam tube. With this arrangement, after the end of the structures, the wakefields generated by the beam do not have a chance to return to their initial conditions, except partially at

the 3% of the structures that follow the 4 m gaps. Therefore, using the asymptotic wakefields to represent the entire SLAC linac, and ignoring the transient effects, should result in very little error even for a 20-μm bunch.

There are three other effects that can be important for short bunches: (1) The so-called "catch-up distance" effect: If the head of the beam generates a wakefield at a certain position in the linac, due to causality the tail does not feel the effect until a distance $\sim 0.5 a^2/\sigma_z$, which in this case is 2.5 m, later. Since this is a small fraction of the 550-meters of accelerating structure after the second compressor, this effect should not be important. (2) For $\sigma_z \leq a/\gamma$, which in this case is 0.3 μm, the impedance drops dramatically. Since the minimum bunch length is 20 μm, this effect should also not be important for the LCLS. (3) The effect of the resistivity of the iris surface is shown, in the following section, not to be a significant effect for the LCLS accelerator.

Finally, it should be noted that the above estimates all assume that the bunch is gaussian, which it is not. The real bunch shape is rectangular with spikes at the edges of the distribution (see bottom of **Figure 7.7**). The Fourier transform of such a bunch shape reaches to higher frequencies than the gaussian approximation, and therefore the short bunch effects will become somewhat more pronounced than estimated above. However, even with this consideration, the calculated wake functions will accurately represent the wakefield effects in the linac for the LCLS project.

7.9.4 Confirmations

There have been confirmations, both theoretical and by measurement, of the calculated SLAC wake functions and, more recently, of the similarly calculated wake functions for the NLC and the DESY-SBLC linac. All of the measurements, however, have been done for bunch lengths significantly larger than the 20-μm of interest here. As to theoretical comparisons, the calculated SLAC wake functions have been confirmed, for gaussian bunches down to $\sigma_z \approx 0.5$ mm, using the time domain program TBCI [61]. A time domain program exists that is able to obtain accurate results for short bunches in accelerating structures [62]. For a 100-μm bunch in the NLC structure, the results of this program, as well as the results of an independent frequency domain program [63], agree with our frequency domain results to within a few percent.

As to confirmation by measurement in the SLC linac, the total wakefield-induced energy loss [64] and more recently the wakefield-induced voltage of a bunch [65], [66] have been shown to agree quite well, for bunch lengths down to 0.5 mm. Also, in the ASSET test facility, the short range transverse wakefield of a 0.5-mm bunch in the NLC structure has been measured, and the results agree quite well with the calculated results [67].

7.9.5 Resistive Wall Wakefields

In addition to geometric wakefields, the micro-bunch beyond BC2 experiences a longitudinal resistive wall (RW) wakefield which introduces a small coherent energy spread along the bunch [68], [70]. For a bunch which is much longer then the characteristic length, s_0,

$$s_0 \equiv \left(\frac{2a^2}{Z_0\sigma}\right)^{1/3}, \tag{7.32}$$

the rms relative energy spread induced in a smooth cylindrical chamber of radius, a, and conductivity, σ, is

$$\sigma_{\delta_{\mathrm{RW}}} \approx (0.22)\frac{e^2 cNL}{\pi^2 a E \sigma_z^{3/2}}\sqrt{\frac{Z_0}{\sigma}}\ . \tag{7.33}$$

This is for a gaussian bunch, which is long compared to s_0. To more accurately estimate the RW energy spread generated after BC2, the beamline is broken into two discrete sections of significantly small radius (**Table 7.24**). Remaining sections have much larger radii (40–400 mm) and are ignored here. The short iris surfaces of the copper accelerating structures in L3 contribute no significant component to the resistive wall wakefields [69].

Table 7.24 The two main beamline sections that transport the micro-bunch and contribute to a resistive wall wake energy spread generated between BC2 and undulator entrance.

Beamline Section	Material	Conductivity	Radius	Length	s_0
		Ω^{-1}-m^{-1}	mm	m	μm
Linac-3 non-accelerating chambers	Stainless Steel	0.14×10^7	12.7	76	85
Linac-to-undulator beamline	Aluminum	3.6×10^7	12.7	106	29

The 76-meters of 1-inch diameter stainless steel are distributed along Linac-3 as quadrupole/BPM chambers, and other short non-accelerating sections including 22 meters beyond sector-30 in the beam switchyard, before the aperture significantly increases. The aluminum sections are new chambers for the DL2/ED2 beamline leading up to the undulator entrance, which follow the large radius beam switchyard. The replacement of the existing 100 meters of stainless chamber, which is presently used in the undulator hall, with aluminum removes an effect which would otherwise increase the coherent energy spread by 0.05% rms, with an energy gradient which is nearly linear across the bunch. The associated transverse resistive-wall wakefields are insignificant for reasonable electron trajectories.

For these sections, the bunch (22 μm) is shorter than s_0, so the RW energy spread of the short-bunch ($\sigma_z/s_0 < 1$) is calculated using the point-charge wake function [70],

$$E_z(s) = -\frac{4qcZ_0}{\pi a^2}\left(\frac{1}{3}e^{-s/s_0}\cos\frac{\sqrt{3}s}{s_0} - \frac{\sqrt{2}}{\pi}\int_0^\infty \frac{dx\, x^2 e^{-x^2 s/s_0}}{x^6+8}\right), \tag{7.34}$$

which is convoluted with the bunch distribution similar to that at bottom of **Figure 7.7**. This estimate ignores the frequency dependence of the conductivity, an effect which is quite small. The results for each of the two sections of **Table 7.24** are shown in **Figure 7.75**.

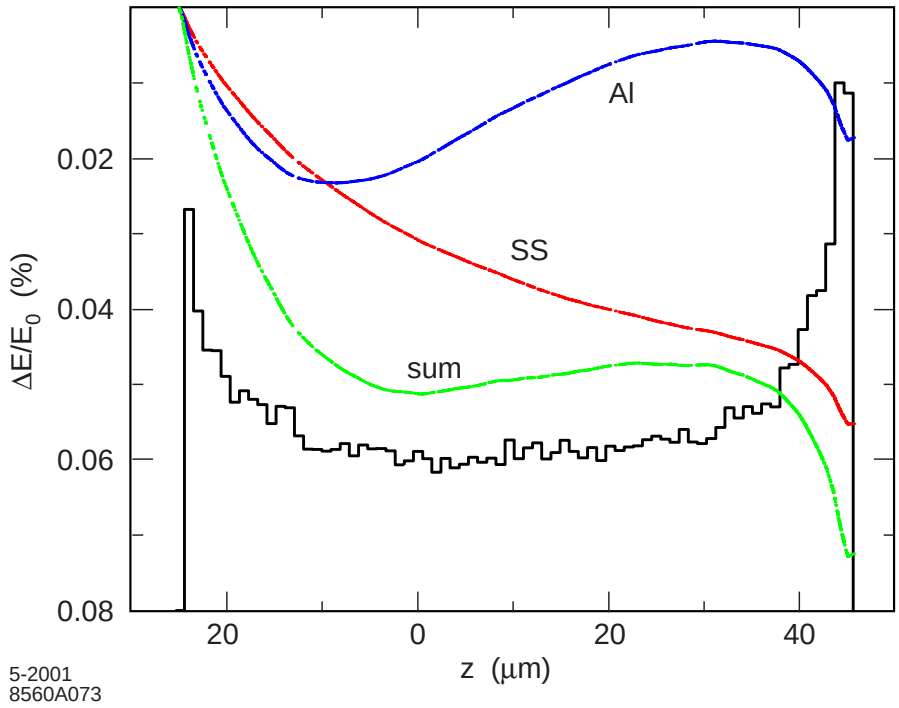

Figure 7.75 Resistive wake of 1-nC bunch after convolution with the temporal bunch distribution (solid/black, arbitrary vertical scale) at bottom of **Figure 7.7**. The contributions, and their sum, are labeled.

For this bunch distribution (shown on arbitrary vertical scale as solid curve in the figure), the total rms RW energy spread generated by both sections is 0.015% (with respect to the mean), which is well below the maximum chirp tolerance (~0.1% rms). If the linear component of the energy spread is removed (by a small rf phase change in L2), this is reduced to 0.009%. This energy spread is, of course, a gradient along the bunch and has almost no effect on the slice energy spread. The longitudinal resistive-wall wakefields prior to the undulator are therefore, very small, but are included in all of the 2D and 6D tracking.

7.10 Parts List and Installation Issues

7.10.1 Parts List

A list of LCLS magnet power supplies is given in **Table 7.25** with each supply designated as new, existing, or recycled (re-used from a previous SLAC installation).

A list of new, existing, and recycled BPMs (beam position monitors) located throughout the LCLS accelerator is given in **Table 7.26**. Just 19 new BPM stripline monitors are needed in the tunnel, the rest are recycled from the FFTB or are already located in the existing beamline. The several new BPMs needed in the L0-linac are not included here (see **Chapter 6**). The required rms BPM resolution at a minimum bunch charge of 0.2 nC is also estimated in the table. Most LCLS BPMs, with the exception of chicane locations, are suitable with a chamber ID of ~2.5 cm.

Table 7.25 Power supply and magnet list for the LCLS accelerator (not including injector).

Magnet String Location	Existing, New or Recycled	No. of Power Supplies	Magnets per Supply	Uni- or Bi-polar	Magnet Type	Max. Current [A]	Max. Voltage [V]	Est. Reg. Tolerance [%]
DL1	N	1	2	U	5D7.1	450	10	0.02
BC1	N	1	4	U	5D7.1	400	20	0.02
BC2	N	1	4	U	1D15.7	~1000	?	0.05
DL2	N	1	4	U	4D102.36T	375	40	0.02
DL2	N	1	2	U	VB	?	?	0.05
DL1/BC1	N	12	1	B	1Q5.6	12	36	0.1
L1/BC1	N	4	1	B	QA	8	5	0.1
L2/L3	E	69	1	U	QE	20	?	0.1
BC1	N	3	1	U	QE	25	2	0.1
L2/L3	N	6	8	U	QE	25	?	0.1
L2	N	1	5	U	QE	25	?	0.1
BC2	N	4	1	U	QE	200	20	0.1
BC2	N	2	1	B	QE	12	1	0.1
BSY	E	1	3	U	50Q1,2,3	310	?	0.1
BSY	E	1	1	U	QSM	9.8	?	0.1
DL2	E	3	1	U	0.91Q17.7	240	?	0.05
DL2	R	2	4	U	0.91Q17.7	250	120	0.05
DL2	R	2	2	U	0.91Q17.7	250	60	0.05
DL2	R	9	1	U	0.91Q17.7	250	30	0.05
DL2	R	1	6	U	0.91Q17.7	100	80	0.05

A list of LCLS profile monitors is given in **Table 7.27**. This list does not include monitors placed upstream of the end of the L0-linac. The profile monitors are wire-scanners, OTR monitors (or both in a few cases), or phosphor screens. Wire-scanners allow non-invasive, but integrated pulse measurements, while screens allow single shot measurements, which are destructive. The phosphor screens are used where the beam size is large and diffuse in BC1 and BC2. The profile monitors are used to measure transverse emittance (ε), energy spread (δ), or bunch length (σ_z), as indicated in the table. The rms transverse beam size listed, $\sigma_{x,y}$, is the x ($\approx y$) size in the case of emittance measurements, the x size in the case of energy spread, and the y size in the case of bunch length. Beam size measurement resolution of $\leq$10% is required with a charge level as low as 0.2 nC per bunch.

Table 7.26 BPM list (not including injector or L0). Estimated rms resolution is based on a minimum operable bunch charge of 0.2 nC. Just 19 new BPM strip-lines are required.

Accelerator Area	Location Range, S [m]	Existing, New or Recycled	Quantity	Est. Resolution [μm]
DL1/ED0	0-21	**N**	**11**	25
L1-linac	21-31	**N**	**2**	20
L1-linac	30	E	1	20
BC1	31-46	**N**	**5**	20
BC1/ED1	43	E	1	20
L2-linac	46-397	E	28	10
BC2	397-423	**N**	**1**	10
L3-linac/BSY	423-1200	E	58	10
DL2/ED2	1200-1280	R	28	5

Table 7.27 Profile monitor list with nominal rms beam sizes for $\gamma\varepsilon$ = 1 μm (not including injector system).

Accelerator Area	Location, S, [m]	Monitor Type	Measures ε, δ or σ_z	Quantity	Energy [GeV]	Beam Size, $\sigma_{x,y}$ [μm]
DL1/ED0	10-15	wire/OTR	ε	3	0.15	65-130
DL1	16.5	OTR	δ	1	0.15	135
BC1	32.6	Phos.	δ	1	0.25	1740
BC1/ED1	39.8	Wire	ε	3	0.25	40-80
L2-linac	359-397	Wire	ε	4	4.1-4.5	41-72
BC2	404	Phos.	δ	1	4.5	1560
L2-linac	524	OTR	σ_z	1	4.5-6.2	250
L3-linac	701-815	Wire	ε	4	4.5-11	39-57
DL2	1218	OTR	δ-slice	1	4.5-15	20
DL2	1237	OTR	δ	1	4.5-15	38
DL2/ED2	1252-1270	wire/OTR	ε	4	4.5-15	17

7.10.2 Installation Issues

Some of the necessary rf modifications to the SLAC linac are listed in **Table 7.28**. Some accelerating structures must be removed in order to locate compressor chicanes and matching sections. And in one case, a new 3-meter structure can be added back to the linac (the extinct NPI gun located at 25-1c).

Table 7.28 Summary of modified, removed or added S-band rf sections for the LCLS design. The energy loss quoted here assumes that the rf power inputs are re-configured.

Linac section	reason for modification	net ΔL removed/added [m]	net energy loss [MeV]
21-1b,c	shorten sections for L1 quads	−0.35	−8
21-2a,b,c,d	remove for BC1 chicane and X-band	−12.2	−235
21-3a	remove for ED1 emittance diagnostic	−3.0	−34
24-3d,4d,5d	remove to add L2-ED profile monitors	−9.1	−103
24-7a,b,c,d	remove for BC2 chicane	−12.2	−235
24-8a,b,c,d	remove for BC2 chicane	−12.2	−235
25-1c	replace missing 3-m section (NPI)	+3.0	+34
25-5a	remove to add transverse rf deflector	−3.0	−34
27-6d	remove to add L3-ED profile monitors	−3.0	−34
total =	—	**−52.1**	**−885**

7.11 Operational Issues

The LCLS will operate at 120 Hz concurrent with PEP-II B-Factory operations. An electron beam can be accelerated through the entire SLAC linac to 50 GeV by switching off and straightening the bunch compressor chicanes, or by providing adequate aperture in the chicane bends. This second option, however, compromises the ability to provide a high-resolution BPM in the center of the chicane, which is a critical requirement for the bunch length and energy feedback systems.

With the chicanes switched off, the DL1 bends are also switched off, as are the other dedicated LCLS focusing magnets in the L1 and BC1 area. This re-configuration will require a switching time on the order of a few minutes at best. The possibility of fast, pulse-to-pulse switching between LCLS and 30-GeV electrons in the end-station can probably only be realized by building a by-pass beamline from sector-21 to sector-30, as is done in the PEP-II injection scenario.

A fast-pulsed kicker in the beam switchyard, just downstream of the linac and well before the undulator, should be installed in order to dump the electron beam during conditions of exceptionally poor beam quality. This will help to preserve the permanent magnet undulator fields, and to provide a 'veto' for unwanted pulses. It will also allow more invasive tuning with the electron beam passing through the bulk of the accelerator. The kicker will, of course, only be fast enough to dump the *next* pulse(s), after detection of a poor beam-quality trigger. Beam collimators just upstream of the undulator will provide protection from the first poor-quality pulse. Such poor quality conditions can be produced by klystron trips (especially in L1 or L2), the firing of the transverse rf deflector in sector-25, or any number of previously determined

beam quality conditions. Such a kicker magnet, its power supply, and the beam dump are all presently available by recycling one of the SLC "single-beam-dumper" systems located in the beam switchyard.

7.12 References

1 P. Emma, "LCLS Accelerator Parameters and Tolerances for Low Charge Operations", *LCLS-TN-99-03*, May 1999.

2 V. Bharadwaj, et al, "LCLS II Design", *LCLS-TN-00-11*, October 1998.

3 S. Heifets, S. Krinsky, G. Stupakov, "CSR Instability in a Bunch Compressor", SLAC-PUB-9165, March 2002.

4 E. L. Saldin, E. A. Schneidmiller, M. V. Yurkov, "Longitudinal Phase Space Distortions in Magnetic Bunch Compressors", *FEL-2001 Conf*., Darmstadt, Germany, *DESY-01-129* (2001).

5 P. Emma, "Automated Optimization of Accelerator Parameters for Peak FEL Performance", to be published as an LCLS technical note.

6 P. Emma, P. Krejcik, C. Pellegrini, S. Reiche, J. Rosenzweig, *Proceedings of the 2001 Particle Accelerator Conf*erence, Chicago, IL, 2001.

7 K. L. Bane et al., "Electron Transport of a Linac Coherent Light Source (LCLS) Using the SLAC Linac," *Proceedings of the 1993 Part. Accel. Conf*., Washington, DC, 1993.

8 P. Emma, "X-Band RF Harmonic Compensation for Linear Bunch Compression in the LCLS", *LCLS-TN-01-01*, January 2001.

9 "Zeroth-Order Design Report for the Next Linear Collider", *SLAC Report 474*, May 1996.

10 M. Borland, "*Elegant:* A Flexible SDDS-Compliant Code for Accelerator Simulation", *ICAP-2000*, Darmstadt, Germany, September 2000.

11 L. M. Young, J. H. Billen, "Parmela"**,** *LA-UR-96-1835*, Rev, January 8, 2000.

12 C. Limborg et al., "New Optimization for the LCLS Photo-Injector", to be published at *EPAC-2002*, Paris, France, June 2002.

13 R. Akre, et al., "Measurements on SLAC Linac RF System for LCLS Operation", *Proceedings of the 2001 Part. Accel. Conf*., Chicago, IL, 2001.

14 J.B. Rosenzweig, and E. Colby, *Proceedings of the Conference on Advanced Acceleration Concepts*, AIP vol. 335, p. 724 (1995).

15 R. Assmann et al., "*LIAR*—A New Program for the Modeling and Simulation of Linear Accelerators with High Gradients and Small Emittances," *18th International Linac Conference*, Geneva, Switzerland, August, 1996.

16 "LCLS Design Study Report", SLAC-R-521, April 1998.

17 C.E. Adolphsen et al., "Beam-Based Alignment Technique for the SLC Linac," *Proceedings of the 1989 Part. Accel. Conf*., Chicago, IL, 1989.

18 J.T. Seeman et al., "The Introduction of Trajectory Oscillations to Reduce Emittance Growth in the SLC Linac," *15th International Conf. on High Energy Accelerators*, Hamburg, Germany, July 1992.

19 L.V. Iogansen, M.S. Rabinovich, *Sov. Phys. JETP*, vol.37(10), 1960, p. 83.

20 Ya. S. Derbenev, J. Rossbach, E. L. Saldin, V. D. Shiltsev, "Microbunch Radiative Tail-Head Interaction", *TESLA-FEL 95-05*, DESY, Sep. 1995.

21 E. L. Saldin, E. A. Schneidmiller, M. V. Yurkov, "On the Coherent Radiation of an Electron Bunch Moving in an Arc of a Circle", *TESLA-FEL 96-14*, Nov. 1996.

22 M. Dohlus, A. Kabel, T. Limberg, "Wakefields of a Bunch on a General Trajectory Due to Coherent Synchrotron Radiation", *Proceedings of the 19th International Free Electron Laser Conference*, Beijing, China, Aug. 18-21, 1997.

23 R. Li, C. L. Bohn, J. J. Bisognano, "Analysis on the Steady-State Coherent Synchrotron Radiation with Strong Shielding", *Proceedings of the 1997 Part. Accel. Conf.*, Vancouver, BC, Canada, 1997.

24 F. Zimmermann, "Longitudinal Single Bunch Dynamics and Synchrotron Radiation Effects in the Bunch Compressor," *NLC-Note-3*, SLAC, October 1994.

25 R. L. Warnock, "Shielded Synchrotron Radiation and Its Effect on Very Short Bunches," *SLAC-PUB-5375*, November 1990.

26 T. Limberg, "Emittance Growth in the LCLS due to Coherent Synchrotron Radiation," SLAC internal note, Oct. 1997.

27 M. Borland, "A Simple Method for Simulation of Coherent Synchrotron Radiation in a Tracking Code", *ICAP-2000*, Darmstadt, Germany, September 2000.

28 G. Stupakov, P. Emma, "CSR Wake for a Short Magnet in Ultrarelativistic Limit", submitted to *EPAC-2002*, Paris, France, June 3-7, 2002.

29 T. O. Raubenheimer et al., "Chicane and Wiggler Based Bunch Compressors for Future Linear Colliders," *SLAC-PUB-6119*, May 1993.

30 M. Dohlus, A. Kabel, T. Limberg, "Uncorrelated Emittance Growth in the TTF-FEL Bunch Compression Sections Due to Coherent Synchrotron Radiation and Space Charge Effects", *Proceedings of the 2000 European Particle Accelerator Conference*, Vienna, Austria, 2000.

31 Ya. S. Derbenev, V.D. Shiltsev, "Transverse Effects of Microbunch Radiative Interaction," *SLAC-PUB-7181, Fermilab-TM-1974,* May 1996.

32 M. Borland, "Bunch Compressor Design for the APS Linac", unpublished ANL note.

33 S. Anderson, et al, "OTR Monitor for the ATF Extraction", KEK/ATF internal report, *ATF-01-08*, June, 2001.

34 Andreas Kabel, private communication.

35 R. Chasman, K. Green, E. Rowe, *IEEE Trans., NS-**22***, 1765 (1975).

36 M. Borland et al., "Start-to-End Simulation of Self-Amplified Spontaneous Emission Free-Electron Lasers from the Gun through the Undulator," *Proc. of FEL2001*, Darmstadt, Germany, August 2001.

37 H.-D. Nuhn, to be published as an LCLS technical note.

38 Ming Xie, "Design Optimization for an X-ray Free Electron Laser Driven by SLAC Linac", *Proceedings of the 1995 Part. Accel. Conf.,* Dallas, TX, 1995.

39 S. Reiche, NIM A 429 (1999) 242.

40 J. Lewellen, private communication.

41 M.C. Ross et al., "Wire Scanners for Beam Size and Emittance Measurements at the SLC," *Proceedings of the 1991 Part. Accel. Conf.*, San Francisco, CA, 1991.

42 D.X. Wang, "Electron Beam Instrumentation Techniques Using Coherent Radiation," *Proceedings of the 1997 Part. Accel. Conf.*, Vancouver, BC, Canada, 1997.

43 G. A. Loew, O. H. Altenmueller, "Design and Applications of R.F. Deflecting Structures at SLAC", *PUB-135*, Aug. 1965.

44 R.H. Miller, R.F. Koontz, D.D. Tsang, "The SLAC Injector", *IEEE Trans. Nucl. Sci*., June 1965, p804-8.

45 X.-J. Wang, "Producing and Measuring Small Electron Bunches", *Proceedings of the 1999 Particle Accelerator Conference*, New York, NY, March 1999.

46 P. Emma, J. Frisch, and P. Krejcik, "A Transverse RF Deflecting Structure for Bunch Length and Phase Space Diagnostics", *LCLS-TN-00-12*, August 2000.

47 P. Emma, et al., "Bunch Length Measurements Using a Transverse RF Deflecting Structure in the SLAC Linac", to be published in the *Proceedings of the 2002 European Particle Accelerator Conference*, Paris, France, June 3-7, 2002.

48 O. H. Altenmueller, R. R. Larsen, and G. A. Loew, "Investigations of Traveling-Wave Separators for the Stanford Two-Mile Linear Accelerator", *The Review of Scientific Instruments*, Vol. 35, Number 4, April 1964.

49 I. Ben-Zvi, J. X. Qui, X. J. Wang, "Picosecond-Resolution 'Slice' Emittance Measurement of Electron-Bunches", Proceedings of the 1997 Particle Accelerator Conference, Vancouver, BC, Canada, May 1997.

50 D.X. Wang, "Measuring Longitudinal Distribution and Bunch Length of Femtosecond Bunches with RF Zero-Phasing Method," *Proceedings of the 1997 Part. Accel. Conf*., Vancouver, BC, Canada, 1997.

51 P. Bolton, *et al*., LCLS technical note to be published.

52 T. Himel et al., "Adaptive Cascaded Beam-Based Feedback at the SLC," *Proceedings of the 1993 Part. Accel. Conf*., Washington, DC, 1993.

53 J. L. Turner *et al.*, "Vibration Studies of the Stanford Linear Accelerator," *Proceedings of the 1995 Part. Accel. Conf.,* Dallas, TX, 1995.

54 G.S. Abrams et al., "Fast Energy and Energy Spectrum Feedback in the SLC Linac," *Proceedings of the 1987 Part. Accel. Conf.,* Washington, DC, 1987.

55 The MAFIA collaboration, *User Guide*, CST GmbH, Darmstadt, Germany.

56 K. Bane, P. Wilson, *Proceedings of the 11th Int. Conf. on High Energy Accelerators*, CERN (Birkhuser Verlag, Basel, 1980), p. 592.

57 K. Bane, *SLAC-NLC-Note 9*, February 1995, and in "Zeroth-order Design Report for the Next Linear Collider," *SLAC Report 474*, p. 367, May 1996.

58 K.L.F. Bane, M. Timm, T. Weiland, "The Short Range Wake Fields in the SBLC Linac", *Proceedings of the 1997 Part. Accel. Conf*., pp. 515, Vancouver, BC, Canada, 1997.

59 E. Keil, *Nucl. Instr. Meth. 100*, 419 (1972).

60 R. Gluckstern, *Phys. Rev D, 29*, 2780 (1989).

61 K.L. Bane, T. Weiland, "Verification of the SLC Wake Potentials," *SLAC/AP-001*, Jan. 1983.

62 A. Novokhatskii, A. Mosnier, "Short Bunch Wake Potentials for a Chain of TESLA Cavities," *DAPNIA-SEA-96-08,* Nov. 1996.

63 K.L.F. Bane, et al., "Calculations of the Short Range Longitudinal Wakefields in the NLC Linac", *Proceedings of the 1998 European Particle Accelerator Conference*, June 22-26, 1998.

64 K.L. Bane et al., "Measurements of the Longitudinal Phase Space in the SLC Linac," *SLAC-PUB-5255*, May 1990.

65 K.L. Bane et al., "Measurement of the Longitudinal Wakefield and the Bunch Shape in the SLAC Linac," *SLAC-PUB-7536,* May 1997.

66 K.L.F. Bane, et al., "Obtaining the Bunch Shape in a Linac from Beam Spectrum Measurements", *Proceedings of the 1999 Part. Accel. Conf*., New York, NY, USA, 1999.

67 C. Adolphsen, et al., "Measurement of Wake Field Suppression in a Damped and Detuned X Band Accelerator Structure", SLAC-PUB-7519, May 1997. 4pp, Submitted to *Phys. Rev. Lett*.

68 O. Napoly, O. Henry, "The Resistive-Pipe Wake Potentials for Short Bunches," *Particle Accelerators*, Vol. 35, pp. 235-247, 1991.

69 G. Stupakov, private communication, 2000.

70 K.L.F. Bane, M. Sands, "The Short-Range Resistive Wall Wakefields," Contributed *to Micro Bunches: A Workshop on the Production, Measurement and Applications of Short Bunches of Electrons and Positrons in Linacs and Storage Rings*, Upton, New York, September 28-30, 1995.